Tug of War between Epoxidation and Ketonization in Electrochemical Alkene Oxidation: Pulling the Rope for Ketonization

Thesis by
Chenyu Jiang

In Partial Fulfillment of the Requirements for the
Degree of
Doctorate in Chemistry

CALIFORNIA INSTITUTE OF TECHNOLOGY
Pasadena, California

2026
Defended May 21, 2026

© 2026

Chenyu Jiang
ORCID: 0000-0002-3434-3138

The copyright of this thesis rests with its author and is made available under a Creative Commons Attribution Non-Commercial No Derivatives license.

ACKNOWLEDGEMENTS

First and foremost, I would like to thank my advisor, Prof. Karthish Manthiram, for his unwavering support and encouragement throughout these years. I cannot fully express my gratitude to Karthish for giving me the opportunity to join his laboratory. When I first started at Caltech, I was torn between whether continuing in the same field as my undergraduate studies or venturing into something entirely new, which was scary. I remember my first couple of meetings with Karthish, and I had little background in electrochemistry; frankly, oxidation and reduction had always confused me. Yet those early conversations never made me feel discouraged or inadequate for what I did not know. Instead, I left each meeting feeling renewed and reinvigorated about learning and, more importantly, new science. Karthish took a chance on me, and ever since, I have been intrigued by electrochemistry and electrocatalysis. For that, I will forever be grateful!

Beyond research, I want to thank Karthish for cultivating a group from which I have learned enormously and within which I have had a great deal of fun. As part of the first cohort at the Manthiram Lab at Caltech, I had the privilege of watching the group take shape from the ground up. Karthish worked closely with us to build a lab space designed around the science we wanted to do. This collaborative and thoughtful process set the tone for everything that followed. What has always struck me the most, though, is his humility. Karthish treats graduate students with genuine respect, as peers and as scientists, which will always be inspiring to me.

I want to express my gratitude to my committee members, Prof. Kim See, Prof. Brian Stoltz, and Prof. Bill Goddard, for their time and thoughtful feedback throughout my graduate studies. Their insightful questions and perspectives during our meetings challenged me to think more deeply about my work and pushed me to become a more rigorous scientist. In addition, I would like to extend my gratitude to their administrative assistants, Aracely Sustaita, Tomoni Kano, and Margarita Davis, for their help in facilitating meeting scheduling.

I would also love to thank Dr. Frances Houle from LBNL. I had the pleasure of meeting Frances through LiSA, and across many meetings, she had always been reassuring and encouraging to me. When I expressed my interests in pursuing a postdoctoral position with Prof. Dr. Beatriz Roldán Cuenya at Fritz-Haber Institute, Frances generously offered to reach out on my behalf. That act of kindness played

a meaningful role in securing the position, and I am truly grateful for it. Academia can be an isolating and uncertain place to navigate, and having someone like Frances makes an enormous difference. I wish to carry on her kindness in my journey.

Through my studies, I had the pleasure to work with and learn from many brilliant scientists at Caltech and other institutes, and I am deeply grateful to all of them. Several deserve special mention. First, I would like to thank Dr. Michal Bajdich from SLAC, with whom I had the honor of collaborating on a LiSA project. I appreciate his genuine engagement and enthusiasm toward my project, which gave me encouragement and strength when I encountered difficult stretches in the lab. I also want to express my sincere gratitude to Dr. Nathan Dalleska from Water and Environment Lab at Caltech. Nathan was endlessly patient with me (even when he had to listen to my rants) and taught me everything I know about chromatography. Nathan's enthusiasm toward nature and sailing served as a constant reminder to me that there is a rich life beyond research and grinding at lab. Nathan will always be a role model to me for his patience and for the kindness he has shown to graduate students and his passion in life. Last, but not the least, I want to thank Dr. Ben Moss for being my mentor in the group and my friend. Ben joined the group as a postdoc during my third year and taught me about spectroscopies in his uniquely intense yet patient way. Ben has been someone who truly believes in me, even when I have doubts about myself and my work. I cannot express how much that means to me. Outside the lab, Ben was always there to talk, listen to my rants and complaints, and sometimes calm me down, as a friend. His down-to-earth and humbling manner attracted people from different subgroups to work with him, which will inspire me to be as versatile in knowledge and generous in spirit as him as a scientist.

My experience would not be the same without my wonderful lab mates and alumni whom I have had the pleasure to spend time with. I want to specifically thank my subgroup, sub O, and our sister subgroup — sub C — for thoughtful discussions and occasional shenanigans. I am grateful to Dr. Minju Chung, Dr. Joy Zeng, Dr. Joseph Maalouf, Emma Cosner, Spencer Delgado, Thu Ton, Dr. Kalipada Koner, Dr. Rachel Baker, Dr. Jason Adams, and the honorable members, Dr. Haochen Zhang and Dr. Evan Miu. I hope our new members — Abbie Blenko, Jong-Yeong Jung, Hari Karthik, and Jason Zhang — will have the experience as great and fun as mine. Minju, Joy, and Joseph were the last cohort at MIT. Although far in distance, they were a significant presence for the subgroup and group meetings. I had the pleasure to visit the MIT lab and worked with Minju and Joy in person during several

beamline trips, learning from them how to do electrochemistry, which as people often say is an art form. I want to give a special shout-out to Dr. Rachel Baker whose optimism and lively demeanor always brightened my days in the lab. Science is still not as friendly to female scientists as we would like it to be, and watching Rachel traverse through and succeed in this male-dominant field is inspirational. One of the most meaningful experiences during my studies is to mentor my two undergraduate students, Yamilet Rivera Cintrón and Alexis Lindenfelser. I am grateful for their trust in me and choosing me as their mentor. I hope the brightest future for both of them! In addition, I would like to express my appreciation to the administrative staff of the group, Martha Hepworth and Matt Buga, for their consistent support and help.

This September will mark the tenth year since I left home to go to school abroad. I am the first person in my family to graduate from college, let alone obtaining a doctorate degree. Living far away from home is not easy, and getting the PhD degree is fundamentally a traumatizing experience. I would not have been able to accomplish the same without the help from my psychologists, Dr. Shauna McManus and Dr. Kris Yi. I appreciate their attentive care that was above and beyond, and I am grateful to have them as part of my experience.

Along the way, I have found such good friends that I can call them my family. I am beyond appreciative to my friend from college, Jacqueline Huang, who has not given up on me even though I often disappear from conversations to deal with my life. I am grateful to Termeh Bashiri, Alexi McAdams, SoYoungn Shin, Matt Ratanapanichkich and Cyrus Fiori for their friendship and for the good and elegant food we have shared and fun nights at Paint and Sip. I want to thank my "big brothers" in the group, Gangsan Lee, Haochen Zhang, and Ben Moss, for helping me in research as well as in life. My family would not be complete without my cohort friends, Thu Ton, Channing Klein, and James Wang, and Colin Morrell. I am grateful for their friendship and company when I needed the most. Late nights out at Afters and L'moon over ice cream and bottled water for James will remain one of my most cherished memories for life. We laughed, we shouted, we lamented, and we bonded. No words are heartfelt and sincere enough to express their importance to me and how much they have supported and helped me throughout this experience. They have been the strength and the North Star whenever I felt I did not have what it took to get the PhD degree. I wish for life-long friendships with these wonderful people.

Life would not have the same fun and meaning without my cats, Ziggy and Louie. I am forever grateful for their existence and their companionship. At last, I want to thank my blood family — my parents, my sisters, my grandma for everything. Never mind that it is hard to explain how academia works and what I do exactly, they have always believed in me and cheered me on no matter how abstract my accomplishments are. In a way, all of my achievements are for my mom who is so brave and brilliant but lacked the opportunities and for my sisters so that they know they can achieve anything they want. My mom and my grandma have raised me to be the person I am, and I would not be able to achieve any of my accomplishments without the integrity and principles as well as the kindness they have taught me. So truly, thank you.

To my mother

"We mortals, men and women, devour many a disappointment between breakfast and dinner-time; keep back the tears and look a little pale about the lips, and in answer to inquiries say, 'Oh nothing!' Pride helps us; and pride is not a bad thing when it only urges us to hide our own hurts – not to hurt others."

— George Eliot, *Middlemarch*

ABSTRACT

The electrochemical oxidation of organic molecules utilizing renewable electricity has emerged as a sustainable alternative to energy-intensive thermal processes in the chemical industry. This thesis investigates electrochemical oxygen-atom transfer reactions to transform alkenes into value-added products using water as the oxygen source under ambient temperature and pressure, with a focus on understanding and controlling the competing pathways between epoxidation and ketonization.

Chapter 2 establishes the mechanistic foundation of alkene electro-oxidation in a model system using MnO_x as the catalyst, and a substrate-scope study reveals a correlation between theoretically determined alkene electrophilicity and epoxide/ketone selectivity. Complementary kinetic and *operando* spectroscopic studies demonstrate that ketonization is favored at lower water content, which corresponds to a less oxidized catalyst and hence indicates catalyst oxidation state as a key selectivity-governing factor.

Building on these mechanistic insights, Chapter 3 describes the screening and optimization of Pd-based bimetallic electrocatalysts for aqueous 1-butene ketonization. Bimetallic PdCu/C was identified as an active and selective catalyst, with the metallic phase outperforming the oxidized analogues, corroborating the findings in Chapter 2. The critical role of synthetic methods in determining catalytic performance is demonstrated through comparison of two bimetallic Pd–Cu catalysts of identical nominal composition prepared via different procedures.

Chapter 4 interrogates the structural origins of PdCu's superior activity through comparative characterization of pristine and post-electrolysis catalysts. Alloying Pd and Cu is found to generate a metallic phase that is retained under harsh anodic conditions, in contrast to monometallic and pre-oxidized controls. The metallic PdCu alloy phase was proposed as a key factor in driving selective 1-butene ketonization, establishing a structure-activity relationship for rational catalyst design.

PUBLISHED CONTENTS AND CONTRIBUTIONS

1. Jiang, C.; Moss, B.; Lindenfelser, A.; Kim, J. T.; Li, Y.; Manthiram, K. Metallic Pd–Cu Alloy Phases Drive Selective Heterogeneous Electrochemical Ketonization of 1-Butene. *ACS Catalysis* **2026**, *16*, 7429–7438, DOI: 10.1021/acscatal.5c08675

   Contributions: Conceptualization, Data curation, Formal analysis, Investigation, Methodology, Project administration, Resources, Software, Supervision, Validation, Visualization, Writing — original draft, and Writing — review and editing.

   The materials in Chapter 4 and Appendix C are adapted from this publication.

2. Zeng, J. S.; Cosner, E. L.; Delgado-Kukuczka, S. P.; Jiang, C.; Adams, J. S.; Román-Leshkov, Y.; Manthiram, K. Electrifying Hydroformylation Catalysts Exposes Voltage-Driven C–C Bond Formation. *Journal of the American Chemical Society* **2024**, *146*, 16521–16530, DOI: 10.1021/jacs.4c02992

   Contributions: Validation.

3. Chung, M.; Maalouf, J. H.; Adams, J. S.; Jiang, C.; Román-Leshkov, Y.; Manthiram, K. Direct propylene epoxidation via water activation over Pd-Pt electrocatalysts. *Science* **2024**, *383*, 49–55, DOI: 10.1126/science.adh4355

   Contributions: Writing — review and editing.

4. Koner, K.; Adams, J. S.; Miu, E. V.; Delgado-Kukuczka, S. P.; Jiang, C.; Kim, J. T.; Park, H.; Bui, J. C.; Oyala, P. H.; Li, Y.; Manthiram, K. Direct electrochemical propylene epoxidation over amorphized perovskite oxide in non-halogenated aqueous electrolyte. *Nature Catalysis* **2026**, 1–10, DOI: 10.1038/s41929-026-01535-6

   Contributions: Data curation, Formal analysis.

5. Adams, J. S.; Koner, K.; Moss, B.; Bui, J. C.; Jiang, C.; Cosner, E. L.; Park, Y.; Chung, M.; Kim, J. T.; Park, H.; Li, Y.; Manthiram, K. Structure of PdPtOx and Kinetic Analysis of Electrochemical Propylene Epoxidation. *Angewandte Chemie International Edition* **2026**, *Manuscript submitted.*

   Contributions: Data curation, Formal analysis.

TABLE OF CONTENTS

LIST OF ILLUSTRATIONS

LIST OF TABLES

LIST OF NOMENCLATURE AND ABBREVIATIONS

Constants and Nomenclatures.

η**.** overpotential.

E_a**.** activation energy.

F**.** Faraday's constant 96485.3321 C mol^{-1}

G**.** Gibbs free energy.

$G^{\ddagger}$**.** Gibbs free energy of activation.

$H^{\ddagger}$**.** enthalpy of activation.

$S^{\ddagger}$**.** entropy of activation.

Chemical Abbreviations.

Ag_3PO_4. silver phosphate.

Co_3O_4. cobalt(II,III) oxide.

$CuCl_2$. copper(II) chloride.

D_2O. deuterium oxide.

H_2PtCl_6. hexachloroplatinic acid.

H_2. hydrogen.

H_3PO_4. phosphoric acid.

Mn_3O_4. manganese(II,III) oxide.

MnO_x. manganese oxide.

$NaBH_4$. sodium borohydride.

$NaClO_4$. sodium perchlorate.

$NiCl_2$. nickel(II) chloride.

$NOBF_4$. nitrosonium tetrafluoroborate.

O_2. oxygen.

$PdCl_2$. palladium chloride.

$RhCl_2$. rhodium(II) chloride.

$RuCl_3$. ruthenium(III) chloride.

$TBABF_4$. tetrabutylammonium tetrafluoroborate.

Cr. chromium.

DMF. N,N-dimethylformamide.

FTO. fluorine-doped tin oxide.

Ge. germanium.

HCl. hydrochloric acid.

NaOH. sodium hydroxide.

TMB. 1,3,5-trimethoxybenzene.

Abbreviations and Acronyms.

Fc/Fc^+. ferrocene/ferrocenium.

Ag/AgCl. silver/silver chloride.

BV. Butler-Volmer.

CA. chronoamperometry.

CCD. charge-coupled device.

CV. cyclic voltammetry.

DFT. density functional theory.

DLC. double-layer capacitance.

EC. electrochemical.

ECSA. electrochemically active surface area.

EDL. electric double layer.

EDL. electric double-layer.

EDS. X-ray energy-dispersive spectroscopy.

FE. Faradaic efficiency.

GC. gas chromatograph.

HRTEM. High-Resolution Transmission Electron Microscopy.

MS. mass spectrometry.

NMR. nuclear magnetic resonance spectroscopy.

OAT. oxygen-atom transfer.

OCV. open circuit voltage.

OER. oxygen evolution reaction.

PDS. potential-determining step.

RDS. rate-determining step.

RHE. reversible hydrogen electrode.

ROS. reactive oxygen species.

sccm. standard cubic centimeters per minute.

SEM. scanning electron microscopy.

SHE. standard hydrogen electrode.

SMD. solvation model based on density.

SWV. square-wave voltammetry.

TEM. transmission electron microscopy.

UV-Vis SEC. ultraviolet-visible spectroelectrochemistry.

XANES. X-ray Absorption Near Edge Structure.

XAS. X-ray absorption spectroscopy.

XPS. X-ray photoelectron spectroscopy.

XRD. X-ray diffraction.

Symbols.

∘. degree.

% v/v. volume percentage.

°C**.** degree Celsius .

wt%. weight percentage.

Chapter 1

INTRODUCTION

1.1 Brief background on electrocatalysis

The first electrocatalytic reaction was performed by Deiman and van Troostwijk in 1789[6,7] nearly 150 years before the term "electrocatalysis" was coined by Kobozev and Monblanowa in 1936.[8] Predating electricity as we know it, they carried out water splitting with two gold electrodes powered by an electrostatic generator. By 1890, Renard established a water electrolyzer unit to supply hydrogen (H_2) for French military airships.[9] Despite this early demonstration, the industrial scale of H_2 production via electrolysis has yet to reach maturity, though interest has grown rapidly as H_2 emerges as a promising energy carrier to replace fossil fuels.[9,10] The urgency of decarbonizing the chemical industry, which contributes 24% of total global greenhouse gas emissions,[11] has further broadened the interest in electrocatalysis.[12] Unlike traditional thermal methods that rely on heat (mainly derived from fossil fuel resources) and high pressures to drive chemical transformations, electrocatalysis utilizes voltage from renewable sources to enable thermodynamically difficult reactions at milder conditions.[13,14] Thus, electrocatalysis represents a promising strategy toward carbon neutrality and reduced fossil fuel dependence in the chemical industry.

Even though water electrolysis is a century-old technology, the anodic reaction, oxygen evolution reaction (OER), remains a quandary, as its exact reaction mechanisms have yet to be fully established and continue to be debated.[15–17] This mechanistic ambiguity has contributed to the slow realization of large-scale water electrolyzers, more than a century after Renard's first example. The complexity arises in part from the nature of the electrified interface between the electrode and the electrolyte. Electrochemistry is inherently a heterogeneous process in which reactant species in the electrolyte (liquid) migrate to spatially separated electrodes (solid) where redox reactions occur. The efficiency and selectivity of an electrocatalytic reaction depend on a multitude of interdependent factors, including the intrinsic reaction kinetics, mass transport of reactants, and surface adsorption/desorption of reactants and products, making the design of efficient electrocatalytic systems particularly challenging. A thorough understanding of these fundamental aspects is therefore

essential for developing effective electrocatalysts that facilitate desired chemical transformations. The following section summarizes the key theoretical foundations of electrocatalysis.

Thermodynamics and kinetics of electrocatalysis

Charge transfer in electrocatalysis can occur via a redox mediator in the solution phase, where electrons are transferred between reactant and mediator molecules homogeneously. Alternatively, in heterogeneous electrocatalysis, electrons are transferred directly between the reactant species and the electrode. The electron transfer proceeds through either an inner- or outer-sphere mechanism, depending on the strength of interaction between the reacting species and the electrode surface. In an outer-sphere process, electrons transfer via tunneling without direct adsorption of reaction species, whereas in an inner-sphere reaction, the reaction species adsorb onto the electrode surface, and strong surface-adsorbate interaction can lead to the formation of a chemical bond (chemisorption). Consequently, inner-sphere reactions are strongly influenced by the electrode materials, and their reactivity can be modulated by the choice of electrocatalyst.[18] Most of electrocatalytic reactions, including OER, proceed via an inner-sphere process,[16,19] and this thesis will exclusively focus on *heterogeneous, inner-sphere* electrocatalysis.

Unlike thermocatalysis, where heat and pressure boost reaction rates, electrocatalysis promotes the formation and breaking of chemical bonds by electron and ion transport at the electrode surface, enabling conversion of electric energy to chemical energy.[20] A defining feature of electrocatalysis is that the application of the voltage modulates not only the activation energy (E_a) of the reaction (thus the rate) but also its thermodynamic free energies:[21]

$$\Delta\Delta G = -nF\Delta V_{app} \tag{1.1}$$

where $\Delta\Delta G$ is the change in Gibbs free energy of the reaction upon the change in applied voltage ΔV_{app}, n is the number of electrons transferred, and F is Faraday's constant.

Equation 1.1 illustrates a remarkable feature of electrocatalysis, the free energy of the reaction scaling *linearly* with the external potential, in contrast to the *exponential* relationship with heat or pressure.[14] This feature allows electrocatalysis to drive thermodynamically unfavorable reactions at ambient temperature and pressure. For instance, water splitting would require a temperature exceeding 2000 °C under thermochemical conditions, yet proceeds at room temperature when ΔV_{app} exceeds 1.23

V vs SHE, the thermodynamic potential of water oxidation.[22] Additionally, because oxidation and reduction half-reactions occur at spatially separated electrodes, the products generated are inherently separated, avoiding recombination issues common in thermocatalysis.

The charge transfer directly involved in the consumption of reactants and formation of products constitutes the *Faradaic* process. The selectivity of an electrocatalytic system is quantified by Faradaic efficiency (FE), which represents the fraction of the total charge consumed by the desired reaction:

$$\textit{Faradaic efficiency (\%)} = \frac{\text{amount of product generated}}{\text{theoretical yield with the total charge supplied}} \times 100. \tag{1.2}$$

Electrochemistry allows for direct measurement of reaction rate by means of the current density. The total current density I represents the total current passing through the electrode per unit area during an electrochemical process, and the partial current j toward a specific product is given by:

$$j = \frac{FE \times I}{100}. \tag{1.3}$$

The Butler-Volmer (BV) equation empirically describes the relationship between applied potential and current density:

$$j = j_0\{exp[\frac{\alpha nF\eta}{RT}] - exp[\frac{(1-\alpha)nF\eta}{RT}]\} \tag{1.4}$$

where j_0 is exchange current density at equilibrium, n is the number of electrons involved, η is the overpotential defined as the difference between applied potential and the standard equilibrium potential, and α is the anodic charge transfer coefficient representing the fraction of applied potential that lowers the activation energy for the anodic reaction. At large η, one partial current dominates; under a large anodic potential, the cathodic contribution becomes negligible. Thus, Equation 1.4 reduces to the Tafel equation, expressing η as a function of j:

$$\eta = a + b\ log\ j \tag{1.5}$$

where b is the Tafel slope, widely employed to assess the electrocatalytic activity.[8,23] It is important to note that the BV framework is strictly valid only for *single-electron* transfer, and Tafel analysis assumes a well-defined rate-determining step (RDS) such that only electrons participating in the RDS are included in the rate

equation. Furthermore, the BV-Tafel framework was originally derived for *outer-sphere* reactions, and no general equivalent exists for inner-sphere processes.[24] These limitations should be recognized when interpreting kinetic data in *inner-sphere* electrocatalysis.

Electrified Interface

The application of external electric fields induces charge separation at the electrode-electrolyte interface, resulting in a potential gradient across the interface. This interfacial region is highly inhomogeneous, and the potential field drives the rearrangement of ions and solvent molecules depending on the charge at the electrode surface, leading to the formation of the electric double layer (EDL).[21,25,26] Heterogeneous electrocatalytic reactions proceed within the electrified interface, and the physicochemical properties of species in the EDL play a vital role in controlling selectivity and activity as these species undergo dynamic changes under the influence of the external voltage and are chemically distinctive from those in the bulk of electrolyte.[27–31] Given the importance of the electrified interface in governing reaction outcomes, this thesis will primarily focus on *anodic oxidation reactions*, using OER as a well-studied model system before narrowing toward the electrochemical oxidation of organic molecules, specifically alkenes.

OER is generally understood to proceed via four consecutive electron transfer steps at the electrocatalyst surface, transforming H_2O to O_2. The generation of protons during this process and the dynamic equilibrium of H_2O in neutral, alkaline, and acidic electrolytes influence local ion distribution and pH, meaning that the EDL should not be assumed to be static but rather dynamic under OER or any other electrocatalytic conditions.[31,32] The interactions between all species present at the interface greatly affect the energetics of surface adsorbates and hence reaction rates.[28] Under anodic polarization, the electrode surface carries positive charges and recruits negatively charged anions, which in turn bring co-cations into the interfacial region; the resulting high ion concentration modifies the strength of the electric field of the EDL.[33] Both anion and cation effects on OER have been widely discussed in the literature, yielding a complex and dynamic picture of the electrified interface.[33–38]

Partially solvated anions can coordinate directly with the surface active sites via specific adsorption, forming direct bonding interaction beyond electrostatic interaction of fully solvated ions.[29,33] Such covalent chemisorption modifies the surface charge

of the electrode and alters the energetics of the intermediates, thereby influencing reaction kinetics. Anions have also been shown to induce catalyst reconstruction through leaching, creating defects and oxygen vacancies, or through intercalation into metal hydroxide layers.[34,39–44] These anion effects have also been observed for electro-oxidation of small organic molecules, suggesting their relevance extends beyond OER.

It is perhaps less intuitive to consider cation effects in anodic reactions. The Gouy-Chapman-Stern EDL model predicts that the ions of opposite charge to the electrode surface form a compact layer near the surface, with their co-ions residing in the diffuse layer,[21,25,26,29] seemingly implying a minor role for cations under oxidative polarization. However, deprotonation of surface oxygen species can yield negatively charged adsorbates that are stabilized by cations in the electrolyte.[45,46] In addition, noncovalent interactions between solvated cations and chemisorbed intermediates have been proposed to block active sites and reduce activity.[47,48] Beyond direct interactions with adsorbed intermediates, cations have been demonstrated to alter interfacial water structure by disrupting the hydrogen bonding network.[36,37] In particular, the strong polarizing and hydration ability of alkali cations promotes the formation of highly polarized water molecules and tunes the number and formation of hydrogen bonds, impacting the energetics of reaction intermediates and the reactivity of interfacial OH^- in alkaline electrolytes.

The complexity of the electrified interface extends beyond ion distribution to the thermodynamic driving forces of the reaction itself. As discussed in the previous section, the applied potential modulates the thermodynamics of the reaction by altering the Gibbs free energies (Equation 1.1). It also controls the reaction rate by changing Gibbs free energy of activation ($\Delta G^{\ddagger}$) which depends on both the enthalpy ($\Delta H^{\ddagger}$) and entropy ($\Delta S^{\ddagger}$) of activation.[49] Early work done by Conway and coworkers separated these enthalpic and entropic contributions and illustrated the crucial role of entropic effects in electrocatalysis.[50] More recently, potential-resolved Arrhenius analysis has demonstrated that the entropy of activation, related to the interfacial reorganization under applied potential, can serve as a primary driving force for electrocatalytic reactions.[51–54] In particular, OER has been found to be intrinsically linked to an interfacial solvation step, driven by an increase in $\Delta S^{\ddagger}$ prior to the BV kinetics regime at high overpotential.[51] Thus, the electrified interface should not be treated as merely a passive medium but an active participant in determining the selectivity, kinetics, and thermodynamics of electrocatalytic reactions.

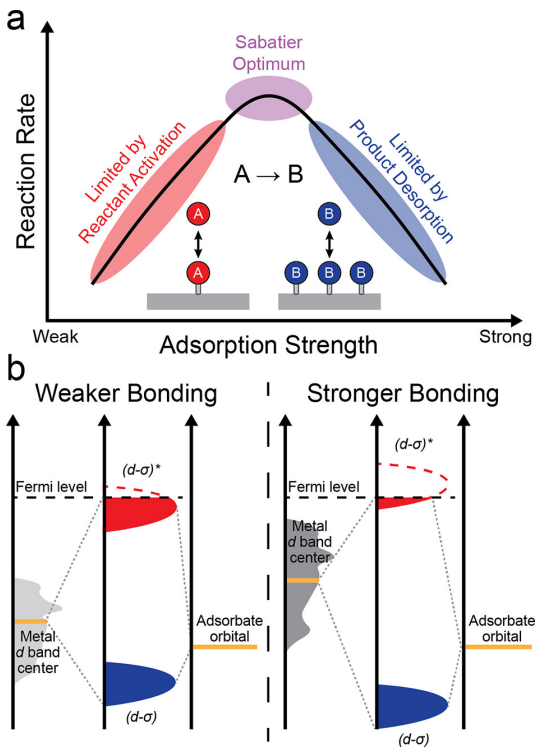

Figure 1.1: Schematics showing the Sabatier principle (a) and *d*-band theory (b) in adsorption. Reproduced with permission from [29]. Copyright 2024 American Chemical Society.

Adsorption

The previous section has highlighted the significance of adsorption at electrocatalyst surfaces in electrocatalysis. The intrinsic ability of a catalyst to interact with reactants via chemisorption or physisorption has therefore emerged as a key design principle in the search for next-generation electrocatalysts. The relationship between the catalyst structure and electrocatalytic activity is usually described using the Sabatier principle, which proposes that optimal catalysis occurs when the reactant binds with the active sites with an intermediate strength (Figure 1.1a).[55] Reactants and intermediates need to be stabilized at the surface, but binding that is too strong renders subsequent catalytic steps energetically prohibitive. The Sabatier principle is rooted in thermodynamics, as the binding energy is an equilibrium constant describing adsorption and desorption of species. It is utilized to rationalize catalytic activity considering Brønsted-Evans-Polanyi relationships where kinetically relevant $\Delta G^{\ddagger}$ is assumed to scale universally with ΔG.[56]

The electronics of adsorption strength is described by *d*-band theory, which relates the binding strength of adsorbates to the *d*-band center of the electrocatalyst relative

to its Fermi level.[57–62] Analogous to frontier molecular orbital theory, the interaction between the *d*-band of the electrocatalyst surface and the valence orbital of the adsorbate gives rise to bonding and antibonding states (Figure 1.1b).[29] The adsorption strength is dictated by the degree to which these antibonding states are populated, which depends on their energy relative to the catalyst's Fermi level; higher *d*-band center raises the antibonding states above the Fermi level, depopulating them and strengthening adsorption.[57,61,63,64] Applying *d*-band theory and the Sabatier principle has led to the construction of volcano plots, which correlate catalytic activity with binding energies of key surface intermediates, $\Delta G_{*O} - \Delta G_{*OH}$, establishing structure-reactivity descriptors for rational catalyst design.[65,66] While widely employed in electrocatalysis and correlating well with empirically measured catalytic activity, the application of *d*-band theory in volcano plots uses binding energies calculated from the gas phase and treats the electrified interface as a static microenvironment, largely overlooking the potential-dependent nature of the EDL and the influence of interactions between electrolyte components and the catalyst surface. Recent developments in the volcano methodology and efforts to account for some missing factors, such as overpotential and kinetic effects, for OER are described in ref [66]. The simplification of the binding-energy-based volcano approach therefore limits the ability of the framework to describe the electrochemical adsorption dynamics, particularly in the presence of organic reactants such as alkene.[29,37]

While the preceding section on the electrified interface briefly describes the adsorption and noncovalent interactions of charged species as an outcome of the applied potential and their significance in governing surface reactions, the adsorption of neutral organic molecules has also been shown to be potential-dependent.[67–69] For instance, Schreier and coworkers revealed the potential-dependent behavior of n-alkane adsorption in C-C bond cleavage under anodic polarization using electrochemical mass spectrometry (EC-MS), which enables the real-time detection of gaseous products desorbing from the catalyst surface at steady state and thereby provides indirect information on reactant adsorption.[68,69] Intriguingly, the selectivity between alkane fragmentation (producing smaller alkanes) and dehydrogenation (yielding alkenes) can be controlled by the applied potential, as the potential affects the desorption of the fragmented/dehydrogenated intermediates and electrolyte cations.[68] Such potential-dependence of alkane adsorption and selectivity is rationalized by the interactions of the adsorbates, ions, and solvent molecules at the electrified interface. Direct experimental measurement of adsorption at the electrified interface remains challenging and is mostly evaluated using computational methods that overlook the

complex interfacial microenvironment. While EC-MS is limited to gaseous desorbing products, *operando* UV-Vis spectroelectrochemistry (SEC) monitors changes in the absorbance spectra of the electrocatalyst surface under applied potential, providing insights into the redox intermediates and surface coverage during OER.[37,70,71] Rao and coworkers employed this technique alongside complementary spectroscopic methods to elucidate the key kinetic differences between acidic and alkaline OER at IrO_x and incorporated adsorbate-adsorbate interactions into the conventional $\Delta G_{*O} - \Delta G_{*OH}$ descriptor to better account for experimental findings.[37] The application of *operando* UV-Vis SEC to probe electrochemical alkene oxidation is described in Chapter 2.

1.2 Electrocatalyst design

In contrast to thermocatalysts, electrocatalysts offer an additional handle on reaction rate and selectivity through the applied potential, which modulates thermodynamic constraints alongside the intrinsic electronic properties of the catalyst material.[72] In practice, the electrocatalysts are oftentimes nanoparticles, owing to high surface area, deposited as a catalyst layer onto conductive substrates that serve as the electrodes. A common modification of the catalyst layer is the incorporation of ionomers such as Nafion to tune the reaction interface.[73] Consequently, the observed electrocatalytic activity reflects the interplay of all the components of the electrode, beyond solely the electrocatalyst itself. As established in Section 1.1, electrocatalytic systems are complex and intricate, consisting of a multitude of factors governing the reaction kinetics and thereby resulting in insufficient understanding of the system. The lack of detailed mechanistic insights into electrocatalytic reactions has led to the reliance on trial-and-error screening of catalysts, in particular with new reactions to expand the scope of synthetic strategies. This section discusses the strategies that guide the design and screening of selective nanoparticle electrocatalysts.

While computational methods may not capture the complexity of real electrode-electrolyte microenvironments in their entirety, theoretical insights offer a valuable general framework for catalyst design.[65,74,75] As discussed in the section on adsorption at the catalyst surface, the Sabatier principle and d-band theory enable the use of binding energy of key intermediates as descriptors for OER catalyst design. This descriptor-based approach has been extended to electrochemical epoxidation, where O binding energy has been proposed as an analogous design criterion concerning the competing pathways between epoxidation and OER.[76–78] Although such studies necessarily rely on model systems that are too simplified to represent real cata-

lysts effectively, they provide useful guidance for compositional screening and help narrow the catalyst search space.

One common strategy to improve catalysts' selectivity and activity is alloying or particulate mixing. Solid catalysts consisting of two or more metals can exhibit enhanced performance,[79] as the electronic and geometric structures of multi-metallic nanoparticles are distinct from those of their monometallic counterparts. However, the correlation between reactivity and these structural factors remains poorly understood,[80] in part due to the difficulty in elucidating the roles of different metals in the reaction. A bimetallic catalyst can enhance reactivity through a bifunctional mechanism, whereby each metal site facilitates a different step in the reaction;[81] alternatively, the reaction may proceed at a single metal center whose electronic structure is perturbed by the presence of the second metal.[82] These enhancement mechanisms are not mutually exclusive and may contribute to different degrees depending on the reaction and conditions. Further complicating the picture, bimetallic catalysts could adopt a wide range of structural motifs, ranging from solid solution with uniform lattice to random mixture with multiple phases, making structure-activity relationships and identification of the catalytically relevant phases particularly challenging. Elucidating the roles of different metal centers and the active phases is thus essential for developing rational design principles for future catalysts.[80]

Beyond catalyst composition, synthetic parameters should be carefully considered, as the resulting surface morphology and structural inhomogeneities greatly influence the underlying electrocatalytic activity.[83,84] Recent studies have found that the electrocatalytic reactions can be facet-dependent.[85–89] For instance, for a Co_3O_4 thin film catalyst prepared by ultra-high vacuum deposition, the (001) facet is more reactive than the (111) facet, which is likely due to the 4- and 5-fold-coordinated surface metal ions in the (001) facet compared to the 3-fold-coordinated ones in the (111) facet.[88] Furthermore, the (100) facet of Ag_3PO_4 crystals was found to be more active for propylene epoxidation than the (110) and (111) facets as the (100) phase likely promotes the breaking of the π bonding and facilitates the formation of C–O bond.[89] For bimetallic nanoparticles, co-reduction of the two metal precursor salts is a widely employed synthetic approach, where the choice of the reducing agents influences the reduction kinetics and mechanisms, yielding nanoparticles of different structures even from the same nominal composition.[90,91] Additionally, the shape and size of nanoparticles can be modulated through the use of capping agents such as sodium citrate. Chapter 3 discusses two bimetallic Pd–Cu catalysts prepared

via co-reduction using different reductants and capping agents and examines how the resulting structural differences influence their reactivity toward electrochemical 1-butene ketonization.

Electrocatalysis also faces broader reproducibility challenges owing to the high experimental complexity and sensitivity of heterogeneous catalysts. A recent round-robin study found that OER currents measured across different laboratories following standardized protocols varied by up to *two orders of magnitude*, highlighting the limited interlaboratory reproducibility in OER.[92] Therefore, beyond catalyst design, rigorous and consistent experimental practices are essential for generating reliable and meaningful results in electrocatalysis.

1.3 Electrochemical oxygen-atom transfer and alkene ketonization

Selective oxidation of alkenes transforms inexpensive starting materials into value-added products, such as epoxides and ketones, which are versatile intermediates in the manufacture of polymers and fine chemicals.[93–95] However, alkenes, especially aliphatic ones formed in petroleum cracking, are unreactive and challenging to functionalize. Traditionally, conditions that pose safety issues and generate toxic byproducts, like strong oxidants and elevated pressures and temperatures, are required to overcome the inertness of alkenes. For instance, most alkene epoxidation reactions require peroxide-based oxidants, such as *m*-chloroperoxybenzoic acid, or are enabled through the chlorohydrin process, generating undesired stoichiometric byproducts.[96,97] Wacker-type oxidation employs Pd(II) catalysts under O_2 atmosphere with stoichiometric Cu co-oxidants to convert terminal alkenes to methyl ketones.[98–103] These drawbacks of the conventional methods call for the search for more sustainable alternatives to achieve carbon neutrality and reduce reliance on fossil fuels in the chemical industry.

Electro-oxidation using water as the oxygen atom source offers an attractive alternative, as it avoids the need for exogenous, harsh chemical oxidants and operates under ambient conditions owing to the thermodynamic relationship between the external voltage and the Gibbs free energy (see Thermodynamics and kinetics of electrocatalysis in Section 1.1).[104] In this approach, inner-sphere activation of water yields reactive oxygen intermediates at the catalyst surface, which can be transferred directly to the alkene substrate via oxygen-atom transfer (OAT). This OAT pathway competes directly with OER, in which these oxygen intermediates undergo complete oxidation and generate O_2.[105] As a result, the reactivity and stabilization of

surface oxygen intermediates are considered the key factors regulating the selectivity between OER and OAT. Work done by Manthiram and coworkers demonstrated electrochemical oxidation of cyclooctene with MnO_x as the catalyst using water as the sole oxygen atom source, whereby cyclooctene oxide was observed as the major product alongside cyclooctanone.[106] Moreover, selectivity toward epoxidation can be further improved by tuning the electronics of MnO_x through Ir doping, allowing for more facile oxidation of the catalyst with anodic potential.[107] Since this demonstration, electrochemical OAT to alkenes has been extended across a range of electrocatalysts and substrates, with epoxidation as the main focus.[3,89,108–112]

Beyond OAT vs. OER selectivity, controlling epoxide-ketone selectivity is another key aspect of selective alkene oxidation (Figure 1.2), yet it remains poorly understood. One of the few studies to explicitly address this selectivity demonstrated that molecular Pt(II) complexes can switch between epoxidation and ketonization depending on the oxidants (H_2O_2 vs. t-BuOOH),[113] suggesting that the OAT pathways can be modulated by the nature of the oxygen species. Ketone formation during alkene electro-oxidation has also been documented in the presence of Pd-based electrocatalysts,[109–111,114] although this reactivity is often ascribed to homogeneous catalysis by soluble Pd ions released through oxidative corrosion of the electrode, casting doubt on the heterogeneous nature of the reaction.[111,114] Electrocatalysts engineered for high epoxidation selectivity, such as Pd-Pt alloys,[3] tend to disfavor ketone formation. Nonetheless, both computational and experimental evidence points to a potential-dependent component in alkene electro-oxidation selectivity,[110,115] raising the possibility that judicious catalyst design and voltage control could steer the reaction toward ketone products. However, heterogeneous electrocatalysis for selective alkene ketonization remains underexplored.

The conversion of terminal alkenes to ketones is well-established in thermocatalysis. The Wacker-Tsuji oxidation, the most widely employed homogeneous route, utilizes $PdCl_2$ as the catalyst with CuCl as a stoichiometric co-catalyst under aerobic conditions.[98–100] Heterogeneous variants have also been developed, with Pd–Cu systems immobilized on zeolite supports, demonstrating Wacker-type ketonization activity under thermal conditions.[101,102,116] These precedents establish Pd–Cu as a promising compositional framework for ketonization catalysis and motivate the exploration in aqueous media. In this context, we recently demonstrated that bimetallic PdCu electrocatalysts can achieve selective ketonization of 1-butene under aqueous ambient conditions, with the metallic PdCu alloy phase identified as the catalytically

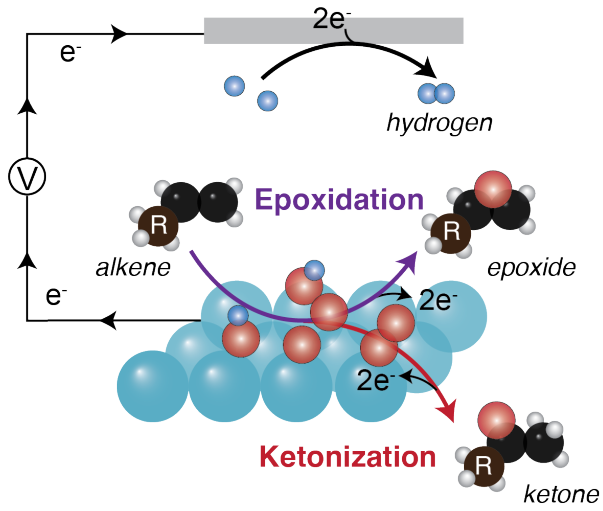

Figure 1.2: Schematics of electrochemical alkene oxidation using water.

relevant phase for this transformation.[1] This work represents the first heterogeneous electrocatalytic system specifically targeting selective alkene ketonization and forms the basis for Chapters 3 and 4 of this thesis.

1.4 Scope of this thesis

The chemical industry's reliance on fossil fuels and energy-intensive thermal processes has motivated the search for sustainable alternative chemical synthesis. Electrochemical oxidation of organic molecules represents a promising strategy, leveraging renewable electricity to drive thermodynamically challenging chemical transformations under mild conditions. This thesis explores electrochemical oxidation of alkenes under ambient conditions by means of water activation, in which the oxygen intermediates generated are directly transferred to the alkenes to form oxidized products, competing with OER. Understanding and controlling the selectivity of this process, as well as identifying selective electrocatalysts, are the central themes of this thesis.

Chapter 2 establishes the mechanistic foundation for alkene electro-oxidation by investigating epoxide-ketone selectivity with MnO_x,[106] indicating divergent, competing reaction pathways. Through a substrate-scope study, alkene philicity is developed as a descriptor for predicting epoxide-ketone selectivity. Complementary kinetic studies of cyclopentene oxidation and *operando* spectroscopic characterization provide further insights into the diverging mechanistic pathways of epoxidation

and ketonization, laying the groundwork for catalyst design for selective alkene ketonization.

Building on these mechanistic insights, Chapter 3 describes efforts toward catalyst screening for aqueous 1-butene ketonization by exploring a range of bimetallic catalysts, identifying bimetallic Pd–Cu as an active and selective catalyst. Two PdCu electrocatalysts prepared via co-reduction using different reductants and capping agents are compared, highlighting the importance of synthetic parameters in determining electrocatalytic performance even for catalysts of identical nominal composition.

Chapter 4 provides in-depth characterization of the more active PdCu catalyst, identifying the metallic PdCu alloy phase as the catalytically relevant phase for 1-butene ketonization. The findings along with the reactivity study of the catalyst, published in *ACS Catalysis*, establish a structure-activity relationship for PdCu-catalyzed ketonization, providing a foundation for future rational design of selective ketonization electrocatalysts.

Finally, Chapter 5 synthesizes the key findings of this thesis and discusses future directions for expanding the scope and mechanistic understanding of electrochemical alkene oxidation.

Chapter 2

EPOXIDE/KETONE SELECTIVITY IN ELECTROCHEMICAL ALKENE OXIDATION

2.1 Introduction

Ketones are commercially important chemicals widely used as solvents and synthetic building blocks in industrial manufacturing and pharmaceutical processes.[95,117] Beyond their traditional roles, ketones have attracted renewed interest as renewable liquid fuel candidates, offering a potential drop-in replacement for petroleum-based fuels within the existing energy infrastructure.[118–120] Fast pyrolysis of biomass is a major method for industrial ketone production, despite the inherent unsustainability due to the inevitable requirement of elevated temperatures.[121] Another prominent method for ketone production on the industrial scale is the Wacker-Tsuji oxidation which directly converts terminal alkenes into methyl ketones using palladium(Pd)/copper(Cu) catalysts and oxidants, such as O_2 at elevated pressures, under homogeneous conditions (Figure 2.1a).[98,99] An alternative approach to transform alkenes into ketones is a two-step catalytic epoxidation-isomerization pathway in which the epoxide undergoes a ring-opening mechanism to yield the ketone (Figure 2.1b).[122–124] However, the employment of noble-metal catalysts and stoichiometric copper leads to high costs and chemical waste. Moreover, the homogeneous nature of the processes also results in inefficient and expensive separation and recovery of the spent metal catalyst from solutions.[125] Therefore, the development of methods that can enable sustainable and cost-effective ketone manufacturing is an attractive research area. As discussed in Chapter 1, electrocatalysis allows access to reactive intermediates under mild conditions by modulating the thermodynamics of redox processes through the applied potential, and the selectivity and kinetics of heterogeneous electrocatalytic reactions are governed by the intricate interplay of catalyst surface properties, interfacial microenvironment, and reaction conditions. Therefore, the electrochemical oxidation of organic molecules represents a promising route toward sustainable chemical synthesis.[126,127]

Building on earlier work in the Manthiram group demonstrating electrochemical alkene epoxidation using pristine and Ir-decorated MnO_x nanoparticles with water as the oxygen-atom source,[106,107] this chapter focuses on understanding and ex-

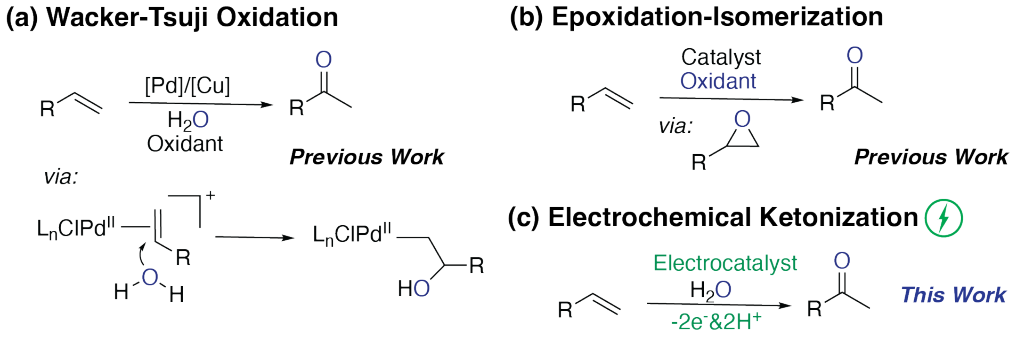

Figure 2.1: Background on alkene functionalization (a) Industrially relevant Wacker-Tsuji oxidation.[98] (b) Epoxidation-isomerization pathway to convert alkenes into ketones.[122–124] (c) (d) Envisioned electrochemical direct alkene ketonization using water as the o-atom source.

panding the product scope of this electrochemical platform. In this system, anodic voltage activates water to generate reactive oxygen species (ROS), which are transferred to the alkene substrate under ambient conditions, avoiding dangerous reagents and producing H_2 as a clean byproduct. Importantly, ketones were observed as the major organic side product in this electrocatalytic reaction, and their selectivity can be modulated via tuning the electrocatalyst. The Ir-decorated MnO_x catalyst exhibits higher epoxide selectivity than the pristine catalyst, attributed to the increased electrophilicity of the ROS upon Ir incorporation.[107] This compositional sensitivity suggests that the electronic properties of ROS are a key determinant of epoxide-ketone selectivity. As established in Chapter 1, the complexity of the heterogeneous catalyst surfaces makes it challenging to characterize active sites and gain molecular-level mechanistic insights. Homogeneous molecular catalysts, by contrast, are better understood. While a solid catalyst surface differs fundamentally from a molecular catalyst, catalysis is ultimately controlled by a molecular phenomenon, and insights from homogeneous catalysis can therefore inform the design principles for heterogeneous systems.[128,129] Thus, selectivity between alkene epoxidation and ketonization is thought through the established knowledge from homogeneous catalysis.

With metal peroxide catalysts, the oxygen transfer to alkenes leading to epoxides proceeds via nucleophilic attack by the alkene on an electrophilic oxygen atom source, with electron density donated from the π orbital of the alkene into the σ^* orbital of the O–O bond (Figure 2.2a).[130,131] In contrast, ketonization via Wacker-Tsuji oxidation requires electrophilic activation of the alkene, in which coordination

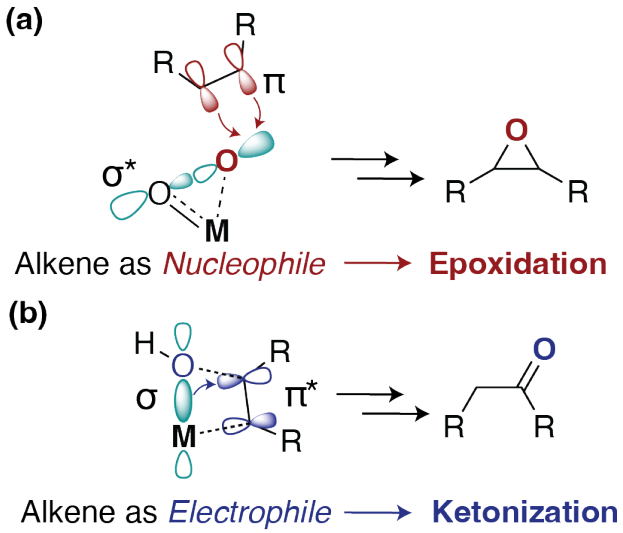

Figure 2.2: Proposed transition states for (a) epoxidation[130] and (b) ketonization.[132]

to the metal center renders the alkene more susceptible to nucleophilic attack (Figure 2.2b showing the intramolecular pathway).[99,132] By analogy, surface-bound oxygen intermediates generated from water activation could act as nucleophiles toward electrophilic alkenes, favoring the ketone pathway. This reasoning motivates the hypothesis that alkene electrophilicity is a governing factor in ketonization selectivity, meaning that more electrophilic alkenes should favor ketone formation over epoxidation, and alkene philicity may therefore serve as a candidate descriptor for predicting selectivity trends. As a preliminary test of this hypothesis, philicity indices for a small set of alkene substrates were computed using density functional theory (DFT), and the corresponding epoxide-to-ketone product ratios were determined experimentally using MnO_x nanoparticles as the electrocatalyst. While the substrate scope is limited, the results provide initial evidence for a correlation between alkene philicity and selectivity, offering a starting point for a descriptor-based approach to catalyst design. To complement the substrate-scope study and probe the underlying mechanistic basis for this selectivity, *operando* X-ray absorption spectroscopy (XAS) was employed to characterize oxidation states of the MnO_x catalyst under operating conditions with varying water and cyclopentene concentrations. These experiments provide insight into how the electronic structure of the active metal center plays an important role in governing reactivity. Notably, these findings point toward metallic, rather than metal oxide, catalysts as potentially more selective electrocatalysts for ketonization, a hypothesis explored in Chapter 3 and 4.

Additionally, initial *in situ* UV-Vis SEC experiments were undertaken in an effort to decouple the contributions of distinct redox-active surface species as well as to elucidate the nature of the interaction between the alkene substrate and the catalyst surface. While experimental challenges precluded a complete study, these attempts outline a spectroscopic approach that could, in future work, provide more direct mechanistic insights into the diverging epoxidation and ketonization pathways. The work presented in this chapter offers preliminary mechanistic insights into electrochemical alkene oxidation selectivity and motivates the transition to metallic electrocatalysts pursued in the remainder of this thesis.

2.2 Methods

MnO_x nanoparticle-loaded Electrode Preparation. The MnO_x nanoparticle-loaded carbon paper electrodes were prepared using a previously reported method.[106] In short, MnO_x nanoparticles were synthesized through a hot injection method with Mn(III) acetate dihydrate as the precursor and myristic acid and decanol as ligands, and $NOBF_4$ in DMF was used to exchange the hydrophobic ligands on the MnO_x nanoparticles. Ligand-exchanged MnO_x nanoparticles were then dispersed in ethanol as the catalyst ink, and a total of 52 μL of the catalyst ink (4×13 μL) was drop-casted on a hydrophilic carbon paper electrode which was prepared by heating disk-shape hydrophobic carbon paper in a muffle furnace at 600 °C for 1 h. The electrode was annealed at 400 °C (ramp rate of 5 °C/min) for 5 h to generate the Mn_3O_4 phase. The MnO_x electrode was naturally cooled down at room temperature and used for electrochemical experiments.

Electrochemical Methods. Electrochemical experiments were conducted using a sandwich-type one-compartment electrochemical cell with a multichannel potentiostat. Platinum foil and MnO_x loaded carbon paper were used as the counter and working electrodes, respectively. A leakless Ag/AgCl electrode was used as the pseudo-reference electrode. Aluminum foil was used as the current collector. A piece of hydrophobic carbon paper was placed behind the working electrode to prevent solvent leakage. Acetonitrile with 0.1 M tetrabutylammonium tetrafluoroborate ($TBABF_4$) was used as the solvent with varying concentrations of alkenes and water. Most of the experiments used 0.2 M of alkene and 5 M of water except for the cyclopentene- and water-dependent studies for cyclopentene oxidation. 4 mL of electrolyte was added to the electrochemical cell. The resistance at the open circuit voltage (OCV) was measured by potentiostatic electrochemical impedance spectroscopy, and all applied potentials were 85% IR-compensated automatically.

For chronoamperometry experiments, a micro magnetic stir bar was inserted into the electrolyte chamber to improve convection, and 20 C of charges were passed. Most of chronoamperometry experiments were carried out at 1.45 V vs. Fc/Fc^+, except for the Tafel studies where the potentials range from 1.05 V to 1.45 V vs. Fc/Fc^+. All cell parts including the counter electrode were thoroughly cleaned with acetone and Milli-Q water after every experiment and sonicated in 10% nitric acid solution for 15 min followed by in Milli-Q water for 5 min. All cell parts were air-dried before being used.

The leakless Ag/AgCl pseudo-reference electrode was calibrated against the ferrocene/ferrocenium (Fc/Fc^+) redox potential weekly, which was done by taking the average of the potentials of the oxidation and reduction peaks obtained via cyclic voltammetry at a scan rate of 50 mV/sec. The Fc/Fc^+ calibration was used to account for the effects of water concentration on the reference electrode potential, and the calibration solution was prepared by adding 5 mM of Fc to electrolyte solutions of varying water concentrations. The water concentration-activity relationship (Figure A.7) was established using a previously established head-space gas sampling method.[133]

Product Analysis. All products generated were analyzed and quantified using gas chromatography-mass spectrometry (GC-MS). 6 mL of brine solution was added to the post-electrolysis electrolyte, and the organic layer was extracted with 1 mL of hexane for 3 times. The internal standard 1,3,5-trimethoxybenzene (TMB) was added to the combined hexane layer, and the hexane solution was back-extracted with 2 mL of brine solution to ensure that $TBABF_4$ was completely removed from the organic phase as any residual $TBABF_4$ can lead to the risk of contamination at the injection port and the column of GC-MS. The hexane solution was analyzed by GC-MS, and external calibration curves for oxidized products (ketones and epoxides) were constructed to account for instrumentation and extraction errors (Appendix A.1). FEs were calculated using Equation 1.2 and partial current density via Equation 1.3.

DFT calculation for alkene philicity. For each alkene, the initial geometry was obtained using geometry optimization in Avogadro. Considering zero charge and multiplicity of 1 for the alkene with the total number of electrons *N*, a further geometry optimization, frequency calculation, and population analysis were performed using Gaussian 16 at M062X/def2-SVPD level of theory with acetonitrile as the implicit solvent implemented by the SMD algorithm. The free energies of the epoxide

and ketone products were calculated following the same protocol. Using the optimized geometry of the alkene, independent frequency calculation and population analysis at the same theory level were performed for the alkene with different number of electrons, N+1 (charge= -1, multiplicity = 2) and N-1 (charge = +1, multiplicity = 2), which are used to calculate the ionization potential and electron affinity of the alkene. Calculations were performed in the Resnick High Performance Computing Center at Caltech. The same methodology was also applied in Chung et al.[3]

For each alkene, the ionization potential (IP) and electron affinity (EA) are calculated using the free energies by:[134]

$$IP = E_{N-1} - E_N \tag{2.1}$$

$$EA = E_N - E_{N-1}. \tag{2.2}$$

With IP and EA, chemical potential (μ) and chemical hardness (η) of the alkene can be defined as:[135,136]

$$\mu = \frac{\partial E}{\partial N} = \frac{IP + EA}{2} \tag{2.3}$$

$$\eta = \frac{1}{2}\frac{\partial^2 E}{\partial N^2} = IP - EA. \tag{2.4}$$

The global electrophilicity index can be expressed as follows:

$$\omega = \frac{\mu^2}{2\eta}. \tag{2.5}$$

In the case of alkene oxidation, the local reactivity of the vinyl carbons is of interest. Therefore, the Fukui functions $f(r)$ are used as local density functional descriptors.[137] A higher value of $f(r)$ means higher reactivity at that atom, and we consider the vinyl carbon atoms in each alkene. Formally, $f(r)$ is defined as the spatial change in the electron density $\rho(r)$ as a function of N in the system at a constant external potential $v(r)$:

$$f(r) = (\frac{\partial \rho(r)}{\partial N})_{v(r)}. \tag{2.6}$$

$f(r)$ describing the reactivity of the atom toward *nucleophilic attack* (i.e., the atom's *electrophilicity*) (Equation 2.7) and the corresponding condensed $f(r)$ (Equation 2.8) calculated using a population analysis are defined as:

$$f^+(r) = \rho_{N+1}(r) - \rho_N(r) \tag{2.7}$$

$$f^+(r) = q_k(N+1) - q_k(N). \tag{2.8}$$

q_k is the gross population on an atom which can be obtained using the Lowdin population analysis from the cclib, an open source library for parsing and interpreting the results of computational chemistry packages.[138]

Similarly, $f(r)$ evaluating the reactivity of an atom toward *electrophilic attack* (i.e., the atom's *nucleophilicity*) and its condensed version are calculated by:

$$f^{-}(r) = \rho_N(r) - \rho_{N-1}(r) \tag{2.9}$$

$$f^{-}(r) = q_k(N) - q_k(N-1). \tag{2.10}$$

X-ray absorption spectroscopy. All XAS spectra were collected in X-ray fluorescence mode at beamline 4-1 at Stanford Synchrotron Radiation Lightsource. The electrochemical reactor used for *operando* measurements has the same geometry as the one used for bulk electrolysis studies, except for a backplate with a hole for the X-ray entrance (Figure A.5). A Kapton polyimide film was placed between the window and electrode to prevent electrolyte leakage. A semiconductor detector was employed to acquire the XAS spectra of standard materials (see Figure A.4 for preparation), while a more sensitive 30-element Ge detector was utilized for all *operando* measurements due to the low concentration of Mn in the catalyst. A standard XAS Mn foil was used to calibrate Mn edge energy. All XAS data were processed using the Athena software for background removal and normalization.

UV-Vis spectrochemistry. *In situ* UV-Vis absorption electrochemistry-spectroscopy was performed using 1 cm × 1 cm MnO_x samples on FTO substrates using a custom-built three-electrode setup. MnO_x catalyst-ink was drop-casted on the FTO substrate while being placed on a hot plate to facilitate the drying process. A Pt wire was used as the counter electrode, and a leakless Ag/AgCl electrode as the pseudo-reference electrode. The same calibration protocol from the electrolysis was applied. A stabilized 10 mW tungsten-halogen light source equipped with a collimating filter was used to illuminate the sample. The transmitted light was collected using a 1 cm diameter liquid light guide and sent to a spectrometer with a CCD camera which was always cooled to −80 °C during the measurement to ensure a high signal-to-noise ratio. A single-channel potentiostat was used to control the electrochemical settings, and a home-built web-interface was used for the data acquisition. Andor software was employed for the spectrometer and detector settings. The experimental setup is shown in Figure A.10.

2.3 Results and discussion

Correlating alkene philicity with electro-oxidation reactivity

As shown in Figure 2.1, ketonization can proceed through a direct pathway from the alkene or an indirect route via epoxide intermediate. In the case of MnO_x-catalyzed electro-oxidation, the observed ketonization is more consistent with the direct route (see A.4 for discussion), occurring in competition with epoxidation. Inspired by the reported homogeneous precedents for epoxidation with peroxide catalysts and ketonization with Pd catalysts (Figure 2.2), alkene philicity is proposed as an important factor determining the ketone/epoxide selectivity.

The local philicity of the alkene is determined by $\omega_k^\alpha = \omega f_k^\alpha$ ($\alpha = +/-$), and the average of the two vinyl carbon atoms' ω_k was assessed as the philicity descriptor. It should be noted that f^- describes the *local nucleophilicity* when the system is subjected to electrophilic attack, and ω represents the *global electrophilicity* of the system. Consequently, ω^- is a measurement of the *local electrophilicity* of the atom behaving as a nucleophile. Somewhat counterintuitively, when regarding ω^- as a descriptor of local nucleophilicity, a higher value indicates that the atom is *less* nucleophilic when facing an electrophile. ω^+, on the other hand, evaluates the local electrophilicity of the site as an electrophile, with higher values corresponding to greater electrophilicity.

As it is hypothesized that alkenes can behave as either an electrophile or a nucleophile toward an O-atom source, and those that are prone to behave as electrophiles favor ketone formation, we define a relative electrophilicity index ($\omega^{+/-}$) as the ratio between local philicity (ω^+ and ω^-). Roy *et al.* defined the ratio of local softness as the relative electrophilicity for carbonyl compounds to explain the reaction trend observed.[139] Similarly, $\omega^{+/-}$ assesses the electrophilicity of the vinyl carbons in the alkene compared to their own nucleophilicity; hence, alkenes with $\omega^{+/-}$ greater than 1 are predicted to exhibit stronger electrophilicity and to be more selective toward ketonization. The philicity and relative electrophilicity indices of various alkenes (Table 2.1) were computed to serve as a guide for choosing suitable alkenes for the substrate scope study.

Table 2.1: DFT-calculated electrophilicity (ω^+), nucleophilicity (ω^-), and relative electrophilicity ($\omega^{+/-}$)for alkenes.

alkene	**electrophilicity** (ω^+)	**nucleophilicity** (ω^-)	**relative electrophilicity** ($\omega^{+/-}$)
1-hexene	20.37	25.71	0.79
cyclooctene	15.05	18.43	0.82
cyclopentene	18.50	18.16	1.02
4.4-dimethyl-2-pentene	16.40	18.85	0.87
4-methyl-1-pentene	22.24	24.69	0.90
4,4-dimethyl-1-pentene	22.34	24.54	0.91
styrene	21.46	23.77	0.90
4-chlorostyrene	21.41	24.92	0.86
4-methylstyrene	20.82	20.15	1.03
4-fluorostyrene	21.54	23.41	0.92

Suitable substrates for the scope study were identified as those yielding detectable amounts of both ketone and epoxide as major products over MnO_x under anodic polarization. This selection criterion proved more restrictive than anticipated, and the cases of unsuitable substrates are themselves informative about the complexity of heterogeneous electrocatalysis.

Styrene and its derivatives were initially considered attractive candidates owing to their high reactivity and synthetic versatility. Compared with aliphatic alkenes, it is easier to functionalize the aryl ring to systematically tune the electronic character of the vinyl carbons. However, passing 20 C of charge at 1.45 V vs. $Fc/Fc^+$with 0.2 M of styrene yielded 2,5-diphenyltetrahydrofuran as the major product, with the expected ketone and epoxide accounting for less than 1% FE collectively (Figure 2.3a). One hypothesis for the formation of 2,5-diphenyltetrahydrofuran is that styrene is activated via chemisorption on the catalyst surface through its π system in addition to the vinyl double bond, followed by nucleophilic attack of an oxygen species, analogous to the proposed mechanism for Wacker-Tsuji oxidation. The regiochemistry of the product should be interpreted with caution, as the assignment was based on mass spectrometry alone and may not be unambiguous. Nonetheless, the formation of the bis-substituted tetrahydrofuran product indicates a second styrene molecule reacts with the OAT intermediate, likely facilitated by the high reactivity of styrene. The absence of analogous coupling product for any aliphatic alkenes tested suggests that the extended π system likely plays a role in the unexpected reactivity. On this basis, styrene and its derivatives were excluded from the substrate scope study. While this

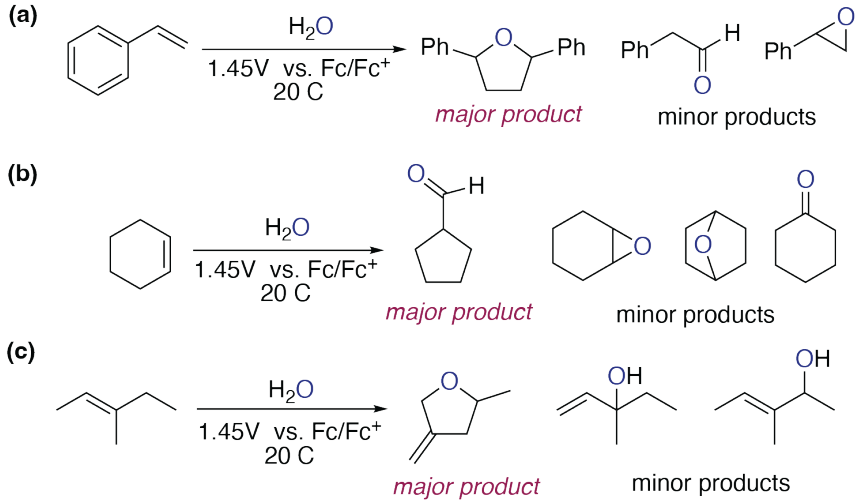

Figure 2.3: Examples of unsuitable alkenes for ketone/epoxide selectivity study. (a) Styrene (b) cyclohexene (c) 3-methyl-2-pentene.

reactivity is beyond the scope of the present work, it raises an intriguing question about how conjugated organic molecules interact with heterogeneous electrocatalyst surfaces under applied potential, which could inform catalyst design strategies that exploit synergistic substrate-surface interactions.

Another class of alkenes considered was cyclohexene and its derivatives; however, the major product observed was cyclopentanecarbaldehyde, a ring-contraction product arising from the greater thermodynamic stability of the five-membered ring (Figure 2.3b). Allylic oxidation represents another competing pathway alongside epoxidation and ketonization. This is clearly demonstrated with 3-methyl-2-pentene, a substituted internal alkene, for which alcohol products consistent with an allylic oxidation mechanism were observed under the electrochemical conditions (Figure 2.3c). Notably, the major product was 2-methyl-4-methylene-tetrahydrofuran, tentatively attributed to the internal allylic oxidation of the intermediate.

Having identified a set of alkenes that yield detectable amounts of both ketone and epoxides under the electrochemical conditions, the relationship between ketone/epoxide selectivity and the computed $\omega^{+/-}$ was examined (Figure 2.4a). A higher value of $\omega^{+/-}$ indicates that the vinyl carbons are more prone to behave as electrophiles than nucleophiles. Selectivity between ketone and epoxide formation is expressed as the ratio of their respective partial current densities. Electrolysis was carried out with 0.2 M alkene at 1.45 V vs. $Fc/Fc^{+}$with 5 M water, passing 20

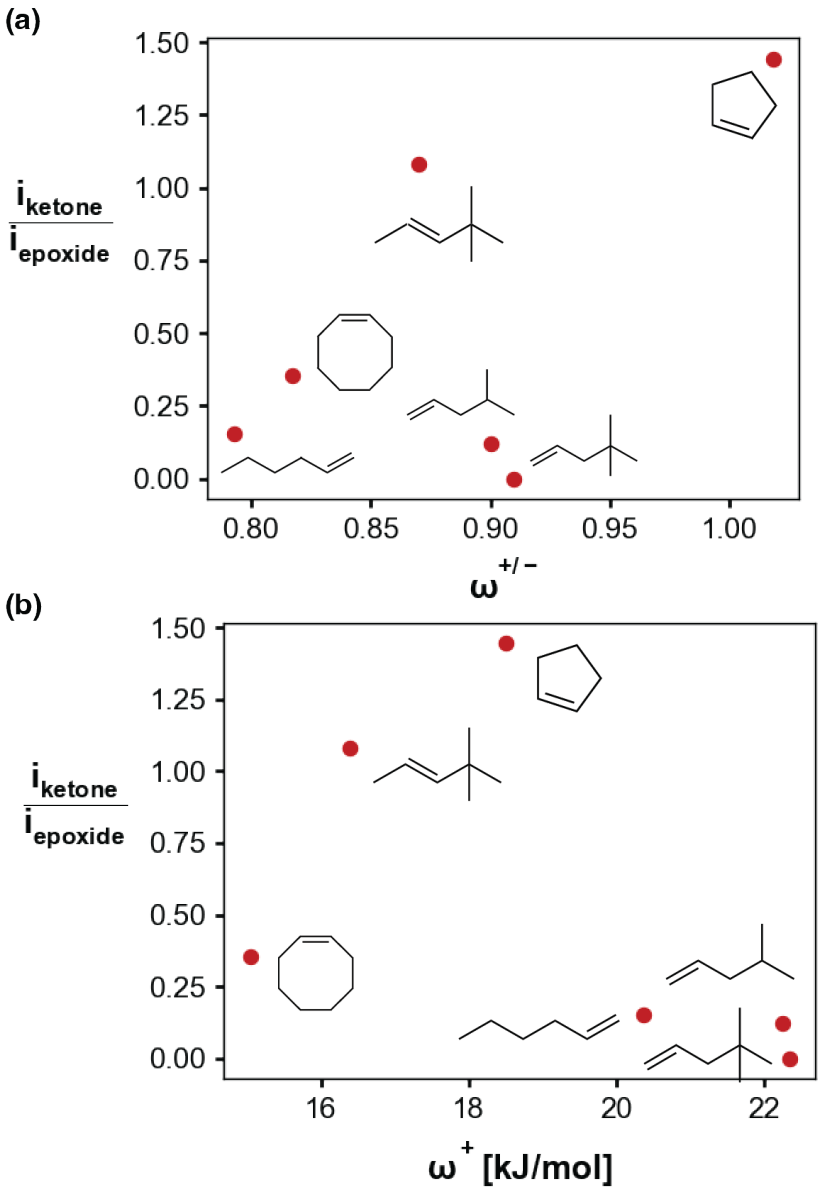

Figure 2.4: Correlation between ketone/epoxide selectivity and calculated philicity index. Partial current density ratio of ketone and epoxide plotted against (a) relative electrophilicity ($\omega^{+/-}$) and (b) local electrophilicity (ω^{+}).

C of charge. This relatively high potential was chosen since the prior observation on MnO_x that ketonization was largely suppressed at low potentials but increased at higher potentials for cyclooctene.[106]

The ketone/epoxide selectivity of 1-hexene, cyclooctene, 4,4-dimethyl-2-pentene, and cyclopentene showed preliminary consistency with the hypothesis that more

electrophilic alkenes favor ketonization over epoxidation (Figure 2.4a). However, 4-methyl-1-pentene and 4,4-dimethyl-1-pentene, for which no ketones were observed, deviated from this trend, indicating that $\omega^{+/-}$ alone is insufficient as a descriptor to fully account for the factors governing selectivity. When ketone/epoxide selectivity is plotted against the local electrophilicity index ω^{+} (Figure 2.4b), a distinction between internal and terminal alkenes becomes apparent. For internal alkenes, cyclooctene, 4,4-dimethyl-2-pentene, and cyclopentene, ketone/epoxide selectivity exhibits a roughly linear scaling relationship with ω^{+}. The terminal alkenes included in the database do not yet reveal an obvious trend, and a larger substrate set would be needed to assess whether a meaningful correlation exists within this subclass. Grouping alkenes by substitution pattern may therefore improve the descriptive power of the philicity-based framework.

An additional limitation of the philicity descriptor is that it does not capture the thermodynamic contribution to selectivity. To assess whether thermodynamic preference contributes to the observed selectivity differences, the relative free energies of the ketone and epoxide products were computed for the substrates examined (Figure A.3). While this approach provides only a rough estimate of reaction enthalpy, the relative free energy differences were found to be similar among alkenes calculated, suggesting that thermodynamic preference alone is unlikely to account for the divergence in ketone/epoxide selectivity. Furthermore, in both philicity and free energy calculations, the kinetic effects are not captured, which is a well-established contributor to the product selectivity.[140] Taken together, the preliminary substrate scope study provides initial evidence that alkene philicity correlates with ketone/epoxide selectivity, particularly for internal alkenes, while also highlighting that additional factors beyond both substrate philicity and reaction thermodynamics likely contribute to the observed product distribution.

Dependence of ketone/epoxide selectivity on reaction conditions

Among the tested alkenes, cyclopentene exhibited the highest ketone selectivity and was thus chosen for a more detailed investigation of selectivity as a function of cyclopentene concentration (Figure 2.5), water activity (Figure 2.6), and applied anodic potential (Figure 2.7). In water-acetonitrile blended electrolytes, the activity-concentration relationship for water is only proportional across a narrow range of concentrations, which can lead to misleading interpretations.[133] Thus, water activity was used in place of concentration throughout in these studies, and the corresponding activity-concentration relationship is provided in Figure A.7.

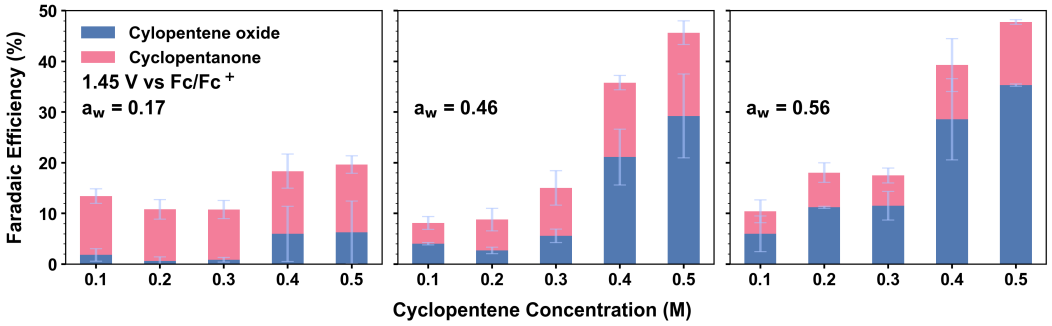

Figure 2.5: Dependence of ketone/epoxide selectivity on cyclopentene concentrations at a constant anodic potential (1.45 V vs. Fc/Fc^+) and varying water activities in acetonitrile. Water activity was varied by adjusting the water concentration: a_w = 0.17, 0.46, and 0.56 corresponds to 1 M, 5 M, and 10 M H_2O, respectively. Applied potential was 85% iR compensated.

The dependence of ketone/epoxide selectivity on cyclopentene concentration was measured at three different water activities (0.17, 0.46, and 0.56), corresponding to 1 M, 5 M, and 10 M H_2O to probe the substrate concentration effects under low, medium, and high water content (Figure 2.5). At low water concentration (Figure 2.5, left), cyclopentanone remains the preferred oxygenated product at all cyclopentene concentrations tested, with the selectivity peaking at 0.2 M cyclopentene and decreasing gradually at higher concentrations. The corresponding ketone/epoxide FE ratios are shown in Figure A.8. A similar trend is observed at medium water activity (Figure 2.5, middle) where the cyclopentanone selectivity again peaks at 0.2 M and declines with increasing substrate concentration. Notably, cyclopentene oxide becomes the major product at 0.4 M with 5 M H_2O, suggesting that higher water concentration likely creates a more favorable reaction microenvironment for epoxidation. This preference for epoxide formation at elevated water concentration is further corroborated by the high water activity case (Figure 2.5, right), where cyclopentene oxide is the predominant product across all cyclopentene concentrations tested, in contrast to the low water concentration case. Interestingly, cyclopentanone formation shows weaker dependence on the substrate concentration at low water activity than at medium and high water content, which likely arises from water being the limiting reagent under these conditions and thereby overriding the influences of substrate concentration.

The water-dependence study at 1.45 V vs. Fc/Fc^+provides further insight into the role of water activity on selectivity (Figure 2.6). At low cyclopentene concentration (0.1 M, Figure 2.6, left panel), cyclopentanone is the dominant product at water

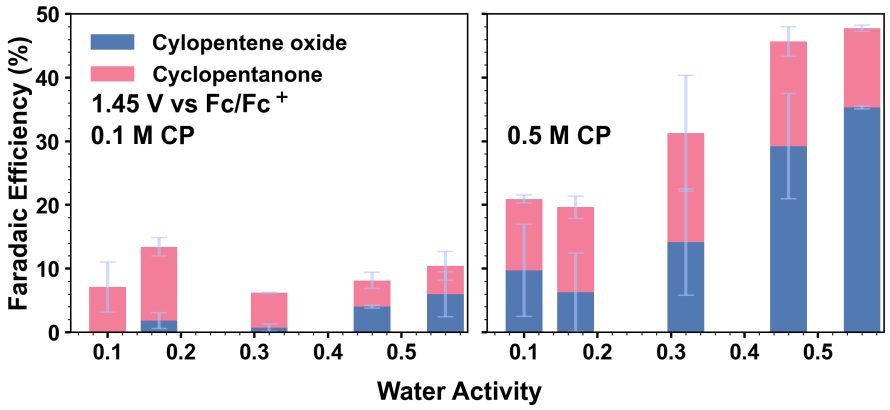

Figure 2.6: Dependence of ketone/epoxide selectivity on water activities at a constant anodic potential (1.45 V vs. Fc/Fc^+) and varying cyclopentene concentrations (0.1 and 0.5 M) in acetonitrile. Water activity was varied by adjusting the water concentration: a_w = 0.1, 0.17, 0.32, 0.46, and 0.56 corresponds to 0.5 M, 1 M, 2 M, 5 M, and 10 M H_2O, respectively. Applied potential was 85% iR compensated. CP = cyclopentene.

activity from 0.1 to 0.32 (corresponding to 0.5 M to 2 M H_2O). At high water activities, the selectivity approaches unity as the epoxide FE increases while the ketone FE decreases slightly. At high cyclopentene concentration (0.5 M, Figure 2.6, right panel), the FE for cyclopentene oxide rises sharply at higher water activities and overtakes cyclopentanone as the favored oxidized product, whereas cyclopentanone exhibits comparatively weak dependence on water activity. The large error bars observed at high water activity suggest considerable variability under these conditions, and the trend should therefore be interpreted with appropriate caution.

Considering both water- and substrate-dependence studies, cyclopentanone formation appears more strongly governed by substrate concentration than by water activity, and its production is slightly suppressed at high water content when the substrate availability is limited. One hypothesis for this observation is that high water content may lead to high surface coverage of oxygen species at the catalyst surface, which forms hydrogen bonding with the interfacial water,[36,45] limiting cyclopentene access to the catalyst surface. Alternatively, the ketone formation may proceed through a Langmuir-Hinshelwood mechanism[141] and require chemisorption of cyclopentene at the catalyst surface to increase its electrophilicity, and the overcrowding of oxygen species restricts the number of active sites available for cyclopentene adsorption, resulting in diminished ketone selectivity. In contrast, the epoxide formation likely undergoes Eley-Rideal mechanism[142] where solvent-phase cyclopentene reacts with

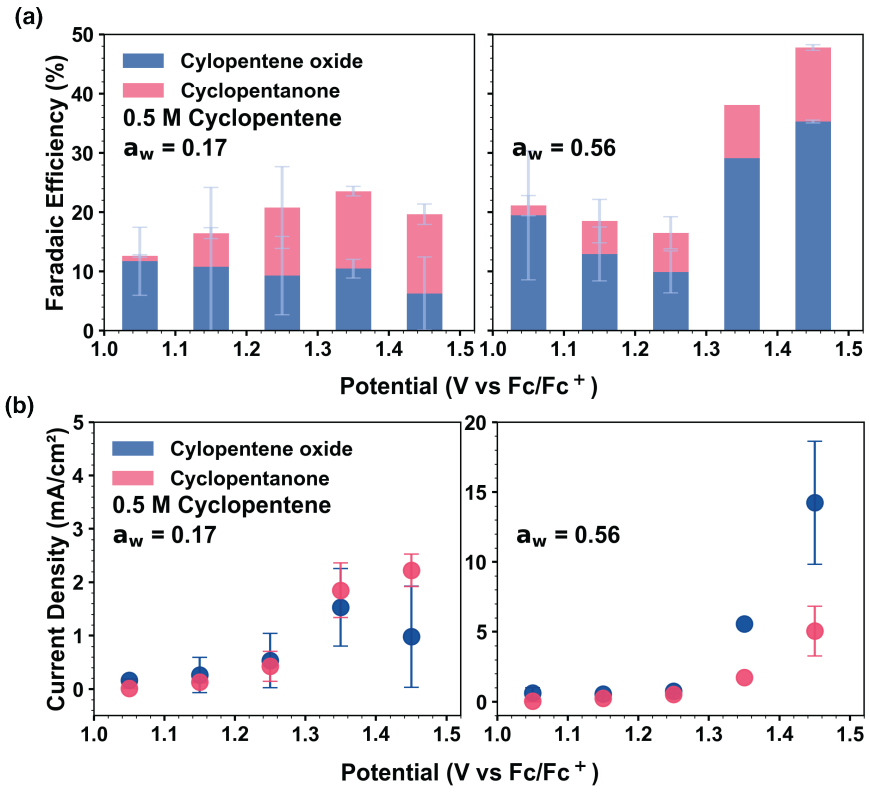

Figure 2.7: Dependence of ketone/epoxide selectivity on applied anodic potentials at a 0.5 M cyclopentene and varying water activities in acetonitrile. Water activity was varied by adjusting the water concentration: $a_w = 0.17$ and 0.56 corresponds to 1 M and 10 M H_2O, respectively. Applied potentials were 85% iR compensated.

the surface oxygen species so that its formation is enhanced with both increasing water and cyclopentene contents.[105]

The potential-dependence was conducted at 0.5 M cyclopentene and two water activities, 0.17 and 0.56, and the resulting FE and partial current densities for cyclopentene oxide and cyclopentanone are shown in Figure 2.7. At both water activities, cyclopentene oxide formation is favored at less oxidizing potentials. However, the selectivity diverges at more anodic potentials depending on water content. Under low water content, the selectivity shifts toward ketonization with increasing potential, while under high water content, epoxidation remains the preferred pathway across the entire potential range examined. The partial current densities show the rate for ketone and epoxide following the same trend with much higher current densities at high water activity. Applied potential not only modulates the surface species but also modifies the interfacial water structure.[36,143] A recent computational study suggests

that more water molecules accumulate at the interface at less oxidizing potentials.[144] At low water content (left panel), the interfacial water may therefore become increasingly scarce at more oxidizing potential, promoting cyclopentanone formation, consistent with the observation that ketonization is favored at low water activity overall (*vide supra*). At high water content (right panel), the bulk water reservoir is sufficiently large that the potential-dependent depletion of interfacial water becomes less consequential, and epoxidation hence remains dominant throughout.

In situ spectroscopic measurements

By varying the reaction conditions, ketone-epoxide selectivity of cyclopentene electro-oxidation was found to exhibit a complicated interplay of water activity, cyclopentene concentration and applied anodic potential. To gain insight into the oxidation state of the MnO_x catalyst under operating conditions, *operando* Mn K-edge X-ray absorption near-edge structure (XANES) spectroscopy was performed during cyclopentene electro-oxidation. The conditions for the *operando* measurements were selected based on the selectivity dependence studies discussed above. Low water activity (a_w = 0.17) and high water activity (a_w = 0.56) at 0.1 M and 0.5 M cyclopentene represent the conditions that yielded the most divergent ketone/epoxide selectivity and are therefore most likely to reveal differences in the catalyst oxidation state that correlate with selectivity. The corresponding FE and current density data (Figure 2.8a) reproduced from the previous section are plotted alongside the XANES spectra (Figure 2.8b) for direct comparison. The Mn K-edge absorption energy is directly correlated, shifting to higher energies with increasing oxidation state. Mn_3O_4 and MnO_2 were used as the reference standards representing Mn oxidation states of + 2.67 and +4, respectively.

The XANES spectra of MnO_x at OCV (i.e., no applied potential) closely resemble that of the Mn_3O_4 standard (Figure 2.8), indicating a similar Mn oxidation state of +2.67 as expected from the synthetic procedure.[106] The *operando* measurements at low water content (1 M or 0.17 water activity) and low cyclopentene concentration (0.1 M) showed that the bulk Mn oxidation state remains mostly unchanged under applied potentials (Figure 2.8b, left panel). This is consistent with the previous measurement in which the MnO_x was observed to experience resistance to oxidation under anodic polarization.[107] In contrast, at high water activity (10 M or 0.56 water activity), the Mn oxidation state increases drastically with applied potential (Figure 2.8b, right panel). Considering the selectivity data (Figure 2.8a, left panel), the more oxidized catalyst observed at high water activity likely contributes to the

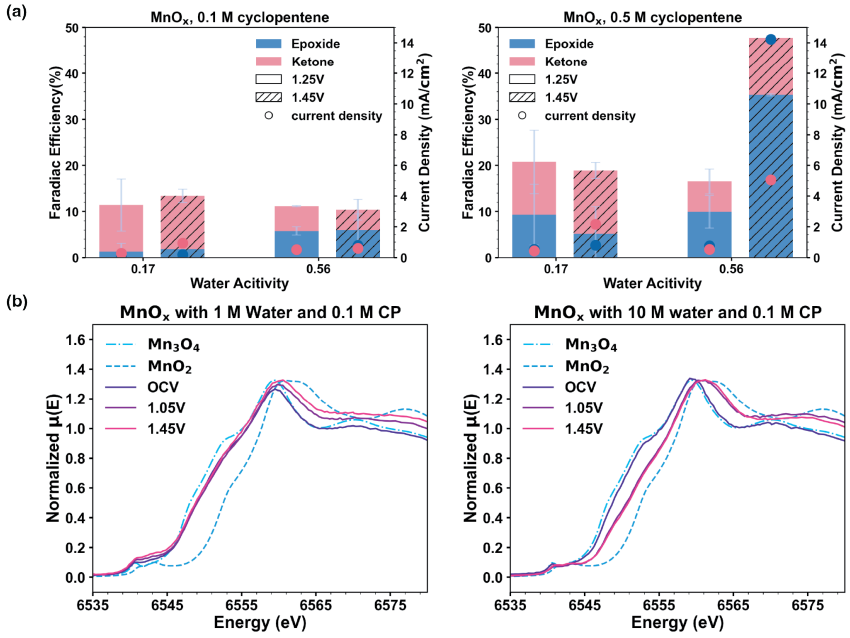

Figure 2.8: Cyclopentene electro-oxidation with MnO_x (a) Ketone/epoxide reactivity with MnO_x under different reaction conditions. a_w = 0.17 and 0.56 corresponds to 1 M and 10 M H_2O, respectively. Normalized XANES spectra focused on the Mn K rising edge, shown for *operando* samples as well as *ex situ* standard materials. CP = cyclopentene. Applied potentials were 85% *iR* compensated.

higher epoxide selectivity under these conditions, whereas the less oxidized MnO_x catalyst is associated with favored ketone formation. This result is consistent with prior observations that the more oxidized catalyst enhances epoxidation activity through increased electrophilicity of the surface oxygen species.[107]

Notably, the XANES data also implies that water facilitates the Mn oxidation (Figure 2.9a). At low water content, the average Mn oxidation state remains largely unchanged under 1.45 V vs. Fc/Fc^+, while its oxidation state increases at high water content as indicated by the pronounced change in the absorption energy, which likely arises from water participating directly in the oxidation of the catalyst surface. More surprisingly, the Mn rising edge was observed to shift slightly to higher energy at higher cyclopentene concentration (Figure 2.9b), suggesting that cyclopentene is not a fully redox-innocent reactant and may influence the redox process at the catalyst surface.

To complement the *operando* XANES measurements and probe the redox processes at the catalyst surface, *in situ* UV-Vis SEC was employed. The optical spectra of the

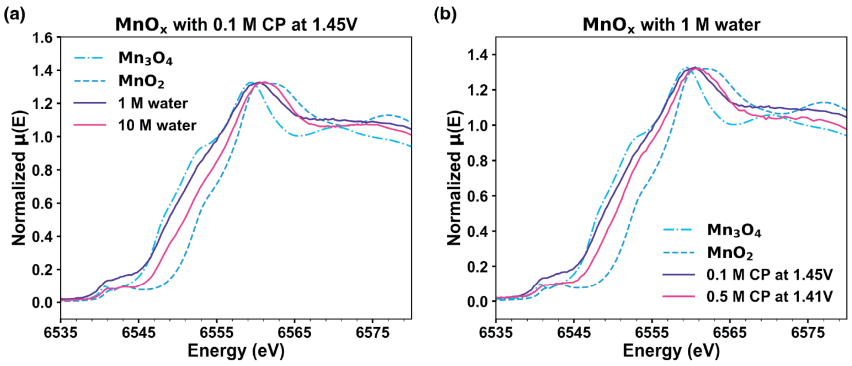

Figure 2.9: *Operando* XANES at the Mn K-edge. Shifts in XANES spectra for MnO_x at 0.1 M cyclopentene and 1.45 V vs. Fc/Fc$^+$with different water contents (a) and at 1 M water with varying cyclopentene concentrations (b). CP = cyclopentene. Applied potentials were 85% iR compensated.

catalyst were collected at 1 M water with and without cyclopentene while CV was conducted at a scan rate of 5 mV/s to capture the minute changes. Figure 2.10a shows the difference absorption spectra (referenced to 0.5 V vs. Fc/Fc$^+$) of the catalyst in 1 M water while the potential is incremented in a 1 mV step, indicating the changes in the surface speciation with the varying potential. Figure 2.10b shows the corresponding difference spectra in the presence of 0.1 M cyclopentene. In the 1 M water without cyclopentene, the broad absorption band centered at ~530 nm emerges at potentials above 0.9 V vs. Fc/Fc$^+$. Upon addition of 0.1 M cyclopentene, a similar broad absorption feature appears at lower wavelength ~480 nm, indicating the formation of different surface species in the presence of cyclopentene. The difference absorption at 550 nm as a function of applied potential (Figure A.11) more clearly shows that the onset of the redox transitions shifts to more oxidative potentials in the presence of cyclopentene, suggesting that cyclopentene likely participates in the redox process at the catalyst surface. Spectra deconvolution[37] further revealed two components with different onset potentials, indicating the likely formation of two distinct potential-dependent redox transitions. Without cyclopentene, the concentration of the first redox component grows from the beginning of the measurement until approximately 0.6 V vs. Fc/Fc$^+$, at which point a second component emerges. The presence of cyclopentene shifts this transition oxidatively to roughly 0.9 V vs. Fc/Fc$^+$.

To assess the reactivity of these potential-dependent surface species, potential decay experiments were conducted.[71] Square-wave voltammetry (SWV) was applied to

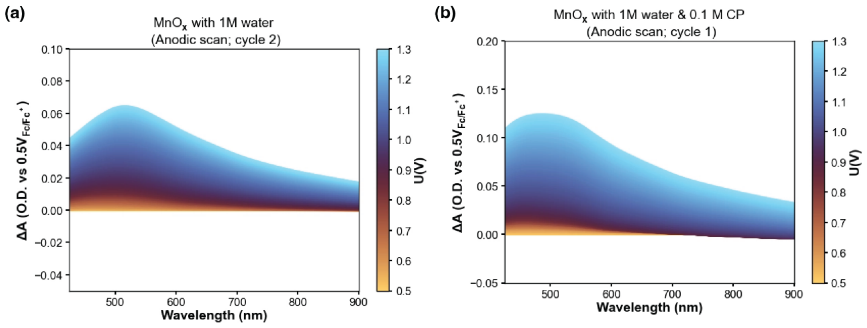

Figure 2.10: Difference absorption spectra of MnO_x during CV scan from 0.5 V to 1.3 V vs. Fc/Fc^+in acetonitrile with and without cyclopentene at a scan rate of 5 mV/s at room temperature (iR corrected). Absorption changes were collected at every 1 ms and shown every 10 mV. The difference spectra are calculated with respect to 0.5 V vs. Fc/Fc^+.

step the potential from OCV to an upper potential corresponding to a redox transition, where it was held for 20 s to allow the accumulation of the intermediate species before returning to OCV. Absorption spectra were recorded throughout to monitor the concentration of the generated species. A rapid decay in absorbance returning to OCV generally indicates the consumption of the accumulated species, thereby providing kinetic information. Figure 2.11 shows the difference spectra from the potential decay experiments conducted at two potential ranges selected based on the redox transitions identified above.

Without cyclopentene, the absence of a decay profile after returning to OCV from the first redox region suggests that the species generated at lower potentials is largely inactive toward OER (Figure 2.11a, left panel), whereas the species generated in the second redox region exhibit a clear decay indicative of reactive intermediate consumption consistent with OER (Figure 2.11a, right panel). In the presence of cyclopentene, the species formed in the first redox region shows a slightly faster decay (Figure 2.11b, left panel) than in its absence. Since this species appears inactive toward OER, the enhanced decay likely arises from cyclopentene oxidation. At higher potentials (Figure 2.11b, right panel), a fast decay between 60 s and 80 s shows the species in cyclopentene oxidation, in addition to OER.

These results provide preliminary mechanistic insight into the potential-dependent surface speciation of MnO_x and its relationship to cyclopentene oxidation. However, the interpretation is complicated by catalyst instability in the presence of cyclopentene, as evidenced by the raw absorption spectra. The observed decay profiles are

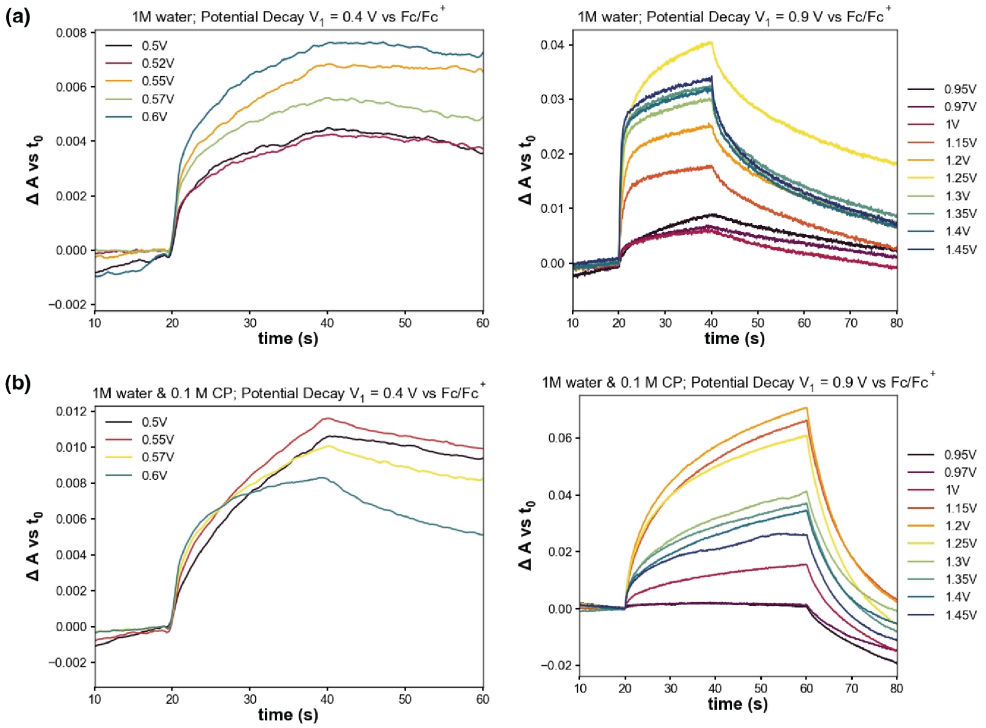

Figure 2.11: Potential decay measurements of MnO_x under varying conditions. Difference spectra at 550 nm in response to the application of square-wave voltammetry (SWV). The SWV was held at OCV for 20 sec, then at the target potential for 20 s, with the exception of (b), right panel for 40s, and finally OCV for 20 s (iR corrected).

therefore convoluted and may partly reflect catalyst degradation. Catalyst instability was found to be more pronounced at higher cyclopentene concentrations, precluding sufficient data collection for unambiguous conclusions under those conditions. The instability is attributed to the use of FTO as the substrate for the SEC measurements, required for optical transparency, in place of the porous carbon paper for electrolysis. The poor adhesion of the catalyst layer on FTO is likely responsible for the intensified degradation that was not observed in bulk electrolysis experiments.

2.4 Conclusion

This chapter investigates the epoxide/ketone selectivity of electrochemical alkene oxidation using water as the oxygen-atom source over MnO_x nanoparticle electrocatalysts. A preliminary substrate-scope study provided initial evidence that alkene philicity correlates with ketone/epoxide selectivity, particularly for internal alkenes, where a roughly linear relationship between relative electrophilicity index and se-

lectivity was observed. The electrophilicity index alone was found insufficient as a universal descriptor, and the thermodynamic preference was found to be similar across substrates, suggesting that additional factors govern selectivity.

Kinetic studies of cyclopentene oxidation revealed a complex dependence of selectivity on water activity, substrate concentration, and applied potential, with ketonization consistently favored at low water activity and low substrate concentration. *Operando* XANES spectroscopy demonstrates that the MnO_x oxidation under anodic polarization is affected by water activity, with the more oxidized catalyst at high water content correlating with higher epoxide selectivity. Initial *in situ* UV-Vis SEC experiments provide preliminary evidence for two distinct potential-driven surface redox transitions, one of which appears reactive toward both OER and cyclopentene oxidation, though catalyst instability on FTO substrates precluded more definitive mechanistic conclusions.

Chapter 3

CATALYST DESIGN AND OPTIMIZATION FOR 1-BUTENE KETONIZATION

3.1 Introduction

Identifying selective electrocatalysts for a new chemical transformation remains one of the central challenges in electrocatalysis. The difficulties of accurately measuring the actual chemical composition of an electrocatalyst and the active catalyst under operating conditions make it difficult to utilize emerging new technologies, such as machine learning, for rapid catalyst discovery.[72,145] Moreover, heterogeneous electrochemical organic synthesis lacks established design principles and fundamental understanding for most transformations beyond more extensively studied reactions, such as CO_2 reduction and OER. The electrochemical oxidation of alkenes in aqueous media presents a particularly demanding catalyst discovery problem. While the theoretical potentials for alkene oxidation, for example ketone and epoxide formation, are lower than that of OER (1.23 V vs. SHE),[146] the reported alkene oxidation, particularly epoxidation, often requires applied potential exceeding that of OER, making it a major competing pathway to the desired OAT reactions.[3,105,109] Additionally, the competing pathways among the OAT reactions further complicate the design for selective catalysts, as the identity of the ROS governs whether epoxidation or ketonization is favored, as established in Chapter 2. Rational design of catalysts for selective electrochemical 1-butene ketonization therefore navigates both the activity-selectivity tradeoff with respect to OER and the epoxide-ketone selectivity, with limited mechanistic precedent to draw from.

2-Butanone is an important industrial chemical widely used in the production of lubricants, resins and coatings, with annual global production exceeding $4 billion global market size.[95,147] Currently, 2-butanone is produced by hydration of butylene in concentrated acids at an elevated temperature.[148] Electrochemical ketonization of 1-butene using water as the oxygen-atom source represents an attractive sustainable alternative, leveraging renewable electricity to generate reactive oxygen intermediates that are otherwise challenging to access under ambient conditions. Chapter 2 establishes the feasibility of cyclopentene ketonization in acetonitrile/water blended electrolytes using MnO_x as a model system, substantiating that water-derived oxy-

gen intermediates can be selectively transferred to 1-butene, forming 2-butanone. However, the activity and selectivity of MnO_x toward ketonization remain limited, particularly in fully aqueous electrolytes. The focus of this Chapter is thus the search for more active electrocatalysts for alkene ketonization in aqueous electrolytes.

The Wacker-Tsuji oxidation, in which Pd(II) catalyzes the conversion of terminal alkenes to methyl ketones with Cu co-catalyst, provides a homogeneous analogy for the target transformation.[98] Coordination of the alkene to Pd(II) activates it toward nucleophilic attack by water, yielding the ketone via β-hydride elimination pathway (Figure 2.1a).[99,100] Furthermore, Pd-based electrocatalysts have been reported for exceptional alkene oxidation reactivity,[3,110,114,115] suggesting Pd-based materials as a promising starting point for electrochemical ketonization.

Bimetallic catalysts offer a particularly versatile handle for tuning electrocatalytic selectivity, as the introduction of a second metal modulates the electronic structure of the active sites, potentially enabling reaction pathways inaccessible on a monometallic surface and thus unlocking unexpected reactivity.[80] In the context of heterogeneous electrocatalysis, bimetallic systems can enhance reactivity through a bifunctional mechanism, in which each metal facilitates a distinct elementary step, or through electronic effects, in which the second metal perturbs the d-band structure of the active sites.[80–82] Elucidating the roles of the metals is non-trivial and requires detailed structural characterization alongside reactivity studies, which is discussed in Chapter 4. For the purposes of catalyst screening, however, the key implication is that the identity of the metal alloyed with Pd represents a tunable compositional variable that can meaningfully alter the nature of ROS at the catalyst surface and thereby modulate selectivity between epoxidation and ketonization.

This chapter describes the screening and optimization of Pd-based bimetallic electrocatalysts for aqueous 1-butene ketonization. Beginning from $PdPtO_x$/C as a benchmark, a series of Pd–M/C (M = Ru, Ni, Rh, Cu) bimetallic catalysts are evaluated, identifying Pd–Cu as the most active and selective composition. Subsequent optimization of the Pd:Cu ratio, electrolyte conditions, and electrochemical pre-activation protocol is described, culminating in the identification of a second PdCu catalyst prepared via an alternative synthetic route that outperforms the carbon-supported analogue without requiring pre-activation. The structural differences between the two PdCu catalysts were probed by XPS, revealing that synthetic conditions profoundly influence the surface oxidation states of both metals. Further detailed characterization of the more active PdCu catalyst and the establishment of

a structure-activity relationship for 1-butene ketonization are discussed in Chapter 4.

3.2 Methods

Nanoparticle-loaded Electrode Preparation. The $PdPtO_x$/C nanoparticles were synthesized following the previously established method.[3] The metallic PdPt nanoparticles were grown on Vulcan XC-72R carbon black with sodium citrate as the ligand and sodium borohydride ($NaBH_4$) as the reductant. Equal moles of metal chloride salts, 0.25 mmol $PdCl_2$ and 0.25 mmol H_2PtCl_6, were used as the precursors. $PdCl_2$ was dissolved in 5 mL of 0.1 M HCl under vigorous stirring for at least 30 min until a clear dark amber solution was obtained. H_2PtCl_6 was readily dissolved in 5 mL of 0.1 M HCl solution. Both precursor solutions were then transferred to a 500-mL round bottle flask containing 4 mmol sodium citrate dihydrate in 200 mL of Milli-Q water and charged with a magnetic stir bar. Vulcan XC-72R carbon black powder (113.1 mg) was added to the solution, and the resulting mixture was sonicated for at least 30 min to achieve uniform distribution. While the solution mixture was vigorously stirred, freshly prepared 50 mL of 0.1 M $NaBH_4$ was added drop-wise at room temperature. To avoid pressure buildup in the reacting flask, a venting needle was placed on the rubber septum. The black precipitates were collected via vacuum filtration after the reaction mixture was continuously stirred for at least 8 h post $NaBH_4$ addition. The filter paper was dried overnight in a vacuum oven at 40 °C, and the dried PdPt/C powder was collected.

PdRu/C, PdRh/C, and PdCu/C nanoparticles were prepared following the same protocol as PdPt/C with their corresponding metal chloride precursors, $RuCl_3$, $RhCl_3$, and $CuCl_2$, respectively. The bimetallic Pd–Cu on carbon materials of varying Pd:Cu ratios were prepared by changing the moles of the metal precursors while maintaining a total mole of 0.5 mmol.

The PdNi/C nanoparticles were synthesized using a hydrothermal method.[149] Instead of $NaBH_4$, NaOH and hydrazine hydrate were used as the reductants. The equimolar metal chlorides, $PdCl_2$ and $NiCl_2$, as well as 0.1 g of Vulcan XC-72R carbon black powder were dispersed in 50 mL 50%v/v water/ethanol solution by stirring for 15 min followed by 5 min of sonication at room temperature. 30 mL of 0.2 M NaOH solution was added to the mixture drop-wise and stirred for 30 min. Next, 2 mL of 85% hydrazine hydrate was added slowly. The resulting mixture was transferred into a 250 mL Teflon liner after being stirred for 2 h. The autoclave reactor was tightly

sealed and heated at 130 °C for 6 h, which was allowed to cool down to the room temperature with a cold running water bath. The resulting powder was collected via vacuum filtration and washed with an ample amount of 50%v/v water/ethanol solution. The filter paper was dried overnight in a vacuum oven at 55 °C for 6 h, and the dried PdNi/C powder was collected and used as the catalyst.

The bimetallic PdCu catalyst was synthesized via a co-reduction method that was adapted from a literature procedure.[150] Briefly, 0.25 mmol $PdCl_2$ and 0.25 mmol $CuCl_2$ solutions were combined with 1.25 mmol of trimethyl(tetra-decyl)ammonium bromide in 200 mL Milli-Q water. The solutions were cooled below 10 °C. 6 mmol of L-ascorbic acid was then added. The reaction mixture was kept cool and stirred rigorously overnight. The product was washed with abundant Milli-Q water and collected and dried at 60 °C overnight under vacuum. The catalyst powder, reddish brown in color, was collected and ground with a mortar and a pestle so that the catalyst powder had a consistent and fine texture. The powder was stored at room temperature. The pure Pd material was synthesized following the same procedure with 0.5 mmol of $PdCl_2$ and no addition of $CuCl_2$.

10 mg of the as-prepared catalyst powder was dispersed in 1 mL of water-ethanol solution (water:ethanol = 3:1 volumetric ratio) to use as the catalyst ink. A total of 100 μL of the catalyst ink was drop-casted on a carbon paper electrode. The electrode was annealed at 500 °C for 3 h to generate the oxide phase, such as $PdPtO_x$/C and $PdRhO_x$/C. Electrodes were then coated with 50 μL of 2 wt% Nafion solution and dried at 80 °C overnight.

Electrolyte Preparation. Aqueous electrolyte solutions were used in the electrochemical studies. All electrolyte formulations used 0.9 M sodium perchlorate, and the bulk pH was controlled via the 0.25 M sodium phosphate buffer. The electrolytes were prepared from 5 M $NaClO_4$ and 1 M/0.5 M sodium phosphate stock solutions. The buffer solutions were prepared by dissolving the theoretically determined amount of H_3PO_4, sodium phosphate monobasic, sodium phosphate dibasic heptahydrate, and sodium phosphate in Milli-Q water and adjusting to the desired pH value with 1 M NaOH and 1 M H_3PO_4 solutions.

Electrochemical Reaction Setup and Product Quantification. Electrochemical experiments were performed in a sandwich-style electrochemical cell in a gas-diffusion configuration with a piece of platinum foil as the counter electrode and catalyst-loaded carbon paper as the working electrode. A leakless Ag/AgCl electrode was used as a reference electrode. Aluminum foils acted as the current collectors

for both the anode and cathode. Hydrophobic carbon paper was placed behind the catalyst-loaded carbon paper to prevent electrolyte flooding. The total volume of electrolyte is 3.6 mL, and an ambient flow of 1-butene was introduced to the cell in a pass-through configuration during the bulk electrolysis.

The electrochemical measurements were conducted with a BioLogic VMP3 Multi-channel potentiostat. The solution resistance was measured at open circuit voltage (OCV) by electrochemical impedance spectroscopy techniques from 200 kHz to 100 mHz at 10 mV amplitude, and the resulting resistance determined from the x-intercept in the Nyquist plot was input for 100% iR compensation. The electrolysis experiments were conducted at fixed applied potentials for 30 minutes. The post-electrolysis electrolytes were collected and dispensed into a 5 mL volumetric flask. The electrolyte chamber was rinsed with additional Milli-Q water, which was then transferred to the volumetric flask until the total volume reached the mark. 540 μL of the electrolyte was added to a clean NMR tube in addition to 60 μL of the internal standard solution, 1 mM 3-(Trimethylsilyl)-1-propanesulfonic acid sodium salt (Fluka Chemika, 99%) in D_2O. The products were quantified using ^1H-NMR spectroscopy. The NMR spectra were acquired on a Bruker 400 MHz spectrometer with water suppression performed. The ^1H probe was automatically tuned, and the solvent lock was done with 90% H2O and 10% D_2O, and gradient shimming and auto-gain were used. 32 scans were collected per sample, and relaxation delay was set at 3 seconds.

Powder XRD analysis. The X-ray diffraction patterns of the synthesized catalysts were obtained using an X-ray powder diffractometer (Rigaku SmartLab) with Cu Ka radiation (λ =1.54056 Å). The diffraction patterns were collected from 10-90° 2θ at a step size of 0.01° and 5° per minute. Data were processed using HighScore software.

X-ray photoelectron spectroscopy. XPS measurements were collected using an AXIS Nova spectrometer by Analytical and analyzed with CasaXPS software. XPS samples were prepared by pressing the sample powders and standard materials into a 3-mm diameter pellet. After electrolysis, the electrodes were rinsed with Milli-Q water and dried under vacuum in a vacuum desiccator. The samples were directly attached to the sample platen with the platen's clips. The carbon 1s spectrum was always acquired for all the measurements so that the adventitious carbon at 285 eV could be used to calibrate the charging effect.

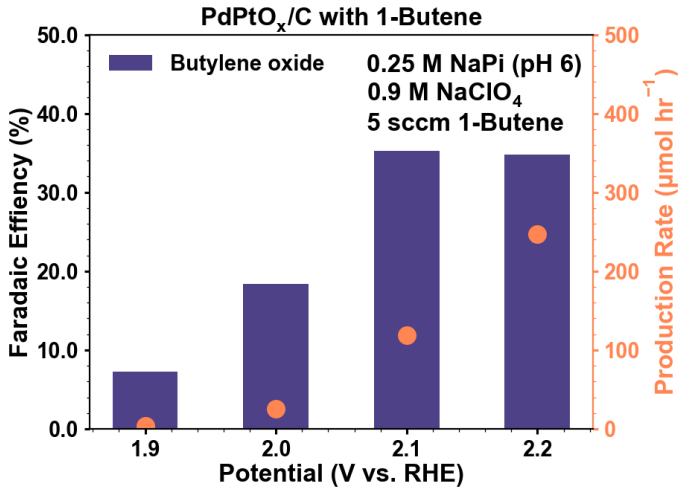

Figure 3.1: Potential dependence of electrochemical 1-butene oxidation with $PdPtO_x$/C in aqueous electrolytes. All experiments conducted in 0.25 M NaPi (pH6), 0.9 $NaClO_4$ with a constant flow of 1-butene. Applied potentials were 100% *iR* compensated.

3.3 Results and discussion

Benchmarking $PdPtO_x$/C with 1-Butene

Prior work from our group established $PdPtO_x$/C as a highly selective electrocatalyst for propylene epoxidation in both acetonitrile/water blended and aqueous electrolytes via water activation at ambient conditions.[3] Thus, we used this catalyst as a well-defined starting point for evaluating electrochemical oxidation of 1-butene, a substrate of lower aqueous solubility than propylene owing to its longer carbon chain.

Electrochemical oxidation of 1-butene was carried out with $PdPtO_x$/C under the aqueous conditions as reported in propylene epoxidation (0.25 M sodium phosphate buffer (NaPi) at pH 6, 0.9 M $NaClO_4$). 1-Butene was introduced to the catalyst surface via a gas diffusion electrode in a pass-through configuration at a constant flow rate of 5/10 sccm under ambient atmosphere. Butylene oxide was found to be the sole 1-butene-derived oxidation product across all applied potentials tested, with no detectable 2-butanone (Figure 3.1), in contrast to the competing epoxide and ketone pathways observed with MnO_x established in Chapter 2. The drastic shift in the selectivity between the two electrocatalysts demonstrates that the ketone-epoxide selectivity can be tuned through rational catalyst design. Despite low aqueous solubility of 1-butene, FEs of 40% toward butylene oxide were achieved with applied potentials above 2.1 V vs. RHE, confirming efficient mass transport in

the gas diffusion pass-through configuration.

The exclusive formation of butylene oxide confirms that the electrophilic epoxidation pathway remains operative on $PdPtO_x$/C for 1-butene, while the absence of any ketonization activity indicates that this catalyst is not suitable for the target transformation. This result is consistent with the mechanistic picture developed in Chapter 2, which attributes epoxide vs. ketone selectivity to the nature of the ROS and its interaction with the alkene substrate; the peroxo intermediates proposed for $PdPtO_x$/C are expected to favor electrophilic oxygen-atom transfer, leading selectively to the epoxide.[3] Furthermore, the selective epoxidation reactivity with $PdPtO_x$/C has been attributed to the oxidized Pt(II) species enabled through alloying with Pd. While elucidating the precise role of the individual metals in bimetallic catalysts is challenging and requires systematic studies,[80,82] the observation motivates the hypothesis that replacing Pt with a second metal that directs the reaction toward ketonization could unlock selective 1-butene ketonization on a Pd-based catalyst. The subsequent catalyst screening effort is therefore focused on Pd-based bimetallic alloys.

Catalyst Screening for 1-Butene Electro-oxidation

Having established that $PdPtO_x$/C selectively epoxidizes 1-butene, we proceeded to screen Pd-based bimetallic catalysts using the same electrochemical reaction setup. The preparation of the metallic nanoparticle catalysts is described in the Methods section, and the oxidized catalysts were obtained by annealing the as-synthesized metallic materials under static air at 500 °C for 3 h. As metal oxides are generally the active phase for OER and the oxygen-atom transfer reactions,[3,65,106,151] we first explored oxidized bimetallic catalysts for 1-butene reactivity. Among those screened (Figure 3.2a), $PdCuO_x$/C emerges as the most active, achieving ~ 3% FE toward 1-butene oxidation products at 2.2 V vs. RHE, with both butylene oxide and 2-butanone detected. $PdRhO_x$/C exhibits modest ketonization reactivity at less than 1% FE, whereas $PdRuO_x$/C and $PdNiO_x$/C show no detectable product formation under the same reaction conditions. The emergence of ketonization activity with $PdCuO_x$/C relative to the other catalysts tested suggests that the identity of the second metal can meaningfully modulate the ROS at the catalyst surface, and that the combination of Pd and Cu plays a particularly favorable role in directing 1-butene electro-oxidation reactivity.

Considering that the most selective ketonization with MnO_x was observed at the

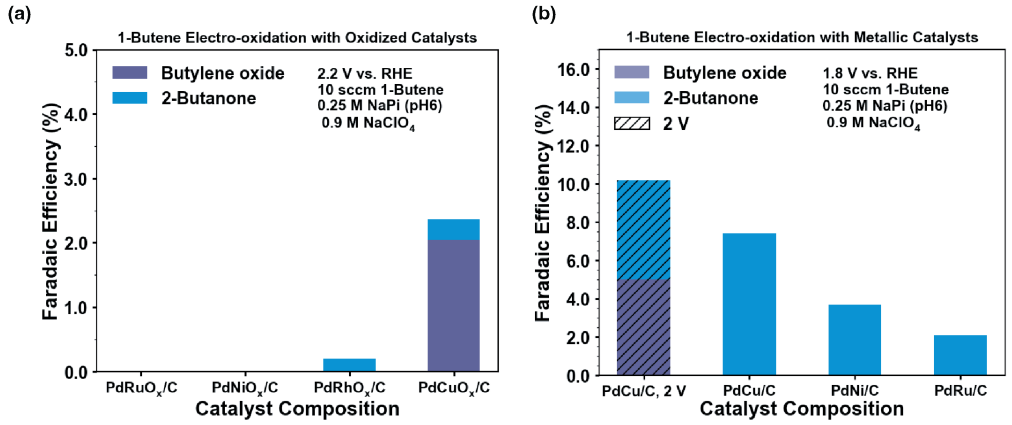

Figure 3.2: Selected Pd-based electrocatalysts for 1-butene oxidation in aqueous electrolytes. (a) Oxidized catalysts. (b) As-synthesized metallic catalysts. All experiments conducted in 0.25 M NaPi (pH6), 0.9 $NaClO_4$ with a constant flow of 1-butene. Applied potentials were 100% iR compensated.

less oxidized catalyst according to the findings in Chapter 2, the metallic analogues were investigated to assess whether the oxidation state of the catalyst influences activity and selectivity more broadly across the bimetallic series (Figure 3.2b). At 2 V vs. RHE, the metallic PdCu/C catalyst more than doubles the FE for butylene oxide and increases 2-butanone formation by over 500% relative to the oxidized Pd–Cu catalyst. Moreover, lowering the applied potential to 1.8 V vs. RHE suppresses the epoxide generation and affords a FE of 8% toward 2-butanone, revealing a potential-dependent ketone-epoxide selectivity. Given this drastic enhancement in 1-butene oxidation with the less oxidized Pd–Cu catalyst, the metallic counterparts for the other oxidized catalysts were also evaluated. Interestingly, while $PdRhO_x/C$ produces a small but detectable amount of 2-butanone, its metallic analogue was found to be inactive. In contrast, both PdNi/C and PdRu/C yield modest amounts of 2-butanone despite their oxidized phases being completely inactive, further underscoring the crucial role of the oxidation state of the catalyst on 1-butene oxidation reactivity. As PdCu/C was identified as the most active and selective catalyst for aqueous 1-butene ketonization among the compositions screened, the remainder of the chapter focuses on the further optimization of this bimetallic system.

Optimization of 1-butene ketonization with the Pd–Cu Bimetallic Catalyst

The optimization for the bimetallic Pd–Cu electrocatalytic systems began with interrogating the effects of Pd:Cu ratios, varied by adjusting the relative amounts of the

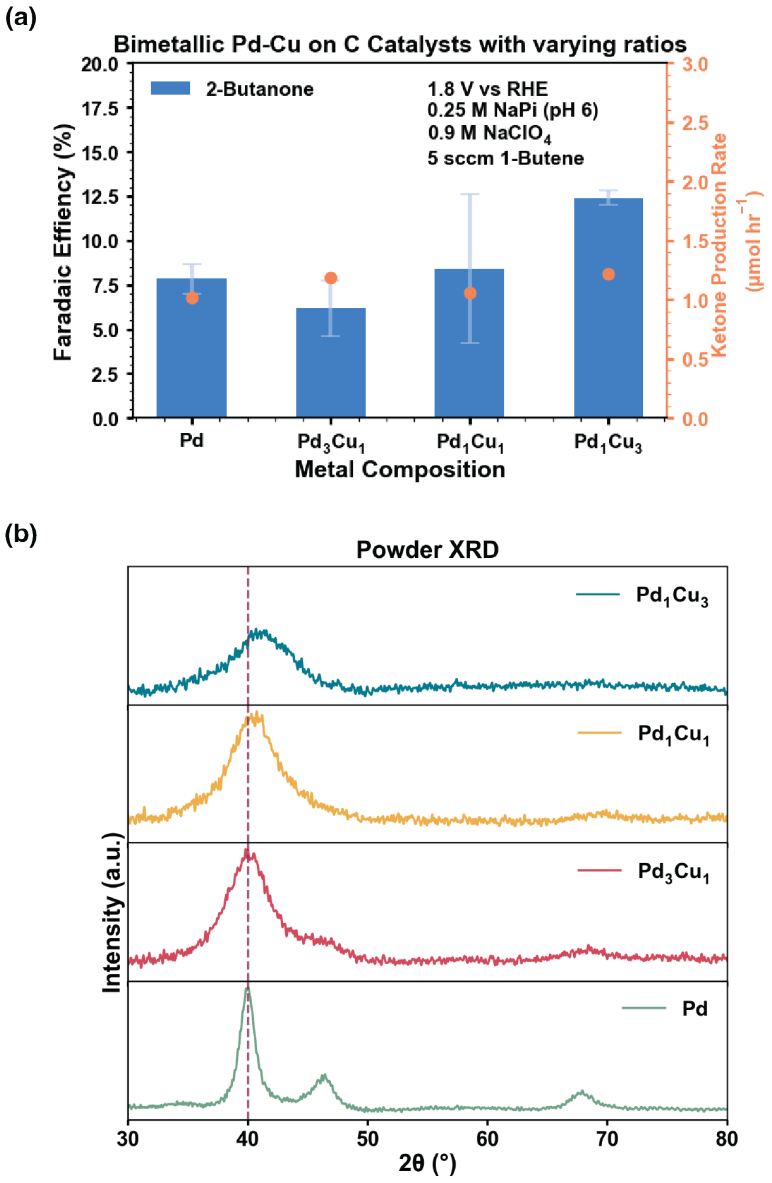

Figure 3.3: Effects of different molar ratios of Pd and Cu in PdCu/C. (a) 1-Butene ketonization with PdCu/C of varying Pd:Cu ratios. All experiments conducted in 0.25 M NaPi (pH6), 0.9 $NaClO_4$ with a constant flow of 1-butene. Applied potentials were 100% *iR* compensated. (b) XRD patterns of Pd–Cu and Pd nanoparticles grown on carbon black.

metal chlorides during synthesis. A monometallic Pd/C analogue was prepared to probe the intrinsic alloying effects of Cu on Pd. The Pd:Cu ratio was found to exert little influence on both FE and production rate for 1-butene ketonization, though Pd_3Cu_1/C and Pd/C exhibited slightly inferior performance (Figure 3.3a).

The Pd–Cu materials were characterized by X-ray diffraction (XRD) to assess their phase composition and crystallinity (Figure 3.3b). The XRD patterns of monometallic Pd/C show a metallic face-centered cubic (fcc) phase with relatively narrow diffraction peaks, indicative of a certain degree of crystallinity. The bimetallic materials likewise display diffraction features consistent with a metallic fcc phase, confirming that the alloyed materials adopt the Pd lattice and contain a mostly crystalline metallic phase. Consistent with previous findings on Cu alloying with Pd,[150,152,153] the diffraction peaks of the bimetallic catalysts systematically shift to higher 2θ values with increasing Cu contents, reflecting the contraction of the Pd lattice upon substitution of the larger Pd atoms by the smaller Cu atoms. The broader peak widths observed for the bimetallic materials relative to Pd/C suggest smaller crystalline domain sizes.

Given the almost negligible effect of Pd:Cu ratio on 1-butene ketonization, the equimolar PdCu/C catalyst was used for the subsequent optimization. Variation of electrolyte composition, including the identity and concentration of the supporting salts, yielded no meaningful improvement in either FE or the production rate (Figure B.1). Instead, a marked enhancement in performance was achieved through electrochemical activation of the catalyst prior to the reaction in the absence of 1-butene (Figure 3.4a).

Electrocatalysts are known to undergo *in situ* surface reconstruction under operating conditions due to the interaction with the electrolyte components and the external potential, and such transformation can result in the generation of the true or active catalyst phase.[154] Electrochemical pre-activation has therefore been regarded as a viable strategy for improving electrocatalytic performance.[155] For PdCu/C, pre-activation was performed by applying an oxidative square-wave potential between 1.5 and 2.5 V vs. RHE at 0.1 Hz, transiently oxidizing the catalyst surface. Pre-activation for 15 min increases the FE from roughly 15% to 18%, and the treatment for 30 min further improves the FE to ~20%, while the partial current density for 2-butanone remains around 0.2 mA/cm^2 (Figure 3.4a).

The macroscopic changes of the PdCu/C-loaded electrode after the electrochemical oxidation were shown in Figure B.2. Compared to the pristine electrode, the ac-

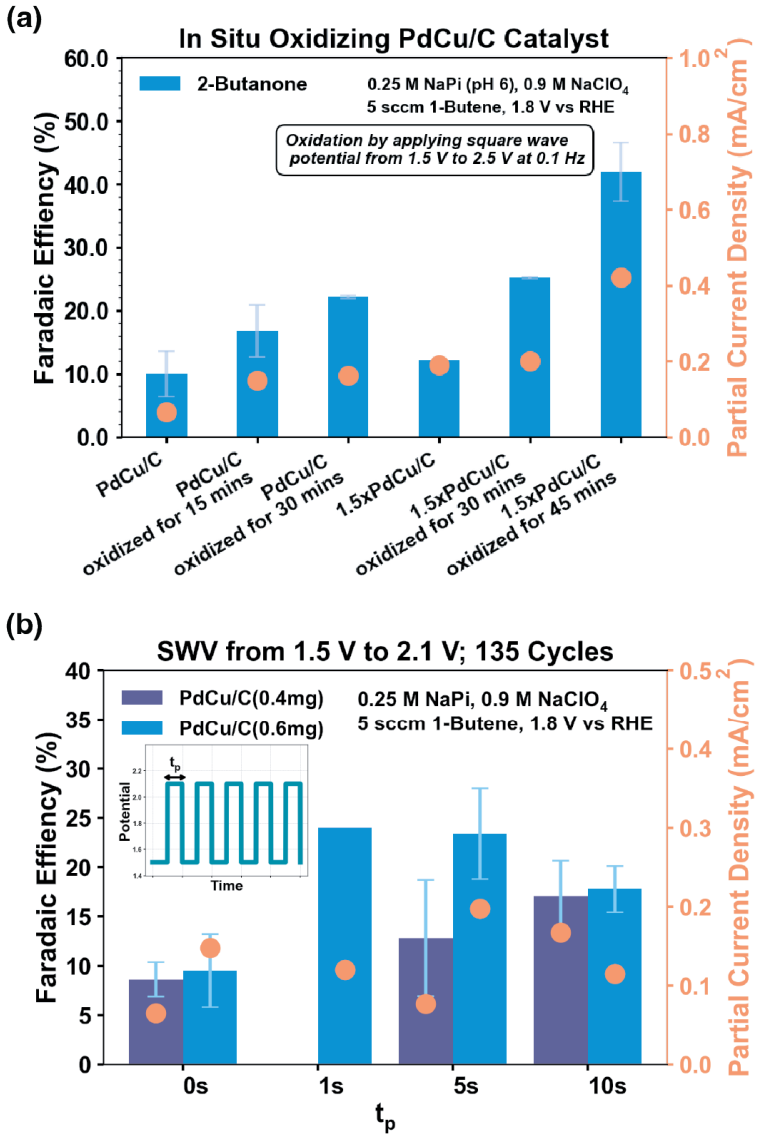

Figure 3.4: Effects of *in situ* electrochemical pre-activation via SWV on 1-butene ketonization by PdCu/C. (a) Varying conditions to test the pre-activation conditions. (b) Effects of time interval for potential pulse (t_p) with two catalyst loadings. The inset shows the schematic of the square-wave potential waveforms. All experiments conducted in 0.25 M NaPi (pH6), 0.9 $NaClO_4$ with a constant flow of 1-butene. Applied potentials were 100% iR compensated.

tivated electrode exhibits a uniformly distributed catalyst layer covering the entire electrode area exposed to the electrolyte. Such visible morphological changes suggest that the catalyst likely undergoes significant restructuring during the activation by square-wave voltammetry (SWV). To probe the effect of the pre-activation on the electrochemical properties of the catalyst, cyclic voltammetry (CV) was conducted for the pristine and activated PdCu/C in the presence of 1-butene (Figure B.3). Notably, the oxidative pre-activation suppresses the OER activity, shifting the OER current takeoff by approximately 0.4 V to more anodic potentials. Since OER is a competing pathway, the reduced OER activity of the activated catalyst likely results in the observed enhancement in ketone formation. In addition, the electrochemical treatment can also improve the catalytic performance by generating more active sites, as catalysts have been reported to become amorphous and contain abundant sites after electrochemical cycling.[156] Consequently, double-layer capacitance (DLC) was measured to estimate the electrochemically active surface area (ECSA) (Figure B.4). The similar DLC values of the pristine and activated PdCu/C catalyst indicate that the pre-activation does not significantly increase the number of accessible active sites. Therefore, the observed improvement in ketonization activity arises from the changes in the intrinsic activity of the active sites generated from oxidative treatment, rather than from an increase in their surface density.

The catalyst with higher metal loading (1.5 × PdCu/C) was also evaluated. In comparison to PdCu/C, the pristine 1.5 × PdCu/C catalyst does not improve the FE but approximately doubles the partial current density, likely due to the greater number of active sites accessible to 1-butene at higher catalyst loading. However, the 30 min of activation does not further enhance the ketonization reactivity and rate for 1.5 × PdCu/C, suggesting that the electrochemical conditioning may create a new catalyst phase with a similar number of active sites regardless of the original loading. Extending the pre-activation to 45 min significantly enhances the ketonization performance, achieving ~40% FE and 0.4 mA/cm^2 partial current density, consistent with the interpretation that the intrinsic reactivity and the number of active sites are governed by the extent of reconstruction induced by the electrochemical conditioning. Collectively, the results indicate that a moderate degree of surface oxidation induced by the square-wave treatment is beneficial for 1-butene ketonization by forming the catalytically active phase.

To further probe the role of dynamic surface oxidation, the effect of the potential pulse time interval (t_p) was investigated (Figure 3.4b). The potential was pulsed

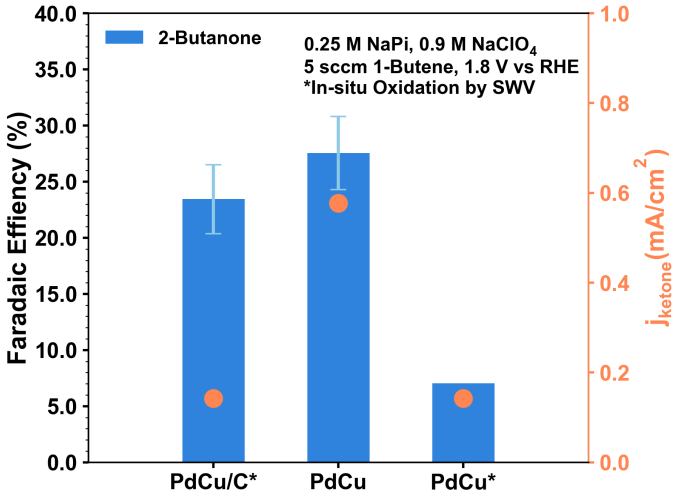

Figure 3.5: Comparison of the two Pd–Cu electrocatalysts, PdCu/C and PdCu.

at 1.5 V to 2.1 V for 135 cycles, and the ketonization reactivity was subsequently assessed by CA at 1.8 V vs. RHE for 30 min. For PdCu/C, t_p values of 1 s and 5 s yield the highest FE of approximately 25%, while a longer interval (t_p = 10 s) results in lower FE and partial current density. In contrast, the ketonization performance of higher loading catalyst is improved with increasing t_p, suggesting that the optimal activation protocol is loading-dependent and that generating the active surface phase requires a greater degree of oxidative treatment at higher catalyst loadings.

Despite the improvement afforded by pre-activation, this approach presented several practical limitations. The pre-activation process was not consistently reproducible, with variable current responses and total charge passed between experiments, making controlled generation of the active surface phase difficult. Furthermore, the partial current density toward 2-butanone does not exceed 0.2 mA/cm^2 for the standard loading catalyst, constraining the overall ketonization activity. These limitations motivated exploration of alternative synthetic routes to obtain more active and reliable Pd–Cu catalysts.

A PdCu catalyst prepared via co-reduction at reduced temperature[150] was found to exhibit superior ketonization performance relative to PdCu/C without requiring pre-activation (Figure 3.5). Whereas PdCu/C was prepared by growing alloyed nanoparticles on carbon black using $NaBH_4$ as the reductant and sodium citrate as the capping agent, the alternative PdCu catalyst was prepared without carbon support using a milder reductant, L-ascorbic acid, and trimethyl(tetradecyl)ammonium bromide as the capping agent, with the reaction maintained below 10 °C for 14–16

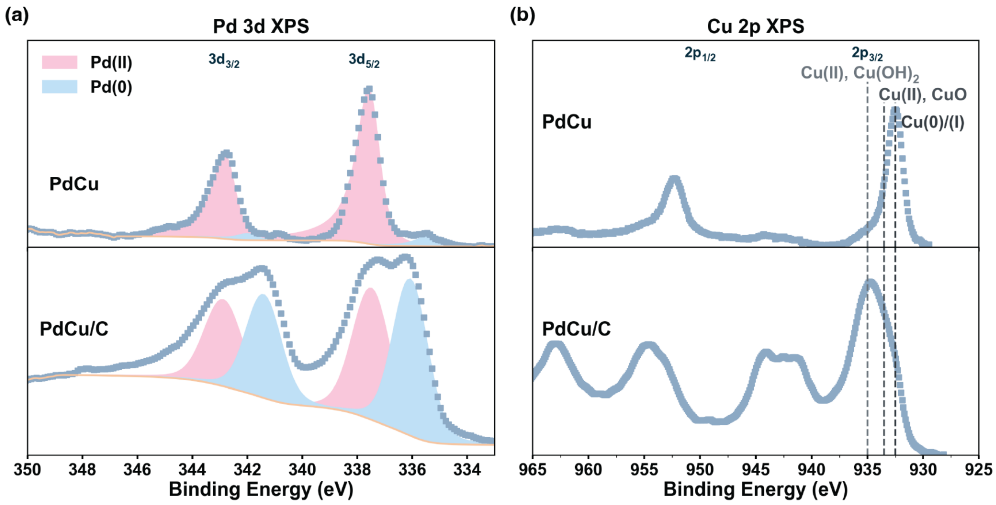

Figure 3.6: Normalized Pd 3d (a) and Cu 2p (b) XPS spectra of PdCu and PdCu/C.

h. Interestingly, the application of the same square-wave pre-activation procedure to PdCu diminishes its performance relative to the pristine catalyst (Figure 3.5), indicating the synthetic condition already generates the active catalyst phase and that further oxidative treatment is counterproductive.

To understand the structural origins of this difference in reactivity, X-ray photoelectron spectroscopy (XPS) was utilized to characterize the oxidation states of the surface species in both catalysts (Figure 3.6). The Pd 3d spectrum of PdCu/C reveals approximately equal contribution from both Pd(0) and Pd(II), with a Pd(0) $3d_{5/2}$ binding energy at 335.8 eV (Figure 3.6a).[157] Notably, the Pd(II) binding energy in PdCu/C is shifted roughly 1 eV higher than that characteristic of Pd(II) in oxides.[157–159] This energy shift is consistent with a PdCuO solid solution where smaller Cu^{2+} ions are substituted for larger Pd^{2+} ions, resulting in the lattice contraction and higher binding energy.[153] This observation indicates that Cu^{2+} and Pd^{2+} are likely mixed within an oxidized alloy phase at the PdCu/C surface. In contrast, PdCu is predominantly composed of Pd(II) species in the alloy phase, with little Pd(0) character. The Cu 2p XPS spectrum of PdCu displays a main peak at 933 eV ($2p_{3/2}$), attributable to Cu(0)/Cu(I),[160,161] with only a slight rise in the shakeup region around 940 and 963 eV, indicating a minor contribution from Cu(II). In contrast, PdCu/C exhibits a prominent Cu(II) shakeup satellite feature and a pronounced $2p_{3/2}$ peak at 935 eV assignable to $Cu(OH)_2$, indicating a substantially more oxidized Cu surface.

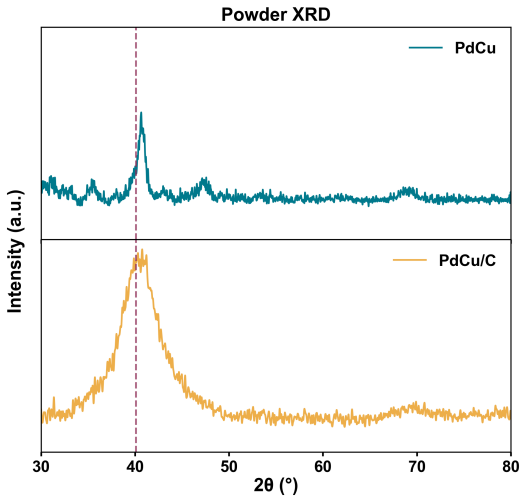

Figure 3.7: XRD pattern for PdCu and PdCu/C.

Overall, the surface-sensitive XPS reveals that PdCu/C presents a more oxidized Cu surface but a higher proportion of metallic Pd(0) relative to PdCu, whereas PdCu contains predominantly Pd(II) with less oxidized Cu species. Interestingly, the XRD pattern of PdCu displays a similar alloyed fcc phase as PdCu/C (Figure 3.7), indicating the presence of the metallic alloy phase in the bulk. As the oxide phase is absent in the XRD patterns for both PdCu and PdCu/C but detected by XPS, both catalysts likely contain an amorphous oxidized alloy phase in addition to the fcc metallic alloy phase. Moreover, PdCu exhibits larger crystalline domains of the metallic phase, as evidenced by the narrower XRD peaks relative to PdCu/C. While the surface Pd(0) species in PdCu is present in lesser proportion than Pd(II) by XPS, the fcc phase in XRD and the detection of the less oxidized Cu species together suggest the metallic phase persists at and below the surface. The difference in the relative oxidation states of the two metals between the two catalysts, arising solely from differences in synthetic conditions, highlights how sensitively the electronic structure and catalytic performance of bimetallic systems depend on the synthetic procedures.

3.4 Conclusion

This chapter describes the screening and optimization of Pd-based bimetallic electrocatalysts for aqueous 1-butene ketonization. Benchmarking with $PdPtO_x$/C confirms that the ketone-epoxide selectivity is strongly catalyst-dependent, motivating a systematic screening of Pd–M bimetallic compositions with PdCu/C identified as the most active and selective catalyst. Electrochemical pre-activation via SWV was

found to enhance activity by generating a more active surface, albeit with limited reproducibility. An alternative PdCu prepared via co-reduction under mild conditions was observed to surpass the performance of pre-activated PdCu/C without requiring additional activation, demonstrating that synthetic parameters are a critical determinant of electrocatalytic performance even for catalysts of nominally identical composition. The structural origins of the superior ketonization activity of PdCu are investigated in detail in Chapter 4.

Chapter 4

METALLIC PD–CU ALLOY PHASES DRIVE SELECTIVE HETEROGENEOUS ELECTROCHEMICAL KETONIZATION OF 1-BUTENE

The material in this chapter is adapted from Jiang, C.; Moss, B.; Lindenfelser, A.; Kim, J. T.; Li, Y.; Manthiram, K. Metallic Pd–Cu Alloy Phases Drive Selective Heterogeneous Electrochemical Ketonization of 1-Butene. *ACS Catalysis* **2026**, *16*, 7429–7438, DOI: 10.1021/acscatal.5c08675. Reproduced with permission from the American Chemical Society.

4.1 Abstract

Electrification of 2-butanone synthesis via ketonization of 1-butene offers a viable pathway to reduce emissions associated with its production as a commodity chemical and to enhance its prospects as a clean carbon-based synthetic fuel. However, direct electrochemical ketonization of alkenes remains underexplored, with previous studies largely limited to epoxides and glycols. Herein, we report an electrochemical heterogeneous system optimized for 1-butene ketonization, converting 1-butene to 2-butanone using a bimetallic PdCu catalyst in aqueous electrolytes. The system achieves a Faradaic efficiency of 20% and a partial current density of 0.6 mA/cm^2 at 1.8 V_{RHE}. In comparison to monometallic Pd and oxidized PdCu analogs, the PdCu catalyst doubles ketonization Faradaic efficiency and quadruples the production rate. Post-electrolysis characterization reveals that PdCu preserves the surface metallic alloy phase under anodic polarization, which likely accounts for the enhanced ketonization activity. This work demonstrates the significance of the Pd–Cu speciation dynamics and provides a framework for designing selective electrocatalysts for alkene ketonization.

4.2 Introduction

Electrifying the chemical industry and transportation sector is a step toward achieving carbon neutrality and reducing reliance on fossil fuels, as electricity from renewable sources is becoming increasingly available and falling in cost.[162] Rather than relying on elevated temperature and pressure, electrochemistry employs applied voltage to drive chemical reactions, offering a more sustainable alternative

to commodity chemical production. Therefore, electrochemical technologies have emerged as a promising strategy for generating clean carbon-based synthetic fuels compatible with existing energy infrastructure.[163] One potential target for electrochemical synthesis is 2-butanone. In addition to its commercial value (∼ $4 billion global market size[147]), 2-butanone is a promising synthetic fuel candidate for spark-ignition engines due to its high knock resistance and gasoline-like enthalpy of vaporization.[119] Industrial production of 2-butanone is commonly achieved via a high-temperature hydration of butylene in concentrated acids, an energy-intensive process.[148] Electrification could, in principle, reduce the emissions associated with 2-butanone production, enhancing its viability as a sustainable synthetic fuel.

A particularly attractive pathway to electrify 2-butanone production is through electro-oxidation of 1-butene. Direct alkene electro-oxidation, achieved by means of water activation over heterogeneous electrocatalysts at ambient conditions, has garnered considerable attention.[104] This electrochemical approach not only replaces the energy-intensive conditions of traditional thermochemical methods but also utilizes water as the oxygen-atom source without the need for stronger, explosive oxidants, such as hydrogen peroxide.[3,89,106–111,114,115,164] However, selective ketonization in alkene electro-oxidation remains significantly underdeveloped, in comparison to other processes like epoxidation. Moreover, propylene oxidation has been the primary focus owing to the high industrial value of propylene oxide and propylene glycol. While ketones are observed particularly with Pd-based electrocatalysts,[109–111,114] this reactivity has been frequently attributed to homogeneous reactions catalyzed by dissolved Pd species from catalyst corrosion rather than true heterogeneous catalysis.[111,114] Additionally, more selective epoxidation electrocatalysts, such as Pd-Pt alloys, have been observed to largely suppress ketonization.[3] While theoretical and empirical investigations have revealed possible potential-dependent selectivity in electrochemical oxidation of alkenes,[110,115] suggesting that the ketone selectivity can be tuned through rational catalyst design and external voltage control, heterogeneous electrocatalytic systems specifically focused on selective alkene ketonization have yet to be reported.

By contrast, several non-electrochemical routes for converting alkenes to ketones are known. Wacker-Tsuji oxidation, a well-studied homogeneous alkene ketonization reaction, employs a $PdCl_2$ catalyst with a $CuCl_2$ co-catalyst.[98,100] Similarly, Pd–Cu immobilized on zeolites has been demonstrated for thermal heterogeneous catalysis.[101,102,116] Building on these precedents, we sought to explore electro-

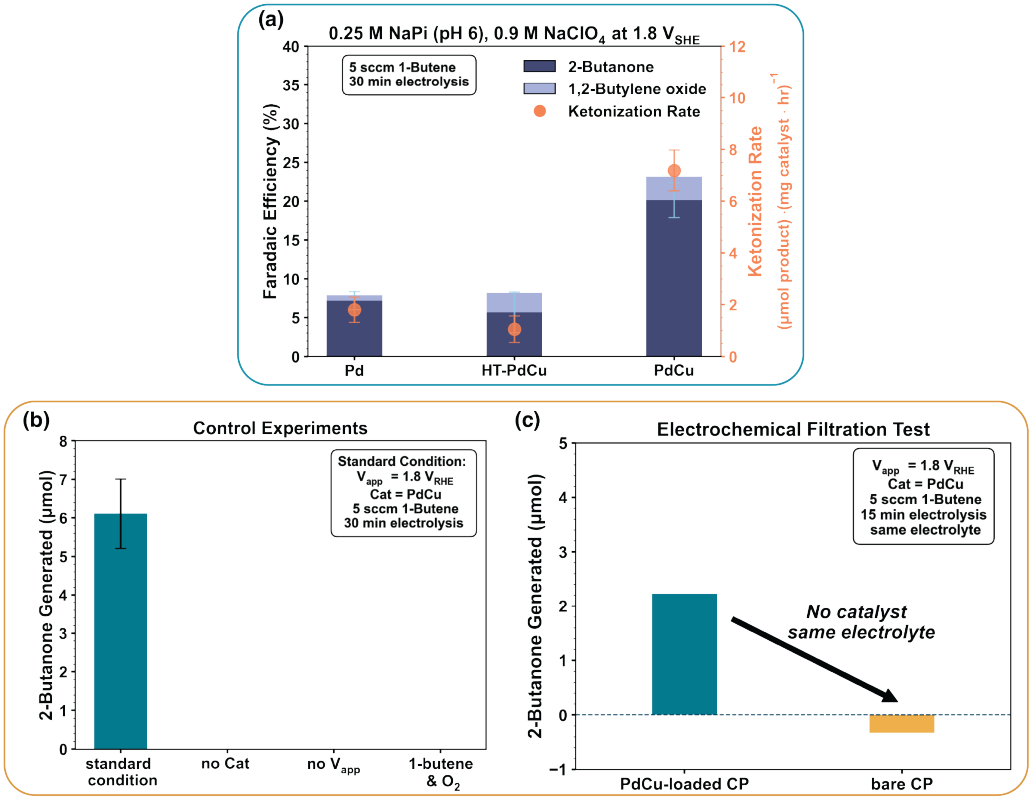

Figure 4.1: Electrochemical oxidation of 1-butene over Pd, PdCu, and HT-PdCu (heat-treated pre-oxidized PdCu). (a) Faradaic efficiency and ketone production rate for direct electrochemical 1-butene ketonization with Pd-based and Cu-based catalysts in aqueous electrolytes Control experiments on PdCu (b) and the electrochemical filtration test (c) used to confirm the electrochemical and heterogeneous nature of the catalysis. In (c) the standard experiment is interrupted and bare carbon paper loaded in place of CAT-CP and the experiment continued. The negative value with bare CP may arise from product loss from transferring the electrolyte out of and back to the electrochemical cell. Error bars represent standard deviations from the mean of multiple replicates ($n \geq 3$) using fresh electrodes for each measurement. Applied potential was 100% iR compensated.

chemical alkene ketonization by heterogeneous Pd–Cu alloys in aqueous electrolytes.[150,165–168] We selected 1-butene as the substrate and 2-butanone as the target product, owing to its industrial relevance and potential application as a synthetic fuel. The aqueous electrochemical oxidation of 1-butene is inherently more challenging than that of propylene as a longer carbon chain results in lower solubility in water, limiting 1-butene availability at the electrode surface. Furthermore, increased carbon chain of alkene is associated with reduced reactivity in heterogeneous catalysis.[168–171] Propylene epoxidation is more difficult than ethylene epoxidation due to the activated allylic C-H group, which makes side reactions yielding acrolein and allyl alcohol more facile.[169–171] By extension, 1-butene electro-oxidation presents even greater challenges regarding both reactivity and selectivity.

Herein, we present a catalytic system optimized for heterogeneous ketonization of 1-butene using an electrocatalyst derived from a bimetallic PdCu alloy. Under electrochemical conditions, Cu-based catalysts are known to undergo dynamic surface reconstruction, which is challenging to predict due to local electric field effects and pH swings at the electrode-electrolyte interface.[172–174] Such surface evolution can present both beneficial and detrimental influence on catalytic performance, leading to either enhanced activity or deactivation.[151,154,175] We therefore characterized the catalysts in both their pristine state and after bulk electrolysis with 1-butene to gain insights into the effects of the evolution of the catalysts on ketonization and to inform future catalyst design.

4.3 Results and discussion

Establishing the PdCu catalyst and heterogeneous electrochemical 1-butene ketonization

As previous studies on alkene electro-oxidation indicate that ketonization is likely favored with metallic catalysts,[110,114] we prepared a PdCu catalyst via co-reduction of $PdCl_2$ and $CuCl_2$ with ascorbic acid at 10 °C following a literature procedure.[150] The monometallic Pd analog was prepared using the same method with PdCl2 as the sole precursor to isolate the effects of alloying. While metallic Pd favors ketonization in electrochemical alkene oxidation, Pd(II) has been proposed as the catalytically active species in heterogenized thermochemical Wacker-Tsuji oxidation.[98,100] Thus, we also prepared a pre-oxidized sample of PdCu, which we refer to as HT-PdCu, by annealing PdCu in static air at 400 °C for 3 h. Catalyst-loaded carbon paper electrodes were fabricated by drop-casting the catalyst ink and subsequently coating with Nafion.[3] Electrochemical experiments were conducted using a home-built,

three-electrode gas diffusion cell operated in a flow-through configuration, identical to that used in our previous study.[3]

Catalytic performance was evaluated by chronoamperometry at 1.8 V_{RHE} in a pH 6 electrolyte (0.25 M sodium phosphate (NaPi) and 0.9 M $NaClO_4$) under an ambient flow of 1-butene. Products were quantified with ^1H nuclear magnetic resonance (NMR) spectroscopy using sodium trimethylsilylpropanesulfonate as the internal standard. The monometallic Pd catalyst showed poor performance, achieving less than 10% Faradaic efficiency (FE) for 2-butanone, and the pre-oxidized sample, HT-PdCu, meant to replicate oxidation states effective for thermochemical Wacker-Tsuji oxidation, demonstrated similarly low FE. Interestingly, relative to Pd and HT-PdCu, PdCu achieved twice the FE and a fourfold increase in the production rate for 2-butanone (Figure 4.1a). Furthermore, the less oxidized catalysts, Pd and PdCu, displayed substantially higher selectivity toward 2-butanone, with ketone-to-epoxide ratios of 6:1 and 5:1, respectively, compared to 2:1 for HT-PdCu. The improved ketone selectivity indicates the significance of the less oxidized catalyst surface in ketonization, as proposed in previous studies,[109,110] and hints at a reaction pathway distinct from the thermochemical route driven by high valent Pd(II). The pronounced enhancement in ketonization activity of PdCu in comparison to Pd further suggests that mixing Pd–Cu is likely to play a key role in facilitating the observed ketonization reactivity.

Since $PdCl_2$and $CuCl_2$ are known to co-catalyze alkene oxidation under molecular oxygen (O_2) in the homogeneous Wacker-Tsuji pathway,[98]one might attribute the observed ketonization in the PdCu electrocatalytic system to non-electrochemical or homogeneous reactions arising from dissolved Pd species in the electrolyte, as suggested in previous studies.[111,114] To interrogate the nature of 1-butene oxidation in this system, we conducted a series of control experiments (Figure 4.1b and c). We verified that 1-butene oxidation by PdCu occurs through an electrochemical rather than a thermochemical pathway, given that no products were detected in the absence of anodic potential (Figure 4.1b). Because O_2 acts as the oxidant in the Wacker-Tsuji oxidation and can be generated *in situ* under operating conditions, particularly at higher potentials, it is plausible that O_2-mediated thermal oxidation could contribute to the observed ketone formation. However, when a mixed 1-butene/O_2stream ($P_{1-butene} = P_{O_2} = 0.5$) was introduced without applying anodic potential, no products were detected, thereby excluding the thermal O_2-mediated pathway. Inductively coupled plasma (ICP) analysis showed minimal leaching of

Pd and Cu into the post-electrolysis electrolyte (0.2 ppm and 6.5 ppb, respectively). To further rule out the contributions from any dissolved species, we conducted an electrochemical "filtration test" following our previous protocol (Figure 4.1c).[2] Halfway through electrolysis, the catalyst-loaded carbon paper was replaced with bare carbon paper. The same electrolyte was reused, and the electrolysis was then resumed. No additional products were detected after swapping the catalyst-loaded carbon paper, consistent with the control experiment in the absence of the catalyst (Figure 4.1b). Collectively, these results corroborate that the observed 1-butene oxidation reactivity originates exclusively from a heterogeneous electrochemical process on the PdCu surface.

The role of potential and pH

Having established the efficiency and heterogeneous nature of 1-butene ketonization in the PdCu electrocatalytic system, we next examined the effects of applied potential and electrolyte pH. Considering the possible evolution of the catalyst surface during anodic polarization, a freshly prepared catalyst-loaded carbon paper was used for each electrolysis experiment to eliminate any influence from the sample history. Electro-oxidation of 1-butene with PdCu generates several organic products with 2-butanone, 2-oxobutanol, 1,2-butylene oxide, and 1,2-butanediol as the major products (Figure 4.2a). Products were identified using ^1H-NMR (see Figure C.4 for NMR assignment). Figure 4.2b shows the potential-dependent product selectivity at pH 6, alongside oxygen evolution reaction (OER) current density obtained via chronoamperometry in the absence of 1-butene. OER was especially evident at potentials more anodic than 1.9 V_{RHE}. The partial current density toward each product at each potential is provided in the Appendix B (Figure C.5).

Until 1.8 V_{RHE}, the FE for 2-butanone remains nearly constant at ~20%, then decreases above 1.9 V_{RHE}, coinciding with the onset of the OER current. 2-Oxobutanol follows a similar trend with an FE of approximately 10% prior to the onset of OER. We note that 2-butanone was the only detectable product at 1.5 V_{RHE}, indicating that the formation of the other products requires a higher overpotential. Above 1.9 V_{RHE}, the epoxidation activity leading to 1,2-butylene oxide surpasses ketonization, and its partial current density closely trends with the OER current. One possible source of 2-oxobutanol is the overoxidation of 1,2-butanediol. However, the ratio of 2-oxobutanol to 1,2-butanediol decreases with more oxidizing potentials, inconsistent with the overoxidation hypothesis (Figure C.8a). As both the FE and partial current density for 2-oxobutanol exhibit a similar trend as 2-butanone (Figure

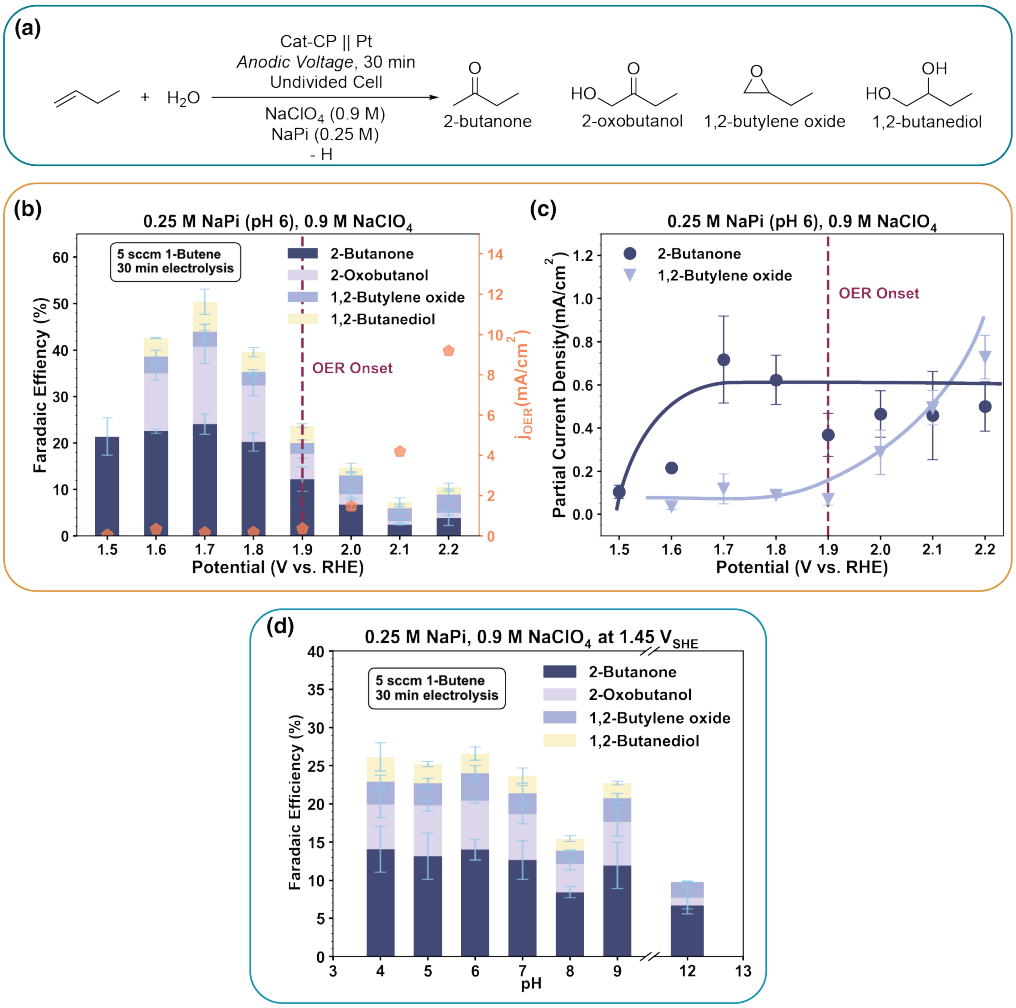

Figure 4.2: Potential- and pH-dependence of electrochemical oxidation of 1-butene by PdCu (a) Reaction scheme showing the major organic products in 1-butene oxidation observed. (Cat-CP: catalyst-loaded carbon paper). Potential-dependence of the FEs of PdCu (b) and the partial current densities (c) for 2-butanone and 1,2-butylene oxide. The solid lines are guides for the eye. (d) Dependence of the FE of the PdCu catalysts on pH. Potentials in this figure were 100% iR corrected. Error bars represent standard deviations calculated from the mean of multiple replicates ($n \geq 3$) with fresh electrodes for each measurement. Applied potentials were 100% iR compensated.

4.2b & C.5), we speculate that 2-oxobutanol is likely formed through a related reaction pathway as 2-butanone.

Given the involvement of multiple reaction pathways and the participation of either $\cdot OH/OH^-$ or H^+ species, we investigated the pH-dependence of the reaction. The pH of the electrolyte has little impact on either ketonization or epoxidation between pH 4 and 7 and at pH 9 under 1.45 $V_{SHE,}$ while pH 8 and 12 result in diminished overall product generation (Figure 4.2d). In contrast to previous observations of a Pd-Pt alloy catalyst optimized for propylene epoxidation, where a higher amount of propylene glycol is detected at more acidic pHs due to more facile acid-catalyzed hydrolysis,[3] the PdCu system at 1.45 V_{SHE} does not show an apparent selectivity toward 1,2-butanediol under acidic conditions (Figure C.8d). Additionally, no 1,2-butanediol was detected at pH 12. The lack of correlation between 1,2-butanediol and 1,2-butylene oxide suggests that 1,2-butanediol was not generated through epoxide ring opening but more likely via a direct glycol pathway due to allylic activation.[111,114]

Our potential-dependence data show that ketonization is favored at lower potentials, consistent with previous Pd-based propylene electro-oxidation studies.[110,114,176] Ketonization on PdCu exhibits a potential dependence with a Tafel slope of 131 ± 38 mV/dec (Figure C.6) that attenuates at more oxidizing potentials within the OER regime (Figure 4.2c). This behavior contrasts sharply with that of epoxidation, which shows the opposite trend of potential independence below OER onset potential and a stronger potential dependence in the OER regime (Tafel slope = 96 ± 25 mV/dec, Figure C.6). The saturation behavior of ketonization is unlikely to arise from mass-transport limitations as supported by theoretical mass transport analysis (Appendix B. Analysis of transport limitation). The weak dependence of partial current densities on both potential and pH suggests that ketonization with PdCu is likely to be limited by a thermochemical step, such as the oxygen-atom transfer to 1-butene or hydrogen-atom migration leading to 2-butanone.

Pristine and Post-electrolysis Catalyst Characterization

To better understand the superior performance of PdCu in 1-butene ketonization, we investigated the structural and electronic differences among Pd, PdCu, and HT-PdCu. The chemistry at the catalyst-electrolyte interface is dynamic and varies drastically from the bulk electrolyte under operating conditions.[28,37,177] For example, the local pH at the catalyst's surface during alkene electro-oxidation could be

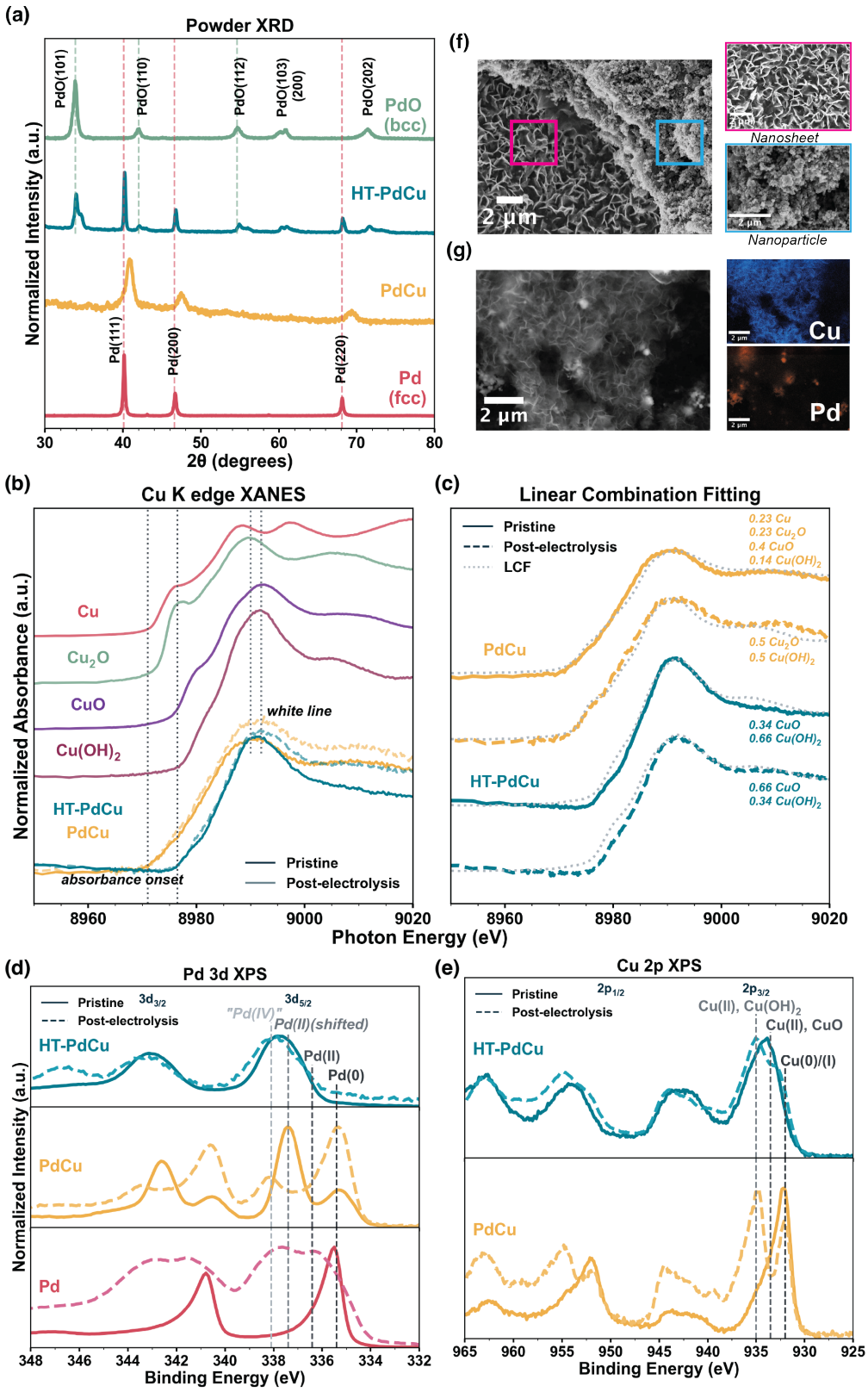

Figure 4.3: Characterization of Pd, PdCu, and HT-PdCu. (a) XRD patterns. fcc —face-centered cubic; bcc—body-centered cubic (b) Normalized XANES data, shown *ex situ* spectra for pristine and post-electrolysis PdCu and HT-PdCu as well as standard Cu materials. (c) Linear combination fitting (LCF) for PdCu and HT-PdCu using the spectra of Cu standard materials. Alternative fittings are provided in Appendix B (d and e) Normalized Pd 3d and Cu 2p XPS spectra of Pd, PdCu,

lower than in the bulk electrolyte as protons accumulate during the generation of reactive oxygen species, which could lead to Cu leaching. However, dissolution may also be associated with catalyst reconstruction that, in some cases, can promote activity.[151,175,178] On the other hand, reconstruction may act as a deactivation pathway, converting active reaction sites into inactive ones.[179] Understanding the changes of pristine catalysts under electrochemical conditions is therefore critical to future optimization of electrocatalytic systems. Accordingly, we characterized both the pristine and post-electrolysis Pd, PdCu, and HT-PdCu catalysts. The post-electrolysis samples were collected after bulk electrolysis under standard conditions (chronoamperometry at 1.8 V_{RHE} for 30 min in an electrolyte of pH 6 with 1-butene). Details on the sample preparation for characterization are provided in Appendix B. Catalyst characterization.

X-ray diffraction (XRD) patterns show that pristine PdCu exhibits diffraction peaks closely resembling face-centered cubic (fcc) Pd metal (Figure 4.3a). Consistent with previous findings on Cu alloying with Pd,[150,152,153] the diffraction peaks of PdCu systematically shift to higher 2θ values due to the incorporation of the smaller Cu atoms into the Pd lattice. Furthermore, the broader peaks for PdCu suggest smaller crystalline domains. The HT-PdCu displays a set of diffraction patterns corresponding to a body-centered cubic (bcc) PdO lattice in addition to the fcc Pd, corresponding to the less oxidized metallic alloy phase (Figure 4.3a). This suggests that HT-PdCu is partially oxidized with both oxide and metallic phases present. Both fcc Pd and bcc PdO phases in HT-PdCu shift to higher 2θ values, albeit to a lesser extent than in PdCu, which could point to a lower degree of Cu and Pd alloying due to partial phase segregation during thermal treatment.[180] The sharpness of these peaks can be attributed to larger crystallite sizes of the particle at higher temperatures.[152,157,181] In summary, the XRD analysis revealed that PdCu has a relatively crystalline metallic fcc structure, whereas HT-PdCu contains a mixture of metallic fcc and oxidized bcc phases with larger crystalline domains.

The broadness of the peaks in XRD hints at the presence of amorphous phases. To examine the nature of the Cu species in PdCu and HT-PdCu, we employed X-ray absorption near-edge spectroscopy (XANES) at the Cu K edge to probe the oxidation states of Cu on both pristine and post-electrolysis samples. Figure 4.3b shows the XANES spectra of PdCu and HT-PdCu alongside standard Cu materials. The absorbance onset of pristine and post-electrolysis PdCu occurs around 8970 eV, within the range of less oxidized Cu species, Cu(0) and $Cu(I)_2O$. However,

the white line position of PdCu lies close to that of Cu(II) materials, Cu(II)O and Cu(II)$(OH)_2$, indicating a mixture of Cu species with varying valencies. To deconvolute the spectra, linear combination fitting (LCF) was performed using the standard spectra. The original and LCF spectra are shown together in Figure 4.3c. Based on LCF analysis, bulk PdCu likely consists of roughly 20% Cu(0) and 20% Cu(I) species in addition to Cu(II). Given that the XRD pattern of PdCu only detects a metallic fcc phase, the more oxidized Cu phases could have been more amorphous and undetectable by XRD. After electrolysis, the bulk PdCu becomes slightly more oxidized, as Cu(0) is no longer found in the fitting. LCF analysis for pristine and post-electrolysis HT-PdCu indicates predominantly Cu(II) species. However, we were unable to obtain a better fitting for the rising edge region; the fits for the rising edge region were offset by about 3 eV relative to the experimental spectra. This could suggest that HT-PdCu might contain Cu species that are slightly more oxidized than the Cu(II) due to the electronic effects of Pd and are not fully captured by the reference standards.

As the surface is the most critical region of the catalyst, we then turned to X-ray photoelectron spectroscopy (XPS) to interrogate oxidation states of the surface species. Figure 4.3d and 4.3e show *ex situ* XPS spectra of Pd, PdCu, and HT-PdCu in both pristine and post-electrolysis states (peak deconvolution is provided in Appendix B. Peak modeling for X-ray photoelectron spectroscopy). The pristine Pd catalyst is predominantly Pd(0), with a Pd $3d_{5/2}$ binding energy at 335.5 eV, and contains approximately 10% of Pd(II) at 336.5 eV.[157] Interestingly, the pristine PdCu exhibits a dominant Pd $3d_{5/2}$ peak (Pd(II) shifted) in the range of the binding energy characteristics of Pd(II)[157–159] but with a substantial increase of 1 eV in comparison to the Pd catalyst. This peak is also present in HT-PdCu. Such an energy shift may have resulted from the substitution of smaller Cu^{2+} atoms for larger Pd^{2+}atoms as observed in PdCuO solid solution.[153] It has been suggested that as the lattice contracts due to the substitution, the increase in Madelung energy leads to a higher binding energy.[153] This observation indicates that Cu^{2+} and Pd^{2+} are likely mixed in an oxidized alloy phase at the catalyst surface. In addition, the pristine HT-PdCu contains another component at a binding energy of 338 eV, which can be tentatively assigned as Pd(IV) based on literature reports.[182–184] The formal 4+ oxidation state is known to be unstable for Pd in solution. Although a highly oxidized species could be plausibly stabilized at the surface, such an assignment would require systematic studies. We emphasize that this assignment is tentative and does not imply a true +4 valency; the label "Pd(IV)" is used solely to indicate the tentative assignment.

Post-electrolysis spectra are shown in dashed lines in Figure 4.3 to allow direct comparison with pristine materials. After being subjected to oxidative potential, the Pd catalyst surface becomes significantly oxidized with the emergence of Pd(II) and the "Pd(IV)" components. In contrast, HT-PdCu exhibits less pronounced change after electrolysis, as further oxidation of Pd species in HT-PdCu is unlikely. Most remarkably, in surprising contrast to Pd(II) as the main species in the pristine PdCu, Pd(0) becomes the dominant species in the post-electrolysis PdCu, in addition to the appearance of the Pd(IV) component.

The Cu 2p XPS spectrum of the pristine PdCu (Figure 4.3e) exhibits a main peak at 933 eV ($2p_{3/2}$) with asymmetry likely arising from a mixture of Cu(0)/Cu(I) at 931 eV and Cu(II) in CuO at 933 eV.[153,160,161] The shake-up features, which stem from valence excitation in paramagnetic states, around 940 and 963 eV are characteristic of Cu(II).[160,161] It should be noted that Cu(0) and Cu(I) are largely indistinguishable in Cu 2p XPS, especially in the presence of a substantial amount of Cu(II).[160] While Cu(I) species are detected in the bulk structure by XAS, we cannot definitively include the presence of Cu(I) at the catalyst surface. After electrolysis, the PdCu surface shows the emergence of a new peak at 934.8 eV, assignable to Cu(II) in $Cu(OH)_2$.[160] In HT-PdCu, Cu is predominantly present as Cu(II), and the $Cu(OH)_2$ peak is also observed on the post-electrolysis surface. Notably, the Cu(0)/(I) remains detectable on the PdCu surface after electrolysis. Overall, less oxidized Cu surface species are present in both pristine and post-electrolysis PdCu surfaces, in addition to the emergence of $Cu(OH)_2$ after electrolysis. In contrast, the HT-PdCu surface contains mostly CuO in the pristine state and both CuO and $Cu(OH)_2$ after electrolysis.

As XPS data unveils the formation of new species at the catalyst surfaces after electrolysis, scanning electron microscopy (SEM) was utilized to investigate morphological changes in the catalyst-loaded carbon paper electrodes. SEM images of post-electrolysis PdCu and HT-PdCu electrodes indicate the formation of a nanosheet structure (Figure 4.3f and g). Nanosheet structures are not observed in the pristine PdCu and HT-PdCu, suggesting that these surface features are likely to be induced by the applied potentials and the interaction with the electrolyte. Potential-driven reconstruction of Cu oxides to hydroxides has previously been observed, associated with sheet and wire-like growth habits.[185] Elemental mapping constructed from energy-dispersive X-ray spectroscopy (EDS) shows a significant phase separation within the nanosheet structure (Figure 4.3g). The nanosheet primarily consists of

Cu and hence is assigned to $Cu(OH)_2$, whereas the Pd signals are concentrated on nanoparticle clusters. In addition to the nanosheet clusters, the post-electrolysis PdCu retains nanoparticle morphologies (Figure 4.3f), resembling those of pristine PdCu (Figure C.21) and presenting a more uniform Pd and Cu distribution (Figure C.22, Figure C.24, C.25, C.26, C.27 for HRTEM-EDS). By contrast, the nanoparticle features are not found in the post-electrolysis HT-PdCu.

In summary, bulk- and surface-sensitive characterization techniques reveal that PdCu catalysts contain multiple phases with varying degrees of oxidation (Figure 4.3). Cu(I) and Cu(II) species are detected in bulk by XAS but are absent in XRD, suggesting that PdCu likely contains amorphous oxide phases along with the fcc metallic alloy phase observed by XRD. The shifted Pd(II) peak in the photoemission spectrum of PdCu indicates the presence of a surface oxide-alloy species in addition to a surface fcc metallic alloy component (Figure 4.4a). While it is difficult to differentiate Cu(0) and Cu(I) in XPS with a considerable amount of Cu(II),[160] the detection of Pd(0) by XPS in both pristine and post-electrolysis PdCu suggests that Cu(0) is more likely, as it would be energetically favorable to form the PdCu alloy. Moreover, the observation of the shifted metallic fcc phase (Figure C.28), rather than pure fcc Pd(0), in the post-electrolysis PdCu by XRD, further supports the presence of the metallic alloy. The absence of the Cu(0) component in the fitted XANES spectrum of the post-electrolysis PdCu (Figure 4.3 c) may be explained by the localization of the less oxidized Cu phase at the catalyst surface, as indicated in the Cu 2p XPS spectrum, rendering it undetectable by XAS. Thermal treatment of the PdCu leads to the mixed-phased HT-PdCu, consisting of the fcc metallic alloy and bcc oxide phases (Figure 4.4b). As Pd(0) is not observed in XPS, the metallic phase is likely to be concentrated in the bulk rather than at the surface.

Under operating conditions for 1-butene oxidation, the PdCu catalyst exhibits higher selectivity and activity toward 2-butanone formation compared with HT-PdCu. Specifically, ketonization of 1-butene was enhanced twofold in selectivity and fourfold in rate with PdCu (Figure 4.1a). Considering that the HT-PdCu surface appears more oxidized due to thermal treatment, the improvement in ketonization with PdCu indicates that the native metallic or less oxidized character of the surface PdCu species is likely to play a crucial role in ketone formation, in agreement with previous studies on alkene electro-oxidation with propylene.[109,110] The difference in activity between PdCu and HT-PdCu, therefore, suggests a catalyst-phase-dependent selectivity between epoxidation and ketonization. Additionally, PdCu

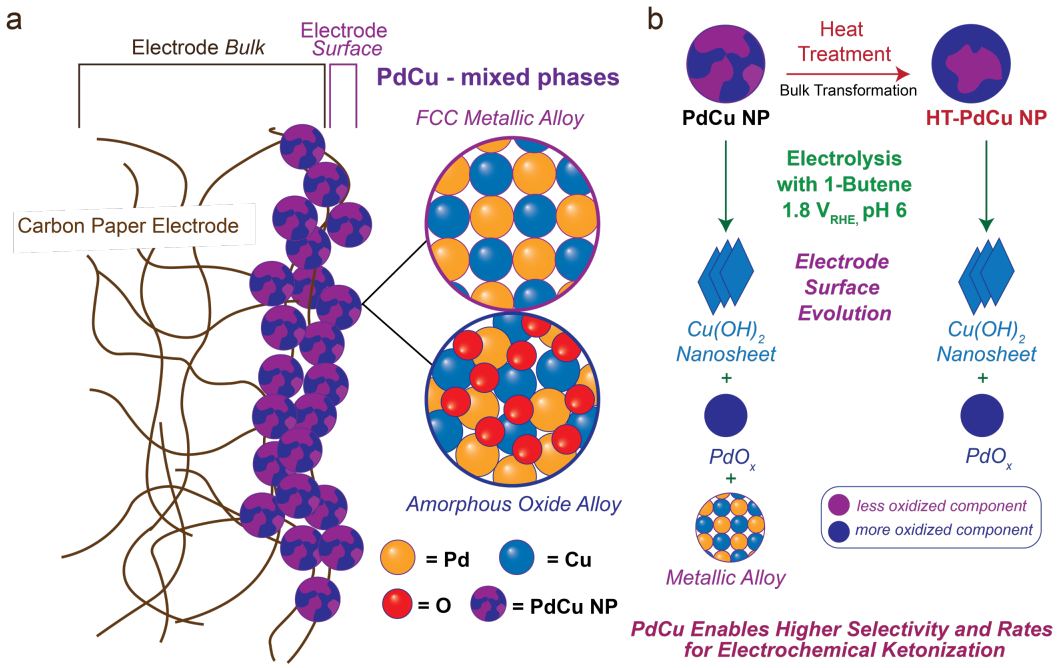

Figure 4.4: Schematics of catalyst-loaded electrode and surface evolution under operating conditions.

shows a potential-dependent epoxide-ketone selectivity based on the OER onset potential (Figure 4.2b and c). Below the OER onset potential, ketonization is favored, while epoxidation overtakes at higher potentials. The observed high ketone selectivity at lower potentials indicates that oxygen intermediates with mild oxidizing ability favor ketone formation. In addition to kinetic competition between oxygen intermediates, it is also plausible that more oxidizing potentials lead to the loss of the less oxidized sites, hence resulting in decreased ketone selectivity. Consequently, the catalyst-phase-dependent selectivity can be compounded by reaction kinetics. Applied potential modulates the electronic properties and thermodynamics of the catalyst surface species, altering the reactivity of oxygen intermediates and thereby affecting ketone-epoxide selectivity. Therefore, potential also plays a significant role in determining product selectivity. Ketone-epoxide selectivity can be influenced by both catalyst phase change and external potential, with potential-induced surface changes further complicating the factors governing selectivity.

Post-electrolysis characterization of catalyst-loaded electrodes provides insight into the potential-induced surface changes. Formation of $Cu(OH)_2$ was observed via XPS and SEM on the surfaces of PdCu- and HT-PdCu-loaded electrodes after electrolysis (Figure 4.3e and g). Considering the poor ketonization performance by

HT-PdCu, $Cu(OH)_2$ is unlikely to account for the superior performance of PdCu. Moreover, surface "Pd(IV)" species were detected on all three post-electrolysis electrode surfaces, suggesting oxidation of the surface Pd species under operating conditions (Figure 4.3d). Intriguingly, not all Pd species on the PdCu surface become more oxidized under anodic polarization. Although the surface Pd(II) species was observed as the dominant species in pristine PdCu, Pd(0) becomes the main component after electrolysis. Moreover, the surface Cu species in PdCu did not fully convert to Cu(II), even under the same electrochemical conditions that oxidize the majority of the Pd(0) in monometallic Pd. Uniform Pd and Cu elemental mapping on the post-electrolysis PdCu electrode indicates a high degree of Pd–Cu mixing within the nanoparticle structures (Figure C.22). These spectroscopic observations point to a metallic alloy component on the PdCu surface after electrolysis, in contrast to the predominantly oxidized surfaces of metallic Pd and HT-PdCu. The superior ketonization performance of PdCu thus may arise not only from its metallic surface species in the pristine state but also from its ability to retain the metallic phase under anodic polarization. This unusual resistance to surface oxidation is likely a result of the electronic effects of alloying Pd and Cu.

4.4 Conclusion

This chapter expands the scope of alkene electro-oxidation by reporting the heterogeneous ketonization of 1-butene to 2-butanone using a bimetallic PdCu electrocatalyst in aqueous electrolytes. While previous research has largely focused on propylene epoxidation, we present the first study of electro-oxidation of 1-butene, which is inherently more challenging due to poorer aqueous solubility and reactivity caused by the longer carbon chain. We demonstrated selective generation of 2-butanone for its industrial relevance and promising status as a fossil fuel alternative. We established the heterogeneous nature of the system and showed that the PdCu catalyst achieves a fourfold enhancement in product rate and a twofold improvement in Faradaic efficiency for 2-butanone compared to monometallic Pd and pre-oxidized controls. Notably, ketone-epoxide selectivity can be modulated by applied potential, with ketonization favored below the OER onset potential. Furthermore, 2-butanone generation exhibits a weak dependence on both applied potentials and bulk electrolyte pHs, suggesting that the reaction is likely limited by a thermochemical rather than an electrochemical step. Characterization of pristine and post-electrolysis electrodes revealed that alloying Pd and Cu generates a metallic phase that remains largely preserved under anodic polarization, in contrast to the monometallic Pd control and

the pre-oxidized analog. We propose that this metallic phase is responsible for the improved ketonization activity. Collectively, these findings indicate that the metallic PdCu phase drives the selective ketonization of 1-butene, offering a framework for the rational design of future alkene ketonization electrocatalysts.

4.5 Methods

Catalyst and Electrode Preparation

The bimetallic PdCu catalyst was synthesized via a co-reduction method that was adapted from a literature procedure.[150] Briefly, 0.25 mmol palladium(II) chloride (Thermo Scientific, 99%) and 0.25 mmol copper(II) chloride (Acros Organis, 99%) solutions were combined with 1.25 mmol of trimethyl(tetra-decyl)ammonium bromide (Sigma Aldrich, 99%) in 200 mL Milli-Q water. The solutions were cooled below 10 °C. 6 mmol of L-ascorbic acid (Sigma Aldrich, Reagent grade) was then added. The reaction mixture was kept cool and stirred rigorously overnight. The product was washed with abundant Milli-Q water and collected and dried at 60 °C overnight under vacuum. The catalyst powder, reddish brown in color, was collected and ground with a mortar and a pestle so that the catalyst powder had a consistent and fine texture. The powder was stored at room temperature. The pure Pd material was synthesized following the same procedure with 0.5 mmol of palladium(II) chloride and no addition of copper(II) chloride.

PdCu-loaded electrodes were prepared by drop casting catalyst ink solutions [5 mg of PdCu powder and 2 mg of carbon black (Vulcan XC 72, Fuel Cell Store) in 1 mL of water/IPA (1:4 w/w)] onto Sigracet carbon paper (Sigracet 39 BB, 5 wt.% PTFE, Fuel Cell Store). A total of 300 μL of catalyst ink was drop casted in 50 μL increments. Electrodes were then coated with 50 μL of 2 wt.% Nafion solution and dried at 80 °C overnight.

Electrolyte Preparation

Aqueous electrolyte solutions were used in the electrochemical studies. All electrolyte formulations used 0.9 M sodium perchlorate (Sigma Aldrich, 98%), and the bulk pH was controlled via the 0.25 M sodium phosphate buffer. The electrolytes were prepared from 5 M $NaClO_4$ and 1 M/0.5 M sodium phosphate stock solutions. The buffer solutions were prepared by dissolving the theoretically determined amount of phosphoric acid (Mallinckrodt 85%), sodium phosphate monobasic (Sigma Aldrich, 98%), sodium phosphate dibasic heptahydrate (Acros Organis, 99+%), and sodium phosphate (Sigma Aldrich, 96%) in Milli-Q water and adjusting

to the desired pH value with 1 M NaOH and 1 M H_3PO_4 solutions.

Electrochemical Reaction Setup and Product Quantification

Electrochemical experiments were performed in a sandwich-style electrochemical cell in a gas-diffusion configuration with a piece of platinum foil (Beantown Chemical, 99.99%) as the counter electrode and catalyst-loaded carbon paper as the working electrode. A leakless Ag/AgCl electrode (eDAQ) was used as a reference electrode. Aluminum foils (Reynold's Wrap) acted as the current collectors for both the anode and cathode. Hydrophobic carbon paper (Toray Carbon Paper 120, 5% wet-proofed, Fuel Cell Store) was placed behind the catalyst-loaded carbon paper to prevent electrolyte flooding. The total volume of electrolyte is 3.6 mL, and an ambient flow of 1-butene was introduced to the cell in a pass-through configuration during the bulk electrolysis.

The electrochemical measurements were conducted with a BioLogic VMP3 Multichannel potentiostat. The solution resistance was measured at open circuit potential (OCP) by electrochemical impedance spectroscopy techniques from 200 kHz to 100 mHz at 10 mV amplitude, and the resulting resistance determined from the x-intercept in the Nyquist plot was input for 100% iR compensation. The electrolysis experiments were conducted at fixed applied potentials for 30 min.

The post-electrolysis electrolytes were collected and dispensed into a 5 mL volumetric flask. The electrolyte chamber was rinsed with additional Milli-Q water, which was then transferred to the volumetric flask until the total volume reached the mark. 540 μL of the electrolyte was added to a clean NMR tube in addition to 60 μL of the internal standard solution, ~1mM 3-(Trimethylsilyl)-1-propanesulfonic acid sodium salt (Fluka Chemika, 99%) in D_2O. The products were quantified using ^1H-NMR spectroscopy. The NMR spectra were acquired on a Bruker 400 MHz spectrometer with water suppression performed. The ^1H probe was automatically tuned, and the solvent lock was done with 90% H_2O and 10% D_2O, and gradient shimming and auto-gain were used. 32 scans were collected per sample, and relaxation delay was set at 3 seconds.

Powder XRD analysis

The X-ray diffraction patterns of the synthesized catalysts were obtained using an X-ray powder diffractometer (Rigaku SmartLab) with Cu Ka radiation (λ =1.54056 Å). The diffraction patterns were collected from 10-90° 2θ at a step size of 0.01° and 5° per minute. Data were processed using HighScore software.

X-ray photoelectron spectroscopy

XPS measurements were collected using an AXIS Nova spectrometer by Analytical and analyzed with CasaXPS software. XPS samples were prepared by pressing the sample powders and standard materials into 3-mm diameter pellets. After electrolysis, the electrodes were rinsed with Milli-Q water and dried under vacuum in a vacuum desiccator. The samples were directly attached to the sample platen with the platen's clips. The carbon 1s spectrum was always acquired for all the measurements so that the adventitious carbon at 285 eV could be used to calibrate the charging effect.

X-ray absorption spectroscopy

All XAS measurements were collected with an easyXAFS300 spectrometer in transmission mode with X-ray operating at 40 kV and 25 mA. The standard materials and catalyst powders were diluted with sucrose to ca. 10% and 15-18%, respectively, and homogenized with a mortar pestle. The resulting mixture was pressed into a 3-mm diameter pellet and sealed with Kapton. The post-electrolysis spectra were obtained by pressing the spent catalyst-loaded carbon paper electrodes into a 3-mm diameter pellet to increase the volumetric concentration. Standard XAS Cu foil was used to calibrate the energy shift. The raw spectra were analyzed and processed via the ATHENA suite to obtain the normalized spectra. The linear combination fitting function in ATHENA was used to fit the spectra of the standard samples to those of the catalysts.

Scanning electron microscopy and high-resolution transmission electron microscopy

The morphologies of the pristine and post-electrolysis electrodes were collected with a ZEISS 15500VP field emission SEM equipped with an Oxford X-MAS SDD EDS system. Catalyst-loaded carbon paper electrodes and vacuum-dried post-electrolysis carbon paper were attached to the SEM holders with carbon tape; extra copper tape was used to ground the sample. A turbo carbon evaporator was used to coat the sample with a thin layer of carbon (< 10 nm). All TEM characterizations were performed using an FEI Titan 80–300 scanning transmission electron microscope operated at 300 kV equipped with a field-emission gun, Oxford X-MaxN 100TLE 100 mm^2 SDD x-ray spectrometer, and Gatan Ultrascan digital camera. A small amount of diluted PdCu catalyst ink was drop-casted on to the TEM grid. The post-electrolysis PdCu-loaded carbon paper was sonicated with a probe sonicator in IPA to extract the catalyst powder. The resulting homogeneous solution was drop-casted

on to the TEM grid. The sample-loaded TEM grids were allowed to air-dry.

Chapter 5

CONCLUSIONS AND OUTLOOK

5.1 Conclusions

The principal focus of this thesis is electrochemical oxygen-atom transfer (OAT) reactions for oxidative functionalization of alkenes using water as the oxygen atom source under ambient conditions. Central to this work, we establish and investigate the distinctive reaction pathways between alkene epoxidation and ketonization, with the broader aim of expanding the scope of heterogeneous alkene electro-oxidation as a sustainable synthetic alternative.

Chapter 2 establishes the mechanistic foundation of this selectivity by examining a substrate scope of alkenes using MnO_x nanoparticles as the catalyst in acetonitrile/water blended electrolytes. We interrogated the hypothesis that the intrinsic electronic character of the alkene, specifically its philicity, plays a significant role in the ketone/epoxide selectivity. Although the substrate scope remains preliminary in breadth, the results reveal an intriguing and potentially predictive correlation between theoretically computed alkene relative electrophilicity and the experimentally observed epoxidation/ketonization selectivity, suggesting that alkene philicity may serve as a useful descriptor for reaction outcome. Complementing the substrate-scope study, a comprehensive reactivity study of cyclopentene electro-oxidation demonstrated that ketonization is favored under low water content conditions. Strikingly, this selectivity trend coincides with a less oxidized catalyst surface, as directly evidenced by *operando* XAS measurements.

This insight that a lower degree of surface oxidation correlates with enhanced ketonization selectivity proved to be a unifying theme across the thesis. In Chapter 3, as-synthesized bimetallic Pd–Cu material was found to display better performance without thermal treatment to achieve the oxide phase, corroborating the selectivity trends observed in Chapter 2. Notably, *in situ* electrochemical pre-activation was observed to drastically improve the catalytic performance of PdCu/C, revealing that the as-synthesized material is not itself the active catalyst but undergoes a transformation under operating conditions. Subsequent optimization efforts led to an alternative PdCu catalyst prepared via a different synthetic procedure. The PdCu catalyst, without electrochemical conditioning, achieves comparable FE and

faster rate for 2-butanone, emphasizing the significance of the catalyst synthesis in electrocatalysis, even for catalysts of nominally identical composition.

Finally, Chapter 4 interrogates the structural origins of the superior activity of PdCu. Through comparative characterization of PdCu and its monometallic Pd and pre-oxidized analogues in both pristine and post-electrolysis forms, it was found that alloying Pd and Cu generates a metallic phase that is resistant to harsh oxidative conditions, in contrast to the controls. Consequently, we postulate that this metallic phase plays a key role in the selective ketonization of 1-butene, an underexplored organic transformation. The findings of this thesis establish a coherent mechanistic and catalytic framework for electrochemical alkene OAT reactions.

5.2 Outlook

Identifying active catalysts and reaction microenvironment

This work has led to the discovery of the PdCu electrocatalytic ketonization system and established the metallic character of the catalyst as a key in facilitating ketone selectivity. While a multitude of characterization techniques were employed, the measurements were conducted *ex situ*, without applied potential. As discussed in Chapter 1, the application of voltage creates a dynamic electrode-electrolyte interface and induces restructuring of the electrolyte components at the interface.[27,32,33] Thus, the catalyst exists in a fundamentally distinct microenvironment under operating conditions. While *ex situ* measurements provide valuable insights into the state of the electrocatalyst after electrolysis, they fail to capture the active catalyst as it interacts with its local environment during operation. Future studies should therefore prioritize *operando* spectroscopic investigations to directly monitor surface evolution and intermediate species under reaction conditions. Of particular importance is the direct spectroscopic characterization of the interfacial structure. Interfacial water structure, modulated by electrolyte ions and applied potential, has been demonstrated to be a governing factor in aqueous electrocatalysis.[36,37,53] Given that the reactivity of ROS is instrumental in determining the selectivity in addition to the observed dependence of Mn oxidation state on water content, resolving the optimal interfacial water structure for epoxidation and ketonization would reveal additional tunable parameters for designing more selective electrocatalytic systems.

Beyond Tafel and rate-law analyses

Tafel slope analysis based on Butler-Volmer equation remains the standard approach for evaluating electrocatalytic kinetics, yet its application is fundamentally limited.

Tafel analysis is strictly valid only at high overpotentials and grounded in outer-sphere electron transfer model.[186] In contrast, most electrocatalysis, like OER, proceeds via inner-sphere electron transfer, where electric double layer dictates the behavior of the solvent, ions, and reaction species at the electrocatalyst surface.[19] Critically, Tafel analysis accounts for the effects of the electric field on the activation enthalpy but overlooks entropic components. Both early works by Conway and more contemporary studies have illustrated the crucial role of the entropic contributions in electrocatalysis.[50–53,187] Temperature-dependent Arrhenius measurements can be used to extrapolate $\Delta H^{\ddagger}$ and $\Delta S^{\ddagger}$ of the activation, revealing entropic control in a certain kinetic regime. Moreover, potential-resolved Arrhenius analysis captures the dynamic evolution of the electrocatalyst surface and interface as a function of applied potential, providing more granular insights into transition states across the full potential range. Importantly, this approach is valid at low overpotential, overcoming the key limitation of Tafel analysis and enabling interrogation of the onset potentials required for alkene electro-oxidation. Therefore, potential-temperature dependent Arrhenius analysis should complement Tafel slope measurements to yield a more complete kinetic picture of alkene electro-oxidation.

Rate law analysis, extracted from reactant-dependent experiments, is another widely practiced kinetic tool in organic electrocatalysis. Steady-state microkinetic analysis is commonly employed to extrapolate rate-determining intermediate species, wherein a single elementary step (i.e., rate-determining step, RDS) is assumed to determine the overall reaction rate as the kinetic bottleneck. An analogous concept, potential-determining steps (PDS), has been specifically introduced for electrocatalytic reactions to describe the thermodynamic bottleneck.[188] However, the concept of the RDS has been debated in heterogeneous electrocatalysis. It assumes negligible surface coverage of adsorbed species, which is particularly tenuous in electrocatalysis,[189] where coverage-dependent rates and potential-dependent coverage are well-documented.[16,23,190–192] Furthermore, the presence of a PDS can masquerade as an RDS, particularly when the rate-order measurements are conducted at a single potential.

Alkene electro-oxidation involves multiple electrochemical and thermochemical steps, rendering its kinetics considerably more complex than better-studied reactions, such as OER or HER. To a first approximation, the electrochemical steps responsible for water activation and ROS generation can proceed via proton-electron coupled or separated pathways depending on the reaction conditions. The subsequent OAT

steps are generally considered to be thermochemical in nature. With peroxo-type oxidants, epoxide formation is thought to proceed in a concerted fashion to form the strained ring, whereas ketone formation requires H-atom shift. This mechanistic complexity means that macroscopic activity measurements alone are insufficient to draw conclusions about the underlying elementary steps. Kinetic analysis of alkene electro-oxidation should therefore be grounded in well-characterized systems with an accurate understanding of the surface speciation under operating conditions, ideally informed by the *operando* spectroscopic approaches described above.

BIBLIOGRAPHY

(1) Jiang, C.; Moss, B.; Lindenfelser, A.; Kim, J. T.; Li, Y.; Manthiram, K. Metallic Pd–Cu Alloy Phases Drive Selective Heterogeneous Electrochemical Ketonization of 1-Butene. *ACS Catalysis* **2026**, *16*, 7429–7438, DOI: 10.1021/acscatal.5c08675.

(2) Zeng, J. S.; Cosner, E. L.; Delgado-Kukuczka, S. P.; Jiang, C.; Adams, J. S.; Román-Leshkov, Y.; Manthiram, K. Electrifying Hydroformylation Catalysts Exposes Voltage-Driven C–C Bond Formation. *Journal of the American Chemical Society* **2024**, *146*, 16521–16530, DOI: 10.1021/jacs.4c02992.

(3) Chung, M.; Maalouf, J. H.; Adams, J. S.; Jiang, C.; Román-Leshkov, Y.; Manthiram, K. Direct propylene epoxidation via water activation over Pd-Pt electrocatalysts. *Science* **2024**, *383*, 49–55, DOI: 10.1126/science.adh4355.

(4) Koner, K.; Adams, J. S.; Miu, E. V.; Delgado-Kukuczka, S. P.; Jiang, C.; Kim, J. T.; Park, H.; Bui, J. C.; Oyala, P. H.; Li, Y.; Manthiram, K. Direct electrochemical propylene epoxidation over amorphized perovskite oxide in non-halogenated aqueous electrolyte. *Nature Catalysis* **2026**, 1–10, DOI: 10.1038/s41929-026-01535-6.

(5) Adams, J. S.; Koner, K.; Moss, B.; Bui, J. C.; Jiang, C.; Cosner, E. L.; Park, Y.; Chung, M.; Kim, J. T.; Park, H.; Li, Y.; Manthiram, K. Structure of PdPtOx and Kinetic Analysis of Electrochemical Propylene Epoxidation. *Angewandte Chemie International Edition* **2026**, *Manuscript submitted.*

(6) Cavaliere, P., Fundamentals of Water Electrolysis In *Water Electrolysis for Hydrogen Production*, Cavaliere, P., Ed.; Springer International Publishing: Cham, 2023, pp 1–60, DOI: 10.1007/978-3-031-37780-8_1.

(7) Smolinka, T.; Bergmann, H.; Garche, J.; Kusnezoff, M., The history of water electrolysis from its beginnings to the present In *Electrochemical Power Sources: Fundamentals, Systems, and Applications*; Elsevier: 2022, pp 83–164, DOI: 10.1016/B978-0-12-819424-9.00010-0.

(8) Duca, M.; Koper, M. T., Fundamental Aspects of Electrocatalysis In *Surface and Interface Science*, Section: 59 _eprint: https://onlinelibrary.wiley.com/doi/pdf/10.1002/978352
John Wiley & Sons, Ltd: 2020, pp 773–890, DOI: 10.1002/9783527680603.ch59.

(9) Liu, R.-T.; Xu, Z.-L.; Li, F.-M.; Chen, F.-Y.; Yu, J.-Y.; Yan, Y.; Chen, Y.; Xia, B. Y. Recent Advances in Proton Exchange Membrane Water Electrolysis. *Chemical Society Reviews* **2023**, *52*, 5652–5683, DOI: 10.1039/D2CS00681B.

(10) Dubouis, N.; Aymé-Perrot, D.; Degoulange, D.; Grimaud, A.; Girault, H. Alkaline Electrolyzers: Powering Industries and Overcoming Fundamental Challenges. *Joule* **2024**, *8*, 883–898, DOI: 10.1016/j.joule.2024.02.012.

(11) US EPA, O. GHG Emission Factors Hub, en, Overviews and Factsheets, 2015.

(12) Centi, G.; Perathoner, S. Electrocatalysis: Prospects and Role to Enable an E-Chemistry Future. *The Chemical Record* **2025**, *25*, e202400259, DOI: 10.1002/tcr.202400259.

(13) Schiffer, Z. J.; Manthiram, K. Electrification and Decarbonization of the Chemical Industry. *Joule* **2017**, *1*, 10–14, DOI: 10.1016/j.joule.2017.07.008.

(14) Schiffer, Z. J.; Limaye, A. M.; Manthiram, K. Thermodynamic Discrimination between Energy Sources for Chemical Reactions. *Joule* **2021**, *5*, 135–148, DOI: 10.1016/j.joule.2020.12.014.

(15) Fabbri, E.; Schmidt, T. J. Oxygen Evolution Reaction—The Enigma in Water Electrolysis. *ACS Catalysis* **2018**, *8*, 9765–9774, DOI: 10.1021/acscatal.8b02712.

(16) Nong, H. N. et al. Key Role of Chemistry Versus Bias in Electrocatalytic Oxygen Evolution. *Nature* **2020**, *587*, Number: 7834, 408–413, DOI: 10.1038/s41586-020-2908-2.

(17) Park, W.; Chung, D. Y. Activity–Stability Relationships in Oxygen Evolution Reaction. *ACS Materials Au* **2025**, *5*, 1–10, DOI: 10.1021/acsmaterialsau.4c00086.

(18) Santos, E.; Nazmutdinov, R.; Schmickler, W. Electron Transfer at Different Electrode Materials: Metals, Semiconductors, and Graphene. *Current Opinion in Electrochemistry* **2020**, *19*, 106–112, DOI: 10.1016/j.coelec.2019.11.003.

(19) Bard, A. J. Inner-Sphere Heterogeneous Electrode Reactions. Electrocatalysis and Photocatalysis: The Challenge. *Journal of the American Chemical Society* **2010**, *132*, 7559–7567, DOI: 10.1021/ja101578m.

(20) Yazdani, A.; Botte, G. G. Perspectives of Electrocatalysis in the Chemical Industry: A Platform for Energy Storage. *Current Opinion in Chemical Engineering* **2020**, *29*, 89–95, DOI: 10.1016/j.coche.2020.07.003.

(21) Fuller, T. F.; Harb, J. N., *Electrochemical engineering*; John Wiley & Sons: 2018.

(22) Roduner, E. Selected Fundamentals of Catalysis and Electrocatalysis in Energy Conversion Reactions—a Tutorial. *Catalysis Today* **2018**, *309*, 263–268, DOI: 10.1016/j.cattod.2017.05.091.

(23) Shinagawa, T.; Garcia-Esparza, A. T.; Takanabe, K. Insight on Tafel slopes from a microkinetic analysis of aqueous electrocatalysis for energy conversion. *Scientific Reports* **2015**, *5*, Number: 1, 13801, DOI: 10.1038/srep13801.

(24) Schmickler, W.; Santos, E., Phenomenological treatment of electron-transfer reactions In *Interfacial Electrochemistry*, Schmickler, W., Santos, E., Eds.; Springer: Berlin, Heidelberg, 2010, pp 91–98, DOI: 10.1007/978-3-642-04937-8_9.

(25) Wu, J. Understanding the Electric Double-Layer Structure, Capacitance, and Charging Dynamics. *Chemical Reviews* **2022**, *122*, 10821–10859, DOI: 10.1021/acs.chemrev.2c00097.

(26) Schmickler, W.; Santos, E., The metal-solution interface In *Interfacial Electrochemistry*, Schmickler, W., Santos, E., Eds.; Springer: Berlin, Heidelberg, 2010, pp 39–50, DOI: 10.1007/978-3-642-04937-8_5.

(27) Cheng, Q.; Wang, M.; Ni, J.; Zhang, L.; Cheng, Y.; Zhou, X.; Cao, Y.; Qian, T.; Yan, C. Comprehensive Understanding and Rational Regulation of Microenvironment for Gas-Involving Electrochemical Reactions. *Carbon Energy* **2023**, *5*, e307, DOI: 10.1002/cey2.307.

(28) Li, G.-F.; Divinagracia, M.; Labata, M. F.; Ocon, J. D.; Abel Chuang, P.-Y. Electrolyte-Dependent Oxygen Evolution Reactions in Alkaline Media: Electrical Double Layer and Interfacial Interactions. *ACS Applied Materials & Interfaces* **2019**, *11*, 33748–33758, DOI: 10.1021/acsami.9b06889.

(29) Lucky, C.; Schreier, M. Mind the Interface: The Role of Adsorption in Electrocatalysis. *ACS Nano* **2024**, *18*, 6008–6015, DOI: 10.1021/acsnano.3c09523.

(30) Tang, Z.; Dong, Z.; Yuan, L.; Li, B.; Zhu, Y. Unlocking the Potential: Key Roles of Interfacial Water in Electrocatalysis. *EES Catalysis* **2025**, *3*, 943–971, DOI: 10.1039/D5EY00161G.

(31) Deng, B.; Huang, M.; Zhao, X.; Mou, S.; Dong, F. Interfacial Electrolyte Effects on Electrocatalytic CO_2 Reduction. *ACS Catalysis* **2022**, *12*, 331–362, DOI: 10.1021/acscatal.1c03501.

(32) Ye, W.; Yang, W. A Holistic View of Ions and Water Arrangements at the Electrified Cu Surface during Electrochemical CO2 Conversion. *The Journal of Physical Chemistry C* **2026**, *130*, 827–837, DOI: 10.1021/acs.jpcc.5c07614.

(33) Noh, J.; Kim, H.; Park, H.; Chung, D. Y. The Roles of Ions in Electrochemical Interface for Electrocatalysis. *ACS Catalysis* **2025**, *15*, 7780–7791, DOI: 10.1021/acscatal.5c00700.

(34) Liu, Z.; Ma, G.; Zhu, X.; Shen, Y.; Guo, X.; Ding, Y.; Liu, J.; Khalafallah, D.; Huang, X.; Guo, B.; Li, S. Anion Effect in Electrocatalysts for Oxygen Evolution Reaction and Small Organic Molecule Oxidation. *ACS Energy Letters* **2026**, *11*, 1514–1537, DOI: 10.1021/acsenergylett.5c04078.

(35) Wu, Q.; Xu, Z. J. Mechanistic Insights into Cation Effects in Electrolytes for Electrocatalysis. *Angewandte Chemie International Edition* **2025**, *64*, e202505022, DOI: 10.1002/anie.202505022.

(36) Rao, R. R.; Huang, B.; Katayama, Y.; Hwang, J.; Kawaguchi, T.; Lunger, J. R.; Peng, J.; Zhang, Y.; Morinaga, A.; Zhou, H.; You, H.; Shao-Horn, Y. pH- and Cation-Dependent Water Oxidation on Rutile RuO2(110). *The Journal of Physical Chemistry C* **2021**, *125*, 8195–8207, DOI: 10.1021/acs.jpcc.1c00413.

(37) Liang, C.; Katayama, Y.; Tao, Y.; Morinaga, A.; Moss, B.; Celorrio, V.; Ryan, M.; Stephens, I. E. L.; Durrant, J. R.; Rao, R. R. Role of Electrolyte pH on Water Oxidation for Iridium Oxides. *Journal of the American Chemical Society* **2024**, *146*, 8928–8938, DOI: 10.1021/jacs.3c12011.

(38) Huang, B. et al. Cation- and pH-Dependent Hydrogen Evolution and Oxidation Reaction Kinetics. *JACS Au* **2021**, *1*, 1674–1687, DOI: 10.1021/jacsau.1c00281.

(39) Yue, Y.; Zhong, X.; Sun, M.; Du, J.; Gao, W.; Hu, W.; Zhao, C.; Li, J.; Huang, B.; Li, Z.; Li, C. Fluorine Engineering Induces Phase Transformation in NiCo2O4 for Enhanced Active Motifs Formation in Oxygen Evolution Reaction. *Advanced Materials* **2025**, *37*, 2418058, DOI: 10.1002/adma.202418058.

(40) Jiang, H.; He, Q.; Li, X.; Su, X.; Zhang, Y.; Chen, S.; Zhang, S.; Zhang, G.; Jiang, J.; Luo, Y.; Ajayan, P. M.; Song, L. Tracking Structural Self-Reconstruction and Identifying True Active Sites toward Cobalt Oxychloride Precatalyst of Oxygen Evolution Reaction. *Advanced Materials* **2019**, *31*, 1805127, DOI: 10.1002/adma.201805127.

(41) Zhang, X.; Wang, Z.; Liu, S.; Lu, M.; Wang, Y.; Luo, B.; Shen, T.; Ren, Z.; Chen, Z.; Liu, B. Leaching-Reconstruction Engineering of Anions on Ferronickel Phosphate Promotes the Enhancement of the Oxygen Evolution Reaction. *ACS Applied Materials & Interfaces* **2025**, *17*, 13851–13860, DOI: 10.1021/acsami.4c19888.

(42) Guan, D. et al. Utilizing Ion Leaching Effects for Achieving High Oxygen-Evolving Performance on Hybrid Nanocomposite with Self-Optimized Behaviors. *Nature Communications* **2020**, *11*, 3376, DOI: 10.1038/s41467-020-17108-5.

(43) Hausmann, J. N.; Menezes, P. W. Effect of Surface-Adsorbed and Intercalated (Oxy)anions on the Oxygen Evolution Reaction. *Angewandte*

Chemie International Edition **2022**, *61*, e202207279, DOI: 10.1002/anie.202207279.

(44) Han, X.; Chen, S.; Yu, J.; Wang, S. Activation of the Lattice Oxygen Mechanism in NiOOH as an Electrocatalyst for the Oxygen Evolution Reaction: The Role of Anion Intercalation. *ACS Applied Materials & Interfaces* **2025**, *17*, 54181–54189, DOI: 10.1021/acsami.5c10726.

(45) Yang, C.; Fontaine, O.; Tarascon, J.-M.; Grimaud, A. Chemical Recognition of Active Oxygen Species on the Surface of Oxygen Evolution Reaction Electrocatalysts. *Angewandte Chemie International Edition* **2017**, *56*, 8652–8656, DOI: 10.1002/anie.201701984.

(46) Garcia, A. C.; Touzalin, T.; Nieuwland, C.; Perini, N.; Koper, M. T. M. Enhancement of Oxygen Evolution Activity of Nickel Oxyhydroxide by Electrolyte Alkali Cations. *Angewandte Chemie International Edition* **2019**, *58*, 12999–13003, DOI: 10.1002/anie.201905501.

(47) Strmcnik, D.; Kodama, K.; van der Vliet, D.; Greeley, J.; Stamenkovic, V. R.; Marković, N. M. The Role of Non-Covalent Interactions in Electrocatalytic Fuel-Cell Reactions on Platinum. *Nature Chemistry* **2009**, *1*, 466–472, DOI: 10.1038/nchem.330.

(48) Huang, J.; Li, M.; Eslamibidgoli, M. J.; Eikerling, M.; Groß, A. Cation Overcrowding Effect on the Oxygen Evolution Reaction. *JACS Au* **2021**, *1*, 1752–1765, DOI: 10.1021/jacsau.1c00315.

(49) Zhang, G.; Schreier, M. Leveraging Electrochemical Double Layer Structure to Rationally Control Electrolysis. *National Science Review* **2024**, *11*, nwae299, DOI: 10.1093/nsr/nwae299.

(50) Conway, B. E.; Tessier, D. F.; Wilkinson, D. P. Experimental Evidence for the Potential-dependence of entropy of activation in electrochemical reactions in relation to the temperature-dependence of Tafel Slopes. *Journal of Electroanalytical Chemistry* **1986**, *199*, 249–246.

(51) Martínez-Hincapié, R.; Timoshenko, J.; Wagner, T.; Ortega, E.; Druce, J.; Monteiro, M. C. O.; Rüscher, M.; Jang, J.; Alagöz, E. Ö.; Lasagna, S.; Jacobse, L.; Bergmann, A.; Cuenya, B. R.; Oener, S. Z. Interfacial Solvation Pre-Organizes the Transition State of the Oxygen Evolution Reaction. *Nature Chemistry* **2025**, 1–9, DOI: 10.1038/s41557-025-01932-7.

(52) Sarabia, F.; Gomez Rodellar, C.; Roldan Cuenya, B.; Oener, S. Z. Exploring Dynamic Solvation Kinetics at Electrocatalyst Surfaces. *Nature Communications* **2024**, *15*, 8204, DOI: 10.1038/s41467-024-52499-9.

(53) Zhang, H.; Raciti, D.; Hall, A. S. Disordered Interfacial H2O Promotes Electrochemical C–C Coupling. *Nature Chemistry* **2025**, *17*, 1161–1168, DOI: 10.1038/s41557-025-01859-z.

(54) Noh, S.; Cho, Y. J.; Zhang, G.; Schreier, M. Insight into the Role of Entropy in Promoting Electrochemical CO2 Reduction by Imidazolium Cations. *Journal of the American Chemical Society* **2023**, *145*, 27657–27663, DOI: 10.1021/jacs.3c09687.

(55) Sabatier, P. Hydrogénations et déshydrogénations par catalyse. *Berichte der deutschen chemischen Gesellschaft* **1911**, *44*, 1984–2001, DOI: 10.1002/cber.19110440303.

(56) Ooka, H.; Huang, J.; Exner, K. S. The Sabatier Principle in Electrocatalysis: Basics, Limitations, and Extensions. *Frontiers in Energy Research* **2021**, *9*, DOI: 10.3389/fenrg.2021.654460.

(57) Hammer, B.; Norskov, J. K. Why Gold Is the Noblest of All the Metals. *Nature* **1995**, *376*, 238–240, DOI: 10.1038/376238a0.

(58) Hammer, B.; Morikawa, Y.; Nørskov, J. K. CO Chemisorption at Metal Surfaces and Overlayers. *Physical Review Letters* **1996**, *76*, 2141–2144, DOI: 10.1103/PhysRevLett.76.2141.

(59) Ruban, A.; Hammer, B.; Stoltze, P.; Skriver, H.; Nørskov, J. Surface Electronic Structure and Reactivity of Transition and Noble metals. *Journal of Molecular Catalysis A: Chemical* **1997**, *115*, 421–429, DOI: 10.1016/S1381-1169(96)00348-2.

(60) Christoffersen, E.; Liu, P.; Ruban, A.; Skriver, H.; Nørskov, J. Anode Materials for Low-Temperature Fuel Cells: A Density Functional Theory Study. *Journal of Catalysis* **2001**, *199*, 123–131, DOI: 10.1006/jcat.2000.3136.

(61) Gorzkowski, M. T.; Lewera, A. Probing the Limits of d-Band Center Theory: Electronic and Electrocatalytic Properties of Pd-Shell–Pt-Core Nanoparticles. *The Journal of Physical Chemistry C* **2015**, *119*, 18389–18395, DOI: 10.1021/acs.jpcc.5b05302.

(62) Zhang, J.; Yang, H. B.; Zhou, D.; Liu, B. Adsorption Energy in Oxygen Electrocatalysis. *Chemical Reviews* **2022**, *122*, 17028–17072, DOI: 10.1021/acs.chemrev.1c01003.

(63) Nørskov, J. K.; Abild-Pedersen, F.; Studt, F.; Bligaard, T. Density Functional Theory in Surface Chemistry and Catalysis. *Proceedings of the National Academy of Sciences* **2011**, *108*, 937–943, DOI: 10.1073/pnas.1006652108.

(64) Saini, S.; Halldin Stenlid, J.; Abild-Pedersen, F. Electronic Structure Factors and the Importance of Adsorbate Effects in Chemisorption on Surface Alloys. *npj Computational Materials* **2022**, *8*, 163, DOI: 10.1038/s41524-022-00846-z.

(65) Seh, Z. W.; Kibsgaard, J.; Dickens, C. F.; Chorkendorff, I.; Nørskov, J. K. Combining Theory and Experiment in Electrocatalysis: Insights into Materials Design. *Science* **2017**, *355*, eaad4998, DOI: 10.1126/science.aad49.

(66) Exner, K. S. Four Generations of Volcano Plots for the Oxygen Evolution Reaction: Beyond Proton-Coupled Electron Transfer Steps? *Accounts of Chemical Research* **2024**, *57*, 1336–1345, DOI: 10.1021/acs.accounts.4c00048.

(67) Zielinski, A. J.; Lucky, C.; Schreier, M. Linking Electrocatalytic Turnover to Elementary Step Rates in Hydrocarbon Fuel Oxidation. *Nature Communications* **2025**, *16*, 9100, DOI: 10.1038/s41467-025-63910-4.

(68) Zhang, G.; Fuller, L.; Lucky, C.; Zielinski, A. J.; Cheng, D.; Mendoza, E.; Sautet, P.; Schreier, M. Room-Temperature Electrocatalytic Dehydrogenation and Partial Fragmentation of n-Alkanes. *Journal of the American Chemical Society* **2025**, *147*, 35219–35226, DOI: 10.1021/jacs.5c12806.

(69) Bakshi, H. B.; Lucky, C.; Chen, H.-S.; Schreier, M. Electrocatalytic Scission of Unactivated C(sp3)–C(sp3) Bonds through Real-Time Manipulation of Surface-Bound Intermediates. *Journal of the American Chemical Society* **2023**, *145*, 13742–13749, DOI: 10.1021/jacs.3c02108.

(70) Liang, C.; Rao, R. R.; Svane, K. L.; Hadden, J. H. L.; Moss, B.; Scott, S. B.; Sachs, M.; Murawski, J.; Frandsen, A. M.; Riley, D. J.; Ryan, M. P.; Rossmeisl, J.; Durrant, J. R.; Stephens, I. E. L. Unravelling the Effects of Active Site Density and Energetics on the Water Oxidation Activity of Iridium Oxides. *Nature Catalysis* **2024**, *7*, 763–775, DOI: 10.1038/s41929-024-01168-7.

(71) Moss, B.; Liang, C.; Carpenter, A.; Verga, L. G.; Scott, S.; Jones, R. J. R.; Manthiram, K.; Walsh, A.; Rao, R. R.; Stephens, I. E. L.; Durrant, J. R. Operando Ultraviolet–Visible Optical Spectroelectrochemistry of Surfaces. *Nature Reviews Methods Primers* **2025**, *5*, 73, DOI: 10.1038/s43586-025-00445-4.

(72) Linnemann, J.; Kanokkanchana, K.; Tschulik, K. Design Strategies for Electrocatalysts from an Electrochemist's Perspective. *ACS Catalysis* **2021**, *11*, 5318–5346, DOI: 10.1021/acscatal.0c04118.

(73) Li, G.-F.; Yang, D.; Abel Chuang, P.-Y. Defining Nafion Ionomer Roles for Enhancing Alkaline Oxygen Evolution Electrocatalysis. *ACS Catalysis* **2018**, *8*, 11688–11698, DOI: 10.1021/acscatal.8b02217.

(74) Cerrón-Calle, G. A.; Senftle, T. P.; Garcia-Segura, S. Strategic Tailored Design of Electrocatalysts for Environmental Remediation Based on Density Functional Theory (DFT) and Microkinetic Modeling. *Current Opinion in Electrochemistry* **2022**, *35*, 101062, DOI: 10.1016/j.coelec.2022.101062.

(75) Zhang, Y.; Xiong, Y.; Wang, Y.; Wang, Q.; Fan, J. Advances in Computational Approaches for Bridging Theory and Experiments in Electrocatalyst Design. *Nanoscale Horizons* **2025**, *10*, 2211–2238, DOI: 10.1039/D5NH00216H.

(76) Li, H.; Abraham, C. S.; Anand, M.; Cao, A.; Nørskov, J. K. Opportunities and Challenges in Electrolytic Propylene Epoxidation. *The Journal of Physical Chemistry Letters* **2022**, *13*, 2057–2063, DOI: 10.1021/acs.jpclett.2c00257.

(77) Basera, P.; Mandal, S. C.; Abild-Pedersen, F.; Bajdich, M. Crossing the Oxo-Peroxo Wall for Selective Electrochemical Epoxidation. *Advanced Science* **2026**, *13*, e17229, DOI: 10.1002/advs.202517229.

(78) Silvioli, L.; Winiwarter, A.; Scott, S. B.; Castelli, I. E.; Moses, P. G.; Chorkendorff, I.; Seger, B.; Rossmeisl, J. Rational Catalyst Design for Higher Propene Partial Electro-oxidation Activity by Alloying Pd with Au. *The Journal of Physical Chemistry C* **2022**, *126*, 14487–14499, DOI: 10.1021/acs.jpcc.1c10095.

(79) Sinfelt, J. H. Catalysis by Alloys and Bimetallic Clusters. *Accounts of Chemical Research* **1977**, *10*, 15–20, DOI: 10.1021/ar50109a003.

(80) Liu, L.; Corma, A. Bimetallic Sites for Catalysis: From Binuclear Metal Sites to Bimetallic Nanoclusters and Nanoparticles. *Chemical Reviews* **2023**, *123*, 4855–4933, DOI: 10.1021/acs.chemrev.2c00733.

(81) Rossmeisl, J.; Ferrin, P.; Tritsaris, G. A.; Nilekar, A. U.; Koh, S.; Bae, S. E.; Brankovic, S. R.; Strasser, P.; Mavrikakis, M. Bifunctional Anode Catalysts for Direct Methanol Fuel Cells. *Energy & Environmental Science* **2012**, *5*, 8335–8342, DOI: 10.1039/C2EE21455E.

(82) Whittaker, T. N.; Hollis, E. N.; Oberg, H. J.; Paul, J. D.; Holewinski, A. Platinum–Ruthenium Alloys Are Not Bifunctional CO Electro-Oxidation Catalysts: A Kinetic Analysis. *ACS Energy Letters* **2026**, *11*, 664–672, DOI: 10.1021/acsenergylett.5c03371.

(83) Liang, H.-P.; Jones, T. G. J.; Lawrence, N. S.; Jiang, L.; Barnard, J. S. Understanding the Role of Nanoparticle Synthesis on Their Underlying Electrocatalytic Activity. *The Journal of Physical Chemistry C* **2008**, *112*, 4327–4332, DOI: 10.1021/jp7100804.

(84) Tang, Y.; Cheng, W. Nanoparticle-Modified Electrode with Size- and Shape-Dependent Electrocatalytic Activities. *Langmuir* **2013**, *29*, 3125–3132, DOI: 10.1021/la304616k.

(85) Müllner, M.; Riva, M.; Kraushofer, F.; Schmid, M.; Parkinson, G. S.; Mertens, S. F. L.; Diebold, U. Stability and Catalytic Performance of Reconstructed Fe3O4(001) and Fe3O4(110) Surfaces during Oxygen Evolution Reaction. *The Journal of Physical Chemistry C* **2019**, *123*, 8304–8311, DOI: 10.1021/acs.jpcc.8b08733.

(86) Poulain, R.; Klein, A.; Proost, J. Electrocatalytic Properties of (100)-, (110)-, and (111)-Oriented NiO Thin Films toward the Oxygen Evolution Reaction. *The Journal of Physical Chemistry C* **2018**, *122*, 22252–22263, DOI: 10.1021/acs.jpcc.8b05790.

(87) Füngerlings, A.; Wohlgemuth, M.; Antipin, D.; van der Minne, E.; Kiens, E. M.; Villalobos, J.; Risch, M.; Gunkel, F.; Pentcheva, R.; Baeumer, C. Crystal-Facet-Dependent Surface Transformation Dictates the Oxygen Evolution Reaction Activity in Lanthanum Nickelate. *Nature Communications* **2023**, *14*, 8284, DOI: 10.1038/s41467-023-43901-z.

(88) Davis, E. M.; Bergmann, A.; Kuhlenbeck, H.; Roldan Cuenya, B. Facet Dependence of the Oxygen Evolution Reaction on Co3O4, CoFe2O4, and Fe3O4 Epitaxial Film Electrocatalysts. *Journal of the American Chemical Society* **2024**, *146*, 13770–13782, DOI: 10.1021/jacs.3c13595.

(89) Ke, J.; Zhao, J.; Chi, M.; Wang, M.; Kong, X.; Chang, Q.; Zhou, W.; Long, C.; Zeng, J.; Geng, Z. Facet-Dependent Electrooxidation of Propylene into Propylene Oxide Over Ag3PO4 Crystals. *Nature Communications* **2022**, *13*, 932, DOI: 10.1038/s41467-022-28516-0.

(90) Wang, D.; Li, Y. Bimetallic Nanocrystals: Liquid-Phase Synthesis and Catalytic Applications. *Advanced Materials* **2011**, *23*, 1044–1060, DOI: 10.1002/adma.201003695.

(91) Shaddad, M. N.; Al-Mayouf, A. M.; Ghanem, M. A.; AlHoshan, M. S.; Singh, J. P.; Al-Suhybani, A. A. Chemical Deposition and Electrocatalytic Activity of Platinum Nanoparticles Supported on TiO2 Nanotubes. *International Journal of Electrochemical Science* **2013**, *8*, 2468–2478, DOI: 10.1016/S1452-3981(23)14324-0.

(92) Hausmann, J. N. et al. Reproducibility in Electrocatalysis. *ChemRxiv* **2025**, DOI: 10.26434/chemrxiv-2025-p0923.

(93) Baer, H.; Bergamo, M.; Forlin, A.; Pottenger, L. H.; Lindner, J., Propylene Oxide In *Ullmann's Encyclopedia of Industrial Chemistry*; John Wiley & Sons, Ltd: 2012, DOI: 10.1002/14356007.a22_239.pub3.

(94) Sienel, G.; Rieth, R.; Rowbottom, K. T., Epoxides In *Ullmann's Encyclopedia of Industrial Chemistry*; John Wiley & Sons, Ltd: 2000, DOI: 10.1002/14356007.a09_531.

(95) Siegel, H.; Eggersdorfer, M., Ketones In *Ullmann's Encyclopedia of Industrial Chemistry*; John Wiley & Sons, Ltd: 2000, DOI: 10.1002/14356007.a15_077.

(96) Dryuk, V. G. The Mechanism of Epoxidation of Olefins by Peracids. *Tetrahedron* **1976**, *32*, 2855–2866, DOI: 10.1016/0040-4020(76)80137-8.

(97) Kim, C.; Traylor, T. G.; Perrin, C. L. MCPBA Epoxidation of Alkenes: Reinvestigation of Correlation between Rate and Ionization Potential. *Journal of the American Chemical Society* **1998**, *120*, 9513–9516, DOI: 10.1021/ja981531e.

(98) Tsuji, J. Synthetic Applications of the Palladium-Catalyzed Oxidation of Olefins to Ketones. *Synthesis* **1984**, *5*, 369–384, DOI: 10.1055/s-1984-30848.

(99) Keith, J. A.; Nielsen, R. J.; Oxgaard, J.; Goddard, W. A. Unraveling the Wacker Oxidation Mechanisms. *Journal of the American Chemical Society* **2007**, *129*, 12342–12343, DOI: 10.1021/ja072400t.

(100) Keith, J. A.; Henry, P. M. The Mechanism of the Wacker Reaction: A Tale of Two Hydroxypalladations. *Angewandte Chemie International Edition* **2009**, *48*, 9038–9049, DOI: 10.1002/anie.200902194.

(101) Imbao, J.; Bokhoven, J. A. v.; Nachtegaal, M. Optimization of a Heterogeneous Pd–Cu/Zeolite Y Wacker Catalyst for Ethylene Oxidation. *Chemical Communications* **2020**, *56*, 1377–1380, DOI: 10.1039/C9CC08835K.

(102) Espeel, P. H.; Tielen, M. C.; Jacobs, P. A. Palladium–copper-exchanged Y type zeolites: a true heterogeneous Wacker catalyst. *J. Chem. Soc., Chem. Commun.* **1991**, *49*, 669–671, DOI: 10.1039/C39910000669.

(103) Rajeshwaran, P.; Trouvé, J.; Youssef, K.; Gramage-Doria, R. Sustainable Wacker-Type Oxidations. *Angewandte Chemie International Edition* **2022**, *61*, e202211016, DOI: 10.1002/anie.202211016.

(104) Sun, Y.; Hu, H.; Li, Y. Electro-Oxidation of Alkenes: A Green Approach Towards Functionalized Oxygenates. *ChemCatChem* **2024**, *16*, e202301534, DOI: 10.1002/cctc.202301534.

(105) Ghosh, R.; Hopping, G. M.; Lu, J. W.; Hollyfield, D. W.; Flaherty, D. W. Alkene Epoxidation and Oxygen Evolution Reactions Compete for Reactive Surface Oxygen Atoms on Gold Anodes. *Journal of the American Chemical Society* **2025**, *147*, 1482–1496, DOI: 10.1021/jacs.4c08948.

(106) Jin, K.; Maalouf, J. H.; Lazouski, N.; Corbin, N.; Yang, D.; Manthiram, K. Epoxidation of Cyclooctene Using Water as the Oxygen Atom Source at Manganese Oxide Electrocatalysts. *Journal of the American Chemical Society* **2019**, *141*, 6413–6418, DOI: 10.1021/jacs.9b02345.

(107) Chung, M.; Jin, K.; Zeng, J. S.; Ton, T. N.; Manthiram, K. Tuning Single-Atom Dopants on Manganese Oxide for Selective Electrocatalytic Cyclooctene Epoxidation. *Journal of the American Chemical Society* **2022**, *144*, 17416–17422, DOI: 10.1021/jacs.2c04711.

(108) Koroidov, S.; Winiwarter, A.; Diaz-Morales, O.; Görlin, M.; Halldin Stenlid, J.; Wang, H.-Y.; Börner, M.; Goodwin, C. M.; Soldemo, M.; Pettersson, L. G. M.; Rossmeisl, J.; Hansson, T.; Chorkendorff, I.; Nilsson, A. Chemisorbed Oxygen or Surface Oxides Steer the Selectivity in Pd Electrocatalytic Propene Oxidation Observed by *Operando* Pd L-Edge X-Ray Absorption Spectroscopy. *Catalysis Science & Technology* **2021**, *11*, 3347–3352, DOI: 10.1039/D0CY02134B.

(109) Li, D.; Sun, P.; Zhang, D.; Li, H.; Xu, H.; Cao, D. Unraveling the Potential-Dependent Selectivity of Propylene Electrooxidation: The Role of Electrochemistry-Induced Reconstruction. *Journal of the American Chemical Society* **2025**, *147*, 24900–24912, DOI: 10.1021/jacs.5c07246.

(110) Liu, X.-C.; Wang, T.; Zhang, Z.-M.; Yang, C.-H.; Li, L.-Y.; Wu, S.; Xie, S.; Fu, G.; Zhou, Z.-Y.; Sun, S.-G. Reaction Mechanism and Selectivity Tuning of Propene Oxidation at the Electrochemical Interface. *Journal of the American Chemical Society* **2022**, *144*, 20895–20902, DOI: 10.1021/jacs.2c09105.

(111) Huang, J. E. et al. Selective Electrified Propylene-to-Propylene Glycol Oxidation on Activated Rh-Doped Pd. *Journal of the American Chemical Society* **2024**, *146*, 8641–8649, DOI: 10.1021/jacs.4c00312.

(112) Dorchies, F.; Serva, A.; Crevel, D.; De Freitas, J.; Kostopoulos, N.; Robert, M.; Sel, O.; Salanne, M.; Grimaud, A. Controlling the Hydrophilicity of the Electrochemical Interface to Modulate the Oxygen-Atom Transfer in Electrocatalytic Epoxidation Reactions. *Journal of the American Chemical Society* **2022**, *144*, 22734–22746, DOI: 10.1021/jacs.2c10764.

(113) Struku, G.; Sinigalia, R.; Zanardo, A.; Pinna, F.; Michelin, R. A. Selective Oxidations of Olefins Catalyzed by platinum(II) Complexes. Use of Tert-Butyl Hydroperoxide and Potassium Caroate as Oxidants: Ketone Vs Epoxide Formation. *Inorganic Chemistry* **1989**, *28*, 554–559, DOI: 10.1021/ic00302a033.

(114) Winiwarter, A.; Silvioli, L.; Scott, S. B.; Enemark-Rasmussen, K.; Sariç, M.; Trimarco, D. B.; Vesborg, P. C. K.; Moses, P. G.; Stephens, I. E. L.; Seger, B.; Rossmeisl, J.; Chorkendorff, I. Towards an Atomistic Understanding of Electrocatalytic Partial Hydrocarbon Oxidation: Propene on Palladium. *Energy & Environmental Science* **2019**, *12*, 1055–1067, DOI: 10.1039/C8EE03426E.

(115) Yun, T. G.; Chen, B.; Wells, S.; Lim, Y.; Kim, J. S.; Guilherme Buzanich, A.; Radtke, M.; Waegele, M. M.; Risch, M.; Grimaud, A. Extrinsic and Intrinsic Factors Governing the Electrochemical Oxidation of Propylene in Aqueous Solutions. *Journal of the American Chemical Society* **2025**, *147*, 12318–12330, DOI: 10.1021/jacs.5c02585.

(116) Imbao, J.; van Bokhoven, J. A.; Nachtegaal, M. On the Promotional and Inhibitory Effects of Water on Wacker-Type Ethylene Oxidation Over Pd–Cu/Zeolite Y. *ACS Catalysis* **2021**, *11*, 8684–8691, DOI: 10.1021/acscatal.1c00507.

(117) Foley, D. J.; Waldmann, H. Ketones as Strategic Building Blocks for the Synthesis of Natural Product-Inspired Compounds. *Chemical Society Reviews* **2022**, *51*, 4094–4120, DOI: 10.1039/D2CS00101B.

(118) Grütering, C. et al. Methyl Ketones: A Comprehensive Study of a Novel Biofuel. *Sustainable Energy & Fuels* **2024**, *8*, 2059–2072, DOI: 10.1039/D4SE00035H.

(119) Ackermann, P. et al. Designed to Be Green, Economic, and Efficient: A Ketone-Ester-Alcohol-Alkane Blend for Future Spark-Ignition Engines. *ChemSusChem* **2021**, *14*, 5254–5264, DOI: 10.1002/cssc.202101704.

(120) Farrell, J. T.; Holladay, J.; Wagner, R. *Co-Optimization of Fuels & Engines: Fuel Blendstocks with the Potential to Optimize Future Gasoline Engine Performance; Identification of Five Chemical Families for Detailed Evaluation*; technical report NREL/TP–5400-69009, DOE/GO–102018-4970, 1434413; 2018, NREL/TP–5400–69009, DOE/GO–102018–4970, 1434413, DOI: 10.2172/1434413.

(121) Shao, S.; Xiang, X.; Li, X.; Zhang, H.; Xiao, R.; Cai, Y. Synergy in the Selective Production of Ketone Platform Compounds from Biomass Pyrolysis Vapors over CeO2 Catalysts. *Industrial & Engineering Chemistry Research* **2020**, *59*, 6460–6469, DOI: 10.1021/acs.iecr.9b06454.

(122) Lamb, J. R.; Mulzer, M.; LaPointe, A. M.; Coates, G. W. Regioselective Isomerization of 2,3-Disubstituted Epoxides to Ketones: An Alternative to the Wacker Oxidation of Internal Alkenes. *Journal of the American Chemical Society* **2015**, *137*, 15049–15054, DOI: 10.1021/jacs.5b10419.

(123) Jat, J. L.; Kumar, G. Isomerization of Epoxides. *Advanced Synthesis & Catalysis* **2019**, *361*, 4426–4441, DOI: 10.1002/adsc.201900392.

(124) Genç, S.; Gülcemal, S.; Günnaz, S.; Çetinkaya, B.; Gülcemal, D. Synthesis of -Alkylated Ketones via Selective Epoxide Opening/Alkylation Reactions with Primary Alcohols. *Organic Letters* **2021**, *23*, 5229–5234, DOI: 10.1021/acs.orglett.1c01765.

(125) Nair, D.; Luthra, S. S.; Scarpello, J. T.; White, L. S.; Freitas dos Santos, L. M.; Livingston, A. G. Homogeneous catalyst separation and re-use through nanofiltration of organic solvents. *Desalination* **2002**, *147*, 301–306, DOI: 10.1016/S0011-9164(02)00556-8.

(126) Cembellín, S.; Batanero, B. Organic Electrosynthesis Towards Sustainability: Fundamentals and Greener Methodologies. *The Chemical Record* **2021**, *21*, 2453–2471, DOI: 10.1002/tcr.202100128.

(127) Leech, M. C.; Garcia, A. D.; Petti, A.; Dobbs, A. P.; Lam, K. Organic Electrosynthesis: From Academia to Industry. *Reaction Chemistry & Engineering* **2020**, *5*, 977–990, DOI: 10.1039/D0RE00064G.

(128) Pelletier, J. D. A.; Basset, J.-M. Catalysis by Design: Well-Defined Single-Site Heterogeneous Catalysts. *Accounts of Chemical Research* **2016**, *49*, 664–677, DOI: 10.1021/acs.accounts.5b00518.

(129) Hoffmann, R., *Solids and Surfaces: A Chemist's View of Bonding in Extended Structures*; VCH: New York Weinheim, 1988.

(130) Deubel, D. V.; Sundermeyer, J.; Frenking, G. Mechanism of the Olefin Epoxidation Catalyzed by Molybdenum Diperoxo Complexes: Quantum-Chemical Calculations Give an Answer to a Long-Standing Question. *Journal of the American Chemical Society* **2000**, *122*, 10101–10108, DOI: 10.1021/ja0006649.

(131) Deubel, D. V.; Frenking, G.; Gisdakis, P.; Herrmann, W. A.; Rösch, N.; Sundermeyer, J. Olefin Epoxidation with Inorganic Peroxides. Solutions to Four Long-Standing Controversies on the Mechanism of Oxygen Transfer. *Accounts of Chemical Research* **2004**, *37*, 645–652, DOI: 10.1021/ar0400140.

(132) Cornell, C. N.; Sigman, M. S. Recent Progress in Wacker Oxidations: Moving toward Molecular Oxygen as the Sole Oxidant. *Inorganic Chemistry* **2007**, *46*, 1903–1909, DOI: 10.1021/ic061858d.

(133) Williams, K.; Limaye, A.; Weiss, T.; Chung, M.; Manthiram, K. Accounting for species' thermodynamic activities changes mechanistic interpretations of electrochemical kinetic data. *ChemRxiv* **2022**, DOI: 10.26434/chemrxiv-2022-vk5z9.

(134) Zhan, C.-G.; Nichols, J. A.; Dixon, D. A. Ionization Potential, Electron Affinity, Electronegativity, Hardness, and Electron Excitation Energy: Molecular Properties from Density Functional Theory Orbital Energies. *The Journal of Physical Chemistry A* **2003**, *107*, 4184–4195, DOI: 10.1021/jp0225774.

(135) Parr, R. G.; Szentpály, L. v.; Liu, S. Electrophilicity Index. *Journal of the American Chemical Society* **1999**, *121*, 1922–1924, DOI: 10.1021/ja983494x.

(136) Chattaraj, P. K.; Maiti, B.; Sarkar, U. Philicity: A Unified Treatment of Chemical Reactivity and Selectivity. *The Journal of Physical Chemistry A* **2003**, *107*, 4973–4975, DOI: 10.1021/jp034707u.

(137) Parr, R. G.; Pearson, R. G. Absolute Hardness: Companion Parameter to Absolute Electronegativity. *Journal of the American Chemical Society* **1983**, *105*, 7512–7516, DOI: 10.1021/ja00364a005.

(138) O'boyle, N. M.; Tenderholt, A. L.; Langner, K. M. cclib: A Library for Package-Independent Computational Chemistry Algorithms. *Journal of Computational Chemistry* **2008**, *29*, 839–845, DOI: 10.1002/jcc.20823.

(139) Roy, R. K.; Krishnamurti, S.; Geerlings, P.; Pal, S. Local Softness and Hardness Based Reactivity Descriptors for Predicting Intra- and Intermolecular Reactivity Sequences: Carbonyl Compounds. *The Journal of Physical Chemistry A* **1998**, *102*, 3746–3755, DOI: 10.1021/jp973450v.

(140) Rehbein, J.; Carpenter, B. K. Do We Fully Understand What Controls Chemical Selectivity? *Physical Chemistry Chemical Physics* **2011**, *13*, 20906–20922, DOI: 10.1039/C1CP22565K.

(141) Gómez-Marín, A. M.; Hernández-Ortiz, J. P. Langmuir–Hinshelwood Mechanism Including Lateral Interactions and Species Diffusion for CO Electro-Oxidation on Metallic Surfaces. *The Journal of Physical Chemistry C* **2014**, *118*, 2475–2486, DOI: 10.1021/jp409385k.

(142) Weinberg, W. H. EleyRideal Surface Chemistry: Direct Reactivity of Gas Phase Atomic Hydrogen with Adsorbed Species. *Accounts of Chemical Research* **1996**, *29*, 479–487, DOI: doi.org/10.1021/ar9500980.

(143) Schultz, Z. D.; Shaw, S. K.; Gewirth, A. A. Potential Dependent Organization of Water at the Electrified MetalLiquid Interface. *Journal of the American Chemical Society* **2005**, *127*, 15916–15922, DOI: 10.1021/ja0543393.

(144) Qiu, P.; Jiao, Y.; Hu, J.; Chen, S.; Li, P. Potential-Dependent Oxygenated Surface Phases and Interfacial Water Layers Underlie the High Overpotential and Mechanistic Switching of Oxygen Evolution on RuO2. *Angewandte Chemie International Edition*, *n/a*, e21856, DOI: 10.1002/anie.202521856.

(145) Keith, J. A.; McKone, J. R.; Snyder, J. D.; Tang, M. H. Deeper Learning in Electrocatalysis: Realizing Opportunities and Addressing Challenges. *Current Opinion in Chemical Engineering* **2022**, *36*, 100824, DOI: 10.1016/j.coche.2022.100824.

(146) Nutting, J. E.; Gerken, J. B.; Stamoulis, A. G.; Bruns, D. L.; Stahl, S. S. "How Should I Think about Voltage? What Is Overpotential?": Establishing an Organic Chemistry Intuition for Electrochemistry. *The Journal of Organic Chemistry* **2021**, *86*, 15875–15885, DOI: 10.1021/acs.joc.1c01520.

(147) Methyl Ethyl Ketone (MEK) Market Size to Reach USD 5.3 Bn by 2034, en.

(148) Torres-Vinces, L.; Contraras-Zarazua, G.; Heurta-Rosas, B.; Sanchez-Ramirez, E.; zednaSegovia-Hern, J. G. Methyl-Ethyl Ketone Production through Novel Intensified Process. *Chemical Engineering & Technology*, DOI: 10.1002/ceat.201900664.

(149) Goswami, C.; Saikia, H.; Tada, K.; Tanaka, S.; Sudarsanam, P.; Bhargava, S. K.; Bharali, P. Bimetallic Palladium–Nickel Nanoparticles Anchored on Carbon as High-Performance Electrocatalysts for Oxygen Reduction and Formic Acid Oxidation Reactions. *ACS Applied Energy Materials* **2020**, *3*, 9285–9295, DOI: 10.1021/acsaem.0c01622.

(150) Zhou, R.; Fan, X.; Ke, X.; Xu, J.; Zhao, X.; Jia, L.; Pan, B.; Han, N.; Li, L.; Liu, X.; Luo, J.; Lin, H.; Li, Y. Two-Dimensional Palladium–Copper Alloy Nanodendrites for Highly Stable and Selective Electrochemical Formate Production. *Nano Letters* **2021**, *21*, 4092–4098, DOI: 10.1021/acs.nanolett.1c01113.

(151) Chung, D. Y.; Lopes, P. P.; Farinazzo Bergamo Dias Martins, P.; He, H.; Kawaguchi, T.; Zapol, P.; You, H.; Tripkovic, D.; Strmcnik, D.; Zhu, Y.; Seifert, S.; Lee, S.; Stamenkovic, V. R.; Markovic, N. M. Dynamic Stability of Active Sites in Hydr(oxy)oxides for the Oxygen Evolution Reaction. *Nature Energy* **2020**, *5*, 222–230, DOI: 10.1038/s41560-020-0576-y.

(152) Kariuki, N. N.; Wang, X.; Mawdsley, J. R.; Ferrandon, M. S.; Niyogi, S. G.; Vaughey, J. T.; Myers, D. J. Colloidal Synthesis and Characterization of Carbon-Supported PdCu Nanoparticle Oxygen Reduction Electrocatalysts. *Chemistry of Materials* **2010**, *22*, 4144–4152, DOI: 10.1021/cm100155z.

(153) Christensen, G. L.; Langell, M. A. Characterization of Copper Palladium Oxide Solid Solutions by X-ray Diffraction, X-ray Photoelectron Spectroscopy, and Auger Electron Spectroscopy. *The Journal of Physical Chemistry C* **2013**, *117*, 7039–7049, DOI: 10.1021/jp310344r.

(154) Wang, J. Controlling dynamic reconstruction chemistry for superior oxygen-evolving catalysts. *Chem* **2023**, *9*, 1645–1657, DOI: 10.1016/j.chempr.2023.06.001.

(155) Suresh, G.; Bang, J. H. Precatalysts: A Missing Link in Efficient Oxygen Evolution Electrocatalysis. *Energy & Fuels* **2025**, *39*, 4669–4692, DOI: 10.1021/acs.energyfuels.4c06264.

(156) Liu, J.; Guo, L. *In Situ* Self-Reconstruction Inducing Amorphous Species: A Key to Electrocatalysis. *Matter* **2021**, *4*, 2850–2873, DOI: 10.1016/j.matt.2021.05.025.

(157) Brun, M.; Berthet, A.; Bertolini, J. XPS, AES and Auger parameter of Pd and PdO. *Journal of Electron Spectroscopy and Related Phenomena* **1999**, *104*, 55–60, DOI: 10.1016/S0368-2048(98)00312-0.

(158) Peuckert, M. XPS Study on Surface and Bulk Palladium Oxide, Its Thermal Stability, and a Comparison with Other Noble Metal Oxides. *The Journal of Physical Chemistry* **1985**, *89*, 2481–2486, DOI: 10.1021/j100258a012.

(159) Jeong, B.; Lee, D.; Park, J.-I.; Lee, S. M. Near Ambient Pressure XPS Investigation of Hydrous Palladium Oxide Under Water and Oxygen Gas Environments. *Journal of Physics D: Applied Physics* **2021**, *54*, 324001, DOI: 10.1088/1361-6463/ac0183.

(160) Biesinger, M. C.; Lau, L. W.; Gerson, A. R.; Smart, R. S. Resolving Surface Chemical States in XPS Analysis of First Row Transition Metals, Oxides and Hydroxides: Sc, Ti, V, Cu and Zn. *Applied Surface Science* **2010**, *257*, 887–898, DOI: 10.1016/j.apsusc.2010.07.086.

(161) Biesinger, M. C. Advanced Analysis of Copper X-Ray Photoelectron Spectra. *Surface and Interface Analysis* **2017**, *49*, 1325–1334, DOI: 10.1002/sia.6239.

(162) Segovia-Hernández, J. G.; Núñez-López, J. M.; Cossío-Vargas, E.; Juárez-García, M.; Sánchez-Ramírez, E. Electrification in the Chemical Industry and Its Role in Achieving Carbon Neutrality: Areas, Challenges, and Opportunities for Process Intensification. *RSC Sustainability* **2025**, *3*, 4955–4974, DOI: 10.1039/D5SU00356C.

(163) Ali, S. A.; Bangash, I. A.; Sajjad, H.; Karim, M. A.; Ahmad, F.; Ahmad, M.; Habib, K.; Nasir Shah, S.; Sami, A.; Laghari, Z. A.; Qudoos, A. Review on the Role of Electrofuels in Decarbonizing Hard-to-Abate Transportation Sectors: Advances, Challenges, and Future Directions. *Energy & Fuels* **2025**, *39*, 5051–5098, DOI: 10.1021/acs.energyfuels.4c06185.

(164) Iguchi, S.; Kataoka, M.; Hoshino, R.; Yamanaka, I. Direct Epoxidation of Propylene with Water at a PtOx Anode Using a Solid-Polymer-Electrolyte Electrolysis Cell. *Catalysis Science & Technology* **2022**, *12*, 469–473, DOI: 10.1039/D1CY01888D.

(165) Kumar, A.; Deka, S. Focused Review on the Use of Bimetallic Alloy Nanoparticle Electrocatalysts in Water Splitting Reactions. *The Journal of Physical Chemistry C* **2024**, *128*, 19037–19054, DOI: 10.1021/acs.jpcc.4c05903.

(166) Xiong, Y.; Ye, W.; Chen, W.; Wu, Y.; Xu, Q.; Yan, Y.; Zhang, H.; Wu, J.; Yang, D. PdCu Alloy Nanodendrites with Tunable Composition as Highly Active Electrocatalysts for Methanol Oxidation. *RSC Advances* **2017**, *7*, 5800–5806, DOI: 10.1039/C6RA25900F.

(167) Pei, G. X.; Liu, X. Y.; Yang, X.; Zhang, L.; Wang, A.; Li, L.; Wang, H.; Wang, X.; Zhang, T. Performance of Cu-Alloyed Pd Single-Atom Catalyst for Semihydrogenation of Acetylene under Simulated Front-End Conditions. *ACS Catalysis* **2017**, *7*, 1491–1500, DOI: 10.1021/acscatal.6b03293.

(168) Ma, M.; Zhu, W.; Shao, Q.; Shi, H.; Liao, F.; Shao, C.; Shao, M. Palladium–Copper Bimetallic Nanoparticles Loaded on Carbon Black for Oxygen Reduction and Zinc–Air Batteries. *ACS Applied Nano Materials* **2021**, *4*, 1478–1484, DOI: 10.1021/acsanm.0c02997.

(169) Porter, W. N.; Lin, Z.; Chen, J. G. Experimental and Theoretical Studies of Reaction Pathways of Direct Propylene Epoxidation on Model Catalyst Surfaces. *Surface Science Reports* **2021**, *76*, 100524, DOI: 10.1016/j.surfrep.2021.100524.

(170) Nijhuis, T. A.; Makkee, M.; Moulijn, J. A.; Weckhuysen, B. M. The Production of Propene Oxide: Catalytic Processes and Recent Developments. *Industrial & Engineering Chemistry Research* **2006**, *45*, 3447–3459, DOI: 10.1021/ie0513090.

(171) Roithová, J.; Schröder, D. Gas-Phase Models for Catalysis: Alkane Activation and Olefin Epoxidation by the Triatomic Cation Ag2O+. *Journal of the American Chemical Society* **2007**, *129*, 15311–15318, DOI: 10.1021/ja075628p.

(172) Wang, Y.; Xu, M.; Wang, X.; Ge, R.; Zhu, Y.-Q.; Li, A.-Z.; Zhou, H.; Chen, F.; Zheng, L.; Duan, H. Unraveling the Potential-Dependent Structure Evolution in CuO for Electrocatalytic Biomass Valorization. *Science Bulletin* **2023**, *68*, 2982–2992, DOI: 10.1016/j.scib.2023.09.033.

(173) Chen, S.; Farzinpour, F.; Kornienko, N. Dynamic Active Sites Behind Cu-Based Electrocatalysts: Original or Restructuring-Induced Catalytic Activity. *Chem* **2025**, *11*, 102575, DOI: 10.1016/j.chempr.2025.102575.

(174) Takamatsu, D.; Fukatani, N.; Yoneyama, A.; Hirano, T.; Hirai, K.; Yabuuchi, S.; Watanabe, K.; Kamiya, K.; Nakanishi, S. Dynamic Relocation of Copper Catalysts in Gas Diffusion Electrodes during CO2 Electroreduction. *Journal of the American Chemical Society* **2025**, *147*, 24103–24112, DOI: 10.1021/jacs.5c07944.

(175) Duan, Y.; Lee, J. Y.; Xi, S.; Sun, Y.; Ge, J.; Ong, S. J. H.; Chen, Y.; Dou, S.; Meng, F.; Diao, C.; Fisher, A. C.; Wang, X.; Scherer, G. G.; Grimaud, A.; Xu, Z. J. Anodic Oxidation Enabled Cation Leaching for Promoting Surface Reconstruction in Water Oxidation. *Angewandte Chemie International Edition* **2021**, *60*, 7418–7425, DOI: 10.1002/anie.202015060.

(176) Huang, X.; Groves, J. T. Oxygen Activation and Radical Transformations in Heme Proteins and Metalloporphyrins. *Chemical Reviews* **2018**, *118*, 2491–2553, DOI: 10.1021/acs.chemrev.7b00373.

(177) Zhang, R.; Pearce, P. E.; Duan, Y.; Dubouis, N.; Marchandier, T.; Grimaud, A. Importance of Water Structure and Catalyst–Electrolyte Interface on the Design of Water Splitting Catalysts. *Chemistry of Materials* **2019**, *31*, 8248–8259, DOI: 10.1021/acs.chemmater.9b02318.

(178) Li, S.; Ma, P.; Gao, C.; Liu, L.; Wang, X.; Shakouri, M.; Chernikov, R.; Wang, K.; Liu, D.; Ma, R.; Wang, J. Reconstruction-Induced NiCu-Based Catalysts Towards Paired Electrochemical Refining. *Energy & Environmental Science* **2022**, *15*, 3004–3014, DOI: 10.1039/D2EE00461E.

(179) Spöri, C.; Kwan, J. T. H.; Bonakdarpour, A.; Wilkinson, D. P.; Strasser, P. The Stability Challenges of Oxygen Evolving Catalysts: Towards a Common Fundamental Understanding and Mitigation of Catalyst Degradation. *Angewandte Chemie International Edition* **2017**, *56*, 5994–6021, DOI: 10.1002/anie.201608601.

(180) Jiang, Y.; Lim, A. M. H.; Yan, H.; Zeng, H. C.; Mirsaidov, U. Phase Segregation in PdCu Alloy Nanoparticles During CO Oxidation Reaction at Atmospheric Pressure. *Advanced Science* **2023**, *10*, 2302663, DOI: 10.1002/advs.202302663.

(181) Wang, C.; Chen, D. P.; Sang, X.; Unocic, R. R.; Skrabalak, S. E. Size-Dependent Disorder–Order Transformation in the Synthesis of Monodisperse Intermetallic PdCu Nanocatalysts. *ACS Nano* **2016**, *10*, 6345–6353, DOI: 10.1021/acsnano.6b02669.

(182) Oh, S.-H.; Hoflund, G. B. Chemical State Study of Palladium Powder and Ceria-Supported Palladium during Low-Temperature CO Oxidation. *The Journal of Physical Chemistry A* **2006**, *110*, 7609–7613, DOI: 10.1021/jp060435u.

(183) Lupan, O.; Postica, V.; Hoppe, M.; Wolff, N.; Polonskyi, O.; Pauporté, T.; Viana, B.; Majérus, O.; Kienle, L.; Faupel, F.; Adelung, R. PdO/PdO_2 Functionalized ZnO: Pd Films for Lower Operating Temperature H_2 Gas Sensing. *Nanoscale* **2018**, *10*, 14107–14127, DOI: 10.1039/C8NR03260B.

(184) Li, Y.; Yu, Y.; Wang, J.-G.; Song, J.; Li, Q.; Dong, M.; Liu, C.-J. CO Oxidation Over Graphene Supported Palladium Catalyst. *Applied Catalysis B: Environmental* **2012**, *125*, 189–196, DOI: 10.1016/j.apcatb.2012.05.023.

(185) Bai, J.; Wang, Q.; Yang, Z.; Yu, H.; Yang, L.; Zhu, J. The influence of reconstructive transformation from micro-/nanostructured copper(II) hydroxide to copper oxides as electrodes for high-performance supercapacitors. *Journal of Alloys and Compounds* **2024**, *976*, 173095, DOI: 10.1016/j.jallcom.2023.173095.

(186) Dreyer, W.; Guhlke, C.; Müller, R. A New Perspective on the Electron Transfer: Recovering the Butler–Volmer Equation in Non-Equilibrium Thermodynamics. *Physical Chemistry Chemical Physics* **2016**, *18*, 24966–24983, DOI: 10.1039/C6CP04142F.

(187) He, Z.-D.; Chen, Y.-X.; Santos, E.; Schmickler, W. The Pre-exponential Factor in Electrochemistry. *Angewandte Chemie International Edition* **2018**, *57*, 7948–7956, DOI: 10.1002/anie.201800130.

(188) Koper, M. T. M. Analysis of Electrocatalytic Reaction Schemes: Distinction Between Rate-Determining and Potential-Determining Steps. *Journal of Solid State Electrochemistry* **2013**, *17*, 339–344, DOI: 10.1007/s10008-012-1918-x.

(189) Huang, J.; Zhu, X.; Eikerling, M. The Rate-Determining Term of Electrocatalytic Reactions with First-Order Kinetics. *Electrochimica Acta* **2021**, *393*, 139019, DOI: 10.1016/j.electacta.2021.139019.

(190) Exner, K. S.; Over, H. Kinetics of Electrocatalytic Reactions from First-Principles: A Critical Comparison with the Ab Initio Thermodynamics Approach. *Accounts of Chemical Research* **2017**, *50*, 1240–1247, DOI: 10.1021/acs.accounts.7b00077.

(191) Exner, K. S. Why the Microkinetic Modeling of Experimental Tafel Plots Requires Knowledge of the Reaction Intermediate's Binding Energy. *Electrochemical Science Advances* **2022**, *2*, e2100037, DOI: 10.1002/elsa.202100037.

(192) Marshall, A. T.; Vaisson-Béthune, L. Avoid the Quasi-Equilibrium Assumption When Evaluating the Electrocatalytic Oxygen Evolution Reaction Mechanism by Tafel Slope Analysis. *Electrochemistry Communications* **2015**, *61*, 23–26, DOI: 10.1016/j.elecom.2015.09.019.

(193) Yang, D. Ketone-Catalyzed Asymmetric Epoxidation Reactions. *Accounts of Chemical Research* **2004**, *37*, 497–505, DOI: 10.1021/ar030065h.

Appendix A

SUPPLEMENTARY INFORMATION FOR CHAPTER 2

A.1 GC-MS Method and Calibration for Product Quantification

Epoxides and ketones generated in the liquid phase were extracted from the post-electrolysis electrolyte and were quantified by GC-MS as described in the Methods section. A HP-INNOWax capillary column was employed to analyze the hexane extract solutions containing epoxides and ketones, which are challenging to resolve due to their similar polarities and boiling points, particularly for the linear products. Rather than an isothermal method, a temperature-programmed GC method was developed and optimized using 1,2-epoxyhexane and 2-hexanone as model compounds (Figure A.1). The GC column outlet was connected directly to a quadrupole mass analyzer, and extracted ion chromatograms isolating the specific mass-to-charge ratio were used to generate the most resolved chromatogram for each analyte and to perform quantification.

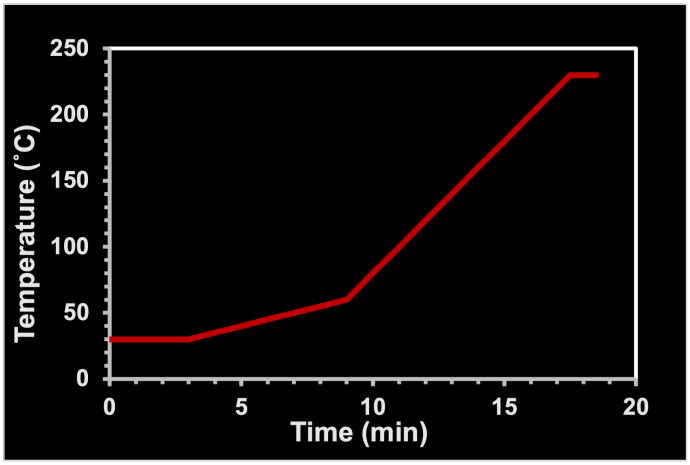

Figure A.1: Temperature profile of the optimized GC method for sufficient separation of ketones and epoxides.

External calibration curves were constructed to account for instrumentation and extraction errors (Figure A.2). Calibration curves for oxidized products (epoxides and ketones) of three olefin substrates, 1-hexene, cyclooctene, and cyclopentene, were obtained. For 1-hexene, 1,2-epoxyhexane and 2-hexanone were used (we assumed the same systematic errors for other possible carbonyl products such as

hexanal); for cyclooctene, cyclooctene oxide and cyclooctanone; cyclopentene oxide and cyclopentanone for cyclopentene. TMB concentrations were maintained at 0.5 mM in all calibration solutions. For each oxidized product, two calibration curves were obtained. The first one was to correct any analytical errors present in GCMS instrument by plotting the GC peak ratio of the oxygenated compound and TMB against known concentrations of the oxygenated compound (Figure A.2a, c, e). The extraction calibration was created by repeating hexane extraction procedure on electrolyte solutions (0.1 M $TBABF_4$ and 10 M water in acetonitrile) with varying concentrations of the oxygenated products. For each olefin substrate, its epoxide and ketone were mixed at the same concentration in the calibration to mimic the post-electrolysis electrolyte conditions. The extraction calibration curves were obtained by plotting the known concentrations of the analytes against the extracted concentrations (values obtained from the GC calibration curves) (Figure A.2b, d, f). Parameters obtained from the linear regression were used for quantification calculations.

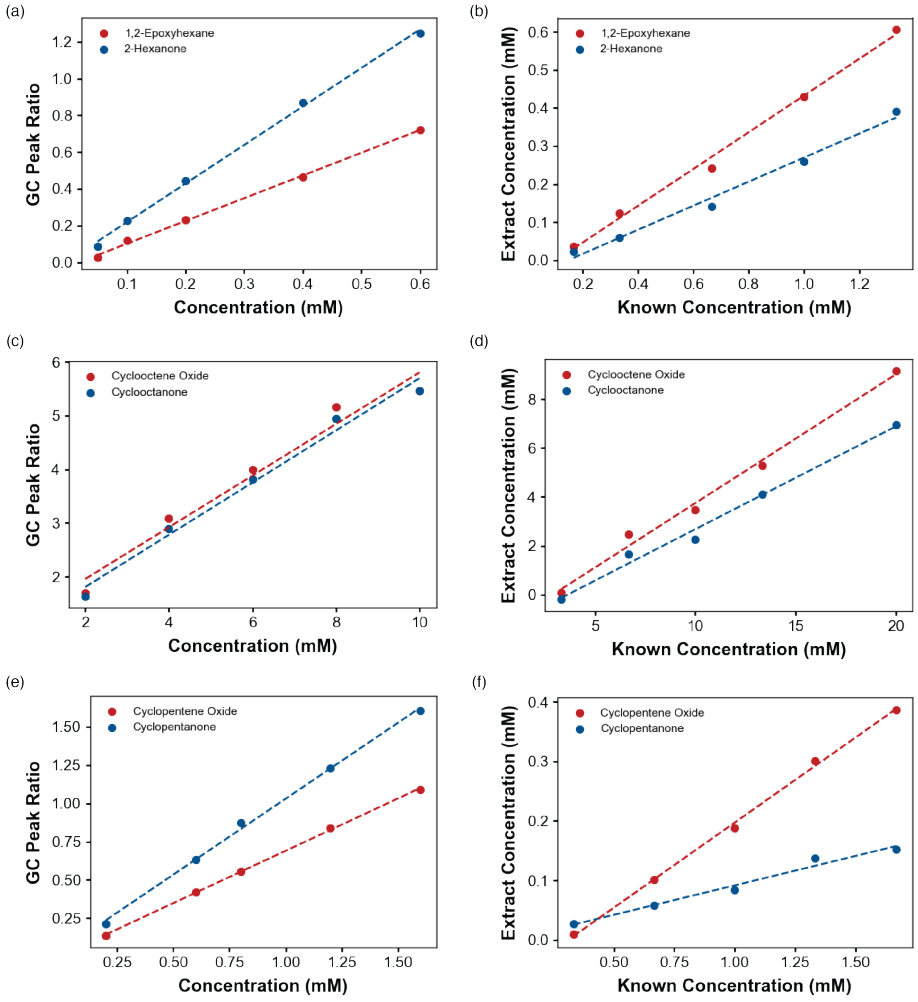

(f) Slope and y-intercept for the line fitting of the calibration curves

	GCMS Correction		Extraction Correction	
	Slope	y-intercept	Slop	y-intercept
1,2-epoxyhexene	1.237	-0.022	0.482	-0.050
2-hexanone	2.096	0.09	0.315	-0.046
Cyclooctene oxide	0.481	0.998	0.527	-1.532
Cyclooctanone	0.486	0.8383	0.425	-1.537
Cyclopentene oxide	0.634	0.006	0.286	-0.089
Cyclopentanone	0.992	0.034	0.099	-0.008

Figure A.2: Calibration curves for GC-MS quantification.

A.2 Free Energy Calculation

Relative free energies of the ketone and epoxide were calculated using DFT at the M062X/def2-SVPD level and plotted relative to their corresponding alkene (Figure A.3). For the three alkenes shown, the free energies of the epoxide and

ketone products are nearly identical, suggesting that the selectivity is likely not an outcome of thermodynamics. It should be noted, however, that these calculations do not account for the full reaction, including water as well as the applied potential. These results were therefore treated as a preliminary check rather than a rigorous thermodynamic analysis.

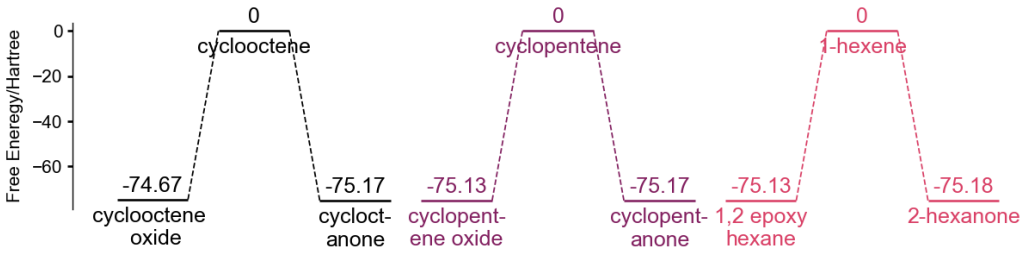

Figure A.3: Computed free energies of alkenes and their epoxide and ketone products.

A.3 Synchrotron XAS Measurements

Operando and *ex situ* XAS measurements were conducted at the Stanford Synchrotron Radiation Lightsource (beam line 4–1). Beam line 4-1 is a high-flux wiggler station in the 5-38 keV range. All XAS spectra were acquired in the fluorescence mode, with the sample facing the incident beam at a 45-degree angle and the detector orthogonal to the sample.

The standard Mn power materials (i.e., Mn_3O_4, MnO_2) were diluted with sucrose to achieve about 10-15% metal w%, minimizing self-absorption and ensuring sufficient transmission signals (Figure A.4a). The resulting mixture was ground with a mortar and a pestle until a homogeneous, fine-grained powder was obtained (Figure A.4b). A small amount of the finely ground powder was placed on the sticky side of the Kapton tape which was taped down on a piece of weighing paper with Scotch tape; the powder was then spread across the Kapton tape with the excess removed to create a thin, uniform layer (Figure A.4c-d). The Scotch tape was removed, and the sample-loaded Kapton tape was then folded and pressed down to create a self-containing pouch as shown in Figure A.4e. At BL 4-1, the sample pouch was placed on a 3D-printed sample holder provided by the Solution Phase Chemistry Group in Stanford PULSE Institute at SLAC National Acceleration Laboratory (Figure A.4f).

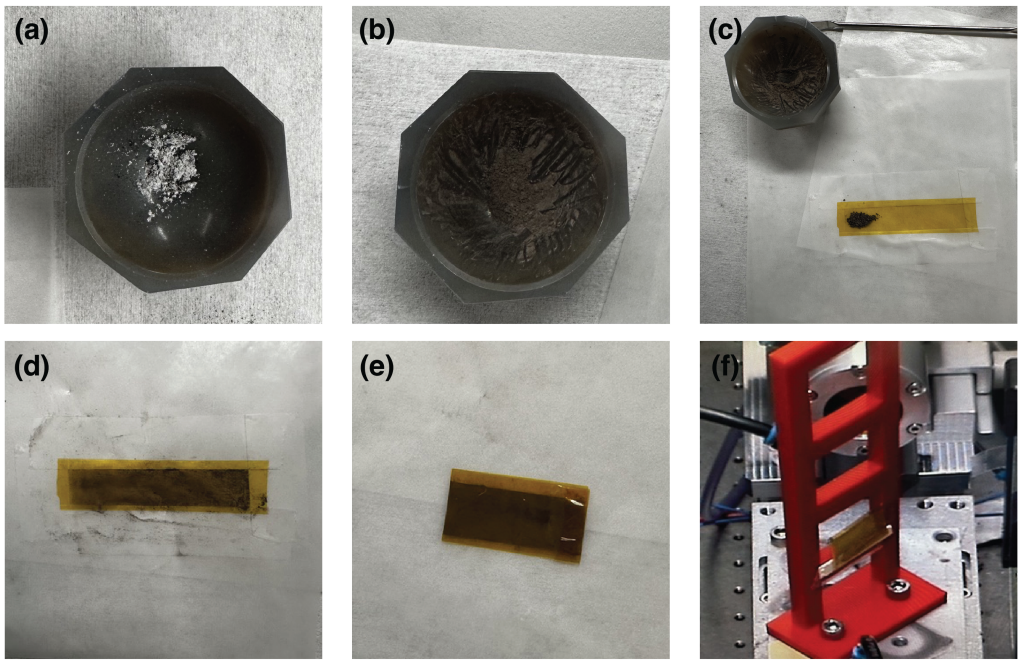

Figure A.4: Powder sample preparation (a-e) and the sample holder (f) at BL 4-1 for *ex situ* XAS measurements.

A standard XAS Mn foil was used to calibrate Mn edge energy. The XAS spectra for the standard samples were acquired with a passivated implanted planar silicon semiconductor detector, and a Canberra 30-element Ge detector were used for the *operando* measurements using a standard electrochemical cell with a Kapton window at the catalyst (Figure A.5). Several pieces of phosphorus paper were placed around the catalyst window to visualize the X-ray position for the alignment. A Z-1 (Cr) filter was positioned in front of the detectors to absorb adventitious low-energy fluorescence. For *operando* experiments, the bulk electrolysis was conducted following the same electrochemical protocol.

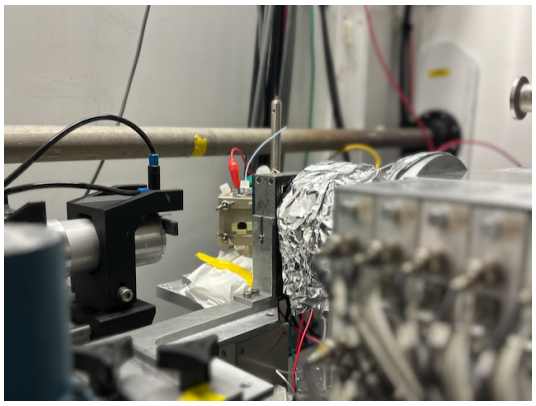

Figure A.5: Experimental setup for *operando* XAS measurements.

A.4 Ketone Formation via Epoxide Ring-Opening vs. Direct Pathway

Ketones can be generated directly from alkenes, as illustrated in Wacker-Tsuji oxidation,[98] or indirectly via epoxide rearrangement, in which the alkene is first converted into an epoxide that subsequently undergoes ring-opening to yield the corresponding ketone. (Figure A.6)[122–124] Distinguishing between these two pathways is therefore an essential first step in understanding ketone/epoxide selectivity in alkene electrooxidation.

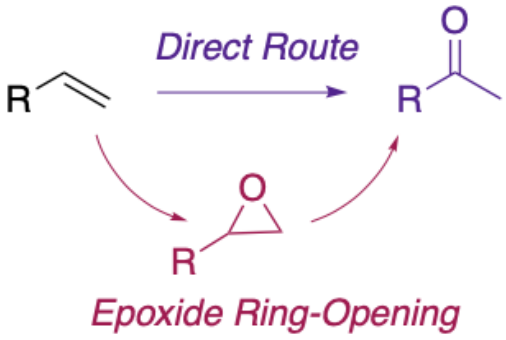

Figure A.6: Two possible pathways for ketone formation.

To differentiate between the two pathways, 5 mM cyclooctene oxide was added to the electrolyte containing 0.2 M cyclopentene and 5 M water prior to the electrolysis. If ketone formation arises from the indirect epoxide-ring opening route, cyclooctanone would be expected in addition to the cyclopentene-derived products under the reaction condition. However, no cyclooctanone was detected after anodic polarization at 1.45 V vs. $Fc/Fc^+$with 20 C of charges passed, inconsistent with the indirect pathway. In addition, ketones have been reported as organic catalysts for

epoxidation of alkenes in homogeneous systems,[193] where ketones with electron-withdrawing groups, such as F and CF_3, were observed to be competent catalysts in the presence of oxone and sodium bicarbonate. Although predicting electrochemical reactivity from homogeneous precedent is complicated by the complex microenvironment at the electrified interface, the possibility of ketone-catalyzed epoxidation was nonetheless tested by repeating the experiment with 5 mM cyclooctanone in place of cyclooctene oxide. No cyclooctanone-derived products were detected after the electrolysis, indicating the observed ketone and epoxide formation is attributed to direct electrochemistry at the MnO_x surface rather than secondary solution-phase reactions.

A.5 Additional Figures

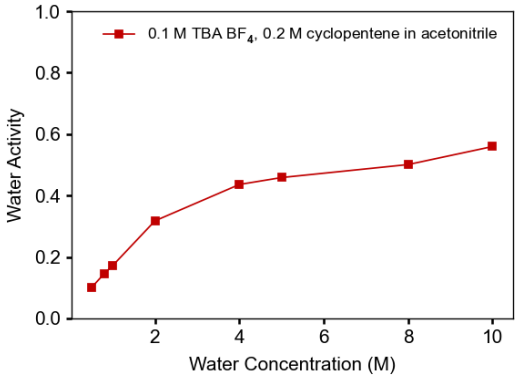

Figure A.7: Measured water activity for different water concentrations in the electrolyte consisting of 0.1 M $TBABF_4$ and 0.2 M cyclopentene. The cyclopentene concentration was found to have minimal effects on activity-concentration relationship.

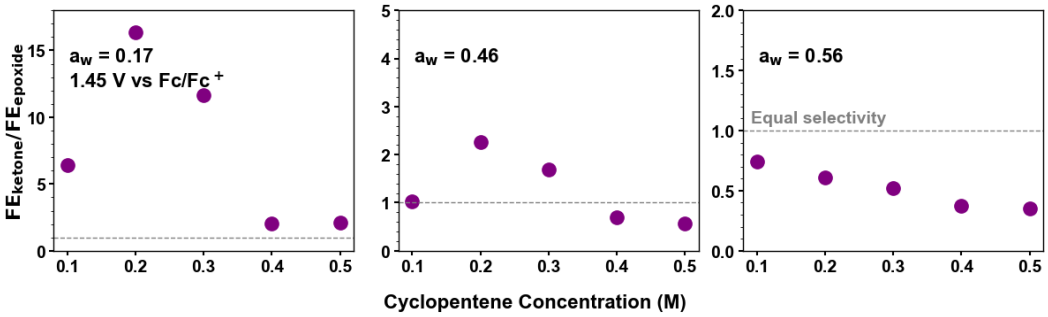

Figure A.8: Ketone/epoxide selectivity, expressed as the ratio of FE_{ketone} to $FE_{epoxide}$, as a function of cyclopentene concentrations across different water activities at a constant anodic applied potential. The dash line marks a ratio of unity, corresponding to equal selectivity between cyclopentanone and cyclopentene oxide.

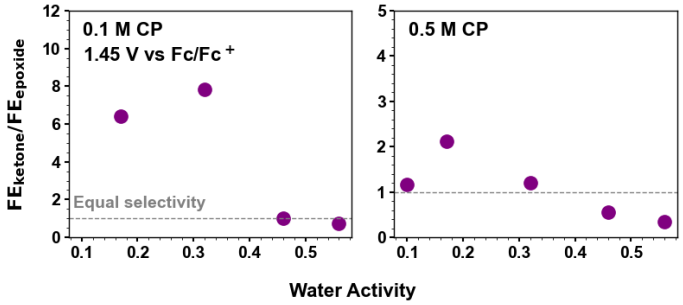

Figure A.9: Ketone/epoxide selectivity, expressed as the ratio of FE_{ketone} to $FE_{epoxide}$ as a function of water activity across different cyclopentene concentrations at a constant anodic applied potential.The dash line marks a ratio of unity, corresponding to equal selectivity between cyclopentanone and cyclopentene oxide.

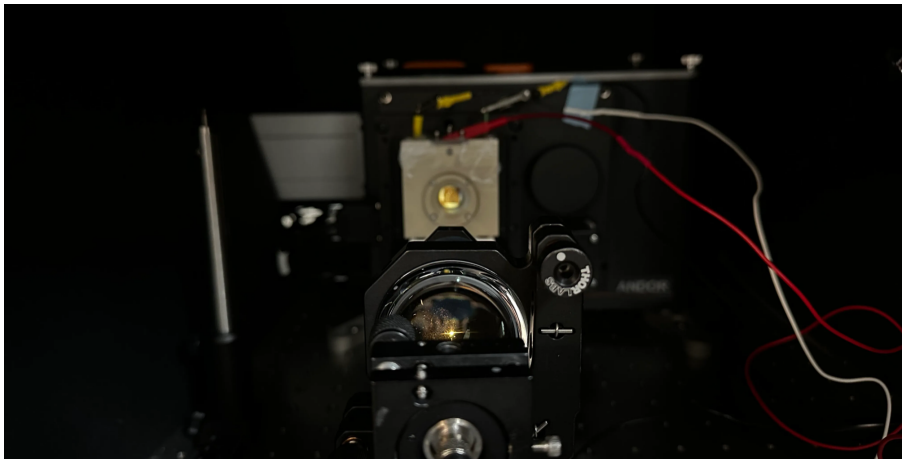

Figure A.10: Experimental setup for operando SEC.

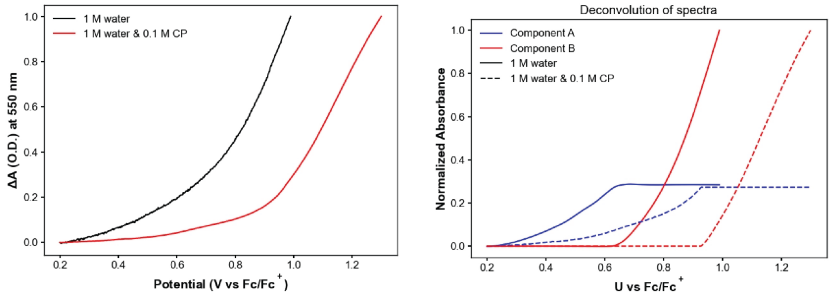

Figure A.11: The absorption change of MnO_x at 550 nm as a function of applied potential at 1 M water with and without cyclopentene. The spectra are deconvoluted into two components.

Appendix B

SUPPLEMENTARY INFORMATION FOR CHAPTER 3

B.1 Additional Electrochemical Methods

Cyclic voltammetry. The cyclic voltammetry (CV) curves were started at OCV and swept first anodically to 2.0/2.1 V vs. RHE and then cathodically back to OCV at a scan rate of 5 mV/sec. The CV scans were repeated at least 3 times to check for the catalyst stability. The second scan was usually chosen for analysis. Prior starting CV scans, 1-butene was bubbled into the electrolyte for 30 min at 10 sccm to ensure saturation; during the CV scans, 1-butene was sparged in the headspace of the electrochemical reactor to avoid additional convection from the gas flow.

Double-layer capacitance measurement. The double-layer capacitance (DLC) of the catalyst-loaded electrodes were measured to estimate the electrochemically active surface area. CV scans spanning ±50 mV of the OCV were recorded at scan rates of 20, 40, 60, and 100 mV/sec. The resulting capacitive CV curves (Figure B.4a) were used to calculate the capacitive current (Δi) by taking the difference between anodic and cathodic currents averages across ±10 mV of the OCV at each scan rate. Δi was plotted as a function of the scan rate, and the slope of the linear regression line was divided by 2 to obtain the DLC of the electrode (Figure B.4b).

B.2 Additional Figures for Chapter 3

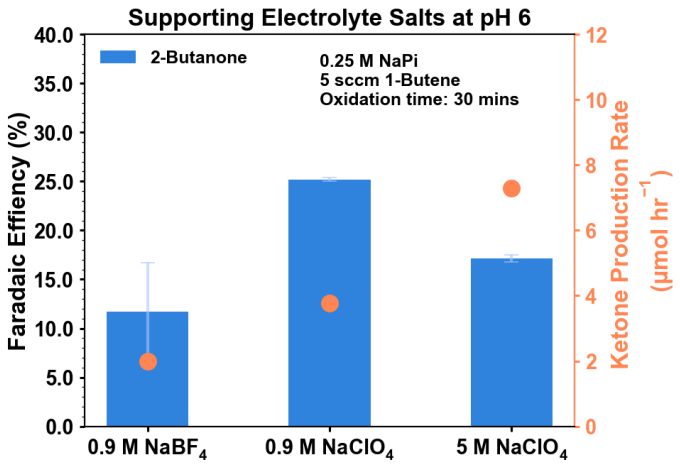

Figure B.1: Effects of supporting electrolyte salts on 1-butene ketonization.

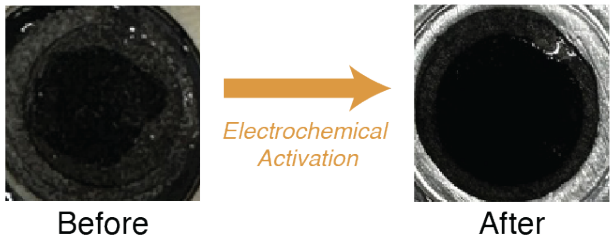

Figure B.2: The electrode loaded with PdCu/C before and after electrochemical activation by SWV.

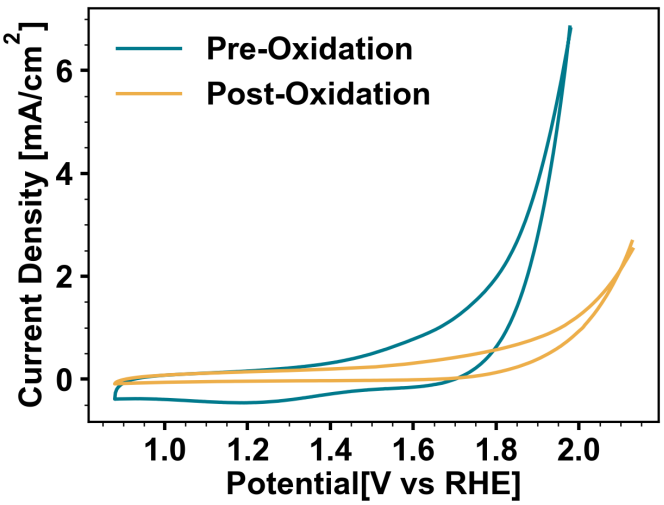

Figure B.3: CV profile of PdCu/C before and after electrochemical activation by SWV. The scans were recorded at 5 mV/sec scan rate with 100% automatic iR compensation. The second scans are shown.

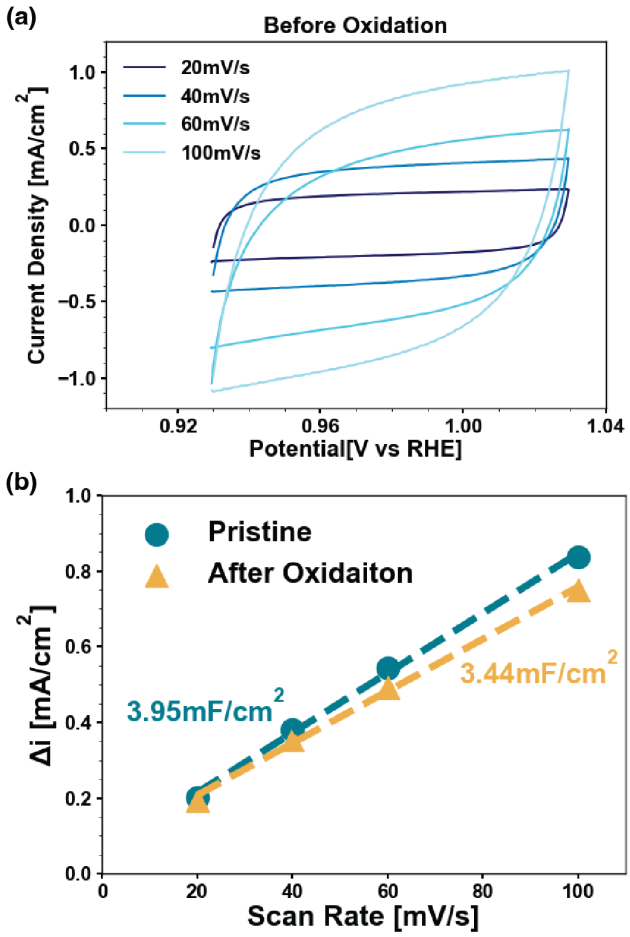

Figure B.4: Double-layer capacitance measurement of PdCu/C in the pristine form and after electrochemical oxidation by SWV. (a) CV curves at various scan rates over PdCu/C in the aqueous electrolyte before activation in the presence of 1-butene. (b) Capacitive current densities at different scan rates for PdCu/C before and after activation.

Appendix C

SUPPLEMENTARY INFORMATION FOR CHAPTER 4

The material in this appendix is adapted from the Supporting Information published with Jiang, C.; Moss, B.; Lindenfelser, A.; Kim, J. T.; Li, Y.; Manthiram, K. Metallic Pd–Cu Alloy Phases Drive Selective Heterogeneous Electrochemical Ketonization of 1-Butene. *ACS Catalysis* **2026**, *16*, 7429–7438, DOI: 10.1021/acscatal.5c08675. Reproduced with permission from the American Chemical Society.

C.1 Materials

Table C.1: Chemicals and materials used in this study.

Chemical & Material	Specification	Vendor
Catalyst Preparation		
Palladium(II) chloride ($PdCl_2$)	99.9% metals basis, Pd 59% min	Thermo Scientific 011034.04
Copper(II) chloride ($CuCl_2$)	Anhydrous, 99%, extra pure	Acros Organics 206532500
Trimethyl(tetradecyl)ammonium bromide (TTAB)	99%	Sigma Aldrich T4762
L-Ascorbic acid	Reagent grade, crystalline	Sigma Aldrich A7506
Electrochemical & Reactivity Study		
1-Butene	99%	Sigma Aldrich 295051
Sodium perchlorate ($NaClO_4$)	ACS reagent, 98.0%	Sigma Aldrich 410241
Sodium phosphate monobasic (NaH_2PO_4)	BioReagent, anhydrous, 98%	Sigma Aldrich S3139
Sodium phosphate dibasic heptahydrate ($Na_2HPO_4 \cdot 7\,H_2O$)	99+%, for analysis	Acros Organics 206512500
Sodium phosphate (Na_3PO_4)	96%	Sigma Aldrich 342483
Phosphoric acid (H_3PO_4)	85%, analytical reagent	Mallinckrodt 3563
DSS	Assay 99%	Fluka Chemika 92754
Deuterium oxide (D_2O)	For NMR, 99.8 atom % D	Thermo Scientific 166300250
Sigracet 39BB	5 wt.% PTFE	Fuel Cell Store 63070043
Platinum foil (Pt)	0.025 mm, 99.99%	Beantown Chemical 122810
Catalyst Characterization		
Cu foil	0.8 cm × 2.6 cm × 5 µm	easyEXAFS
Copper(I) oxide (Cu_2O)	≥99.99% trace metals basis	Sigma Aldrich 566284
Copper(II) oxide (CuO)	99.999% trace metals basis	Sigma Aldrich 203130
Copper(II) hydroxide ($Cu(OH)_2$)	93.51%	CHEM-IMPEX 27260

C.2 Catalyst Preparation

Catalyst Synthesis

The bimetallic PdCu catalyst was synthesized via a co-reduction method that was adapted from a literature procedure.[150] 0.25 mmol of $PdCl_2$ (44 mg) was dissolved in 5 mL of 0.1 M HCl solution, and separately, 0.25 mmol of $CuCl_2$ (34 mg) was dissolved in 5 mL of Milli-Q water. To fully dissolve $PdCl_2$, the solution was rigorously stirred for at least 30 min, resulting in a partially transparent, dark red solution. 1.25 mmol of TTAB (421 mg) was dissolved in 200 mL of Milli-Q water in a 500 mL round-bottle flask charged with a stir bar. The TTAB solution was cooled and kept below 10 °C with the aid of a circulating cooler (Figure C.1a). The temperature at the cooler was set at 8.5 °C, ensuring the content of the reaction vessel was sufficiently cooled. The Pd and Cu precursor solutions were transferred to the chilled TTAB solution and stirred for 5 minutes, leading to a cloudy orange solution. This was followed by the addition of 6 mmol of L-ascorbic acid (1.06 g). The reaction mixture was kept cool and stirred rigorously overnight. As the reaction proceeded, the solution mixture gradually became darker; the overnight stirring resulted in a dark gray, cloudy solution (Figure C.1b). The final solution was transferred to 50 mL centrifuge tubes and centrifuged for 30 minutes at 9000 rpm. The supernatant was removed, and Milli-Q water was added to the centrifuge tubes to disperse the precipitate, and the precipitates were combined in a single centrifuge tube. The mixture was then washed with Milli-Q three more times, with the supernatant discarded. The final precipitate was dried at 60 °C overnight under vacuum, and the catalyst powder, reddish brown in color, was collected and ground with a mortar and a pestle so that the catalyst powder had a consistent and fine texture. The powder was stored at room temperature.

The pure Pd material was synthesized following the same procedure with 0.5 mmol of $PdCl_2$ (88 mg) and no addition of $CuCl_2$.

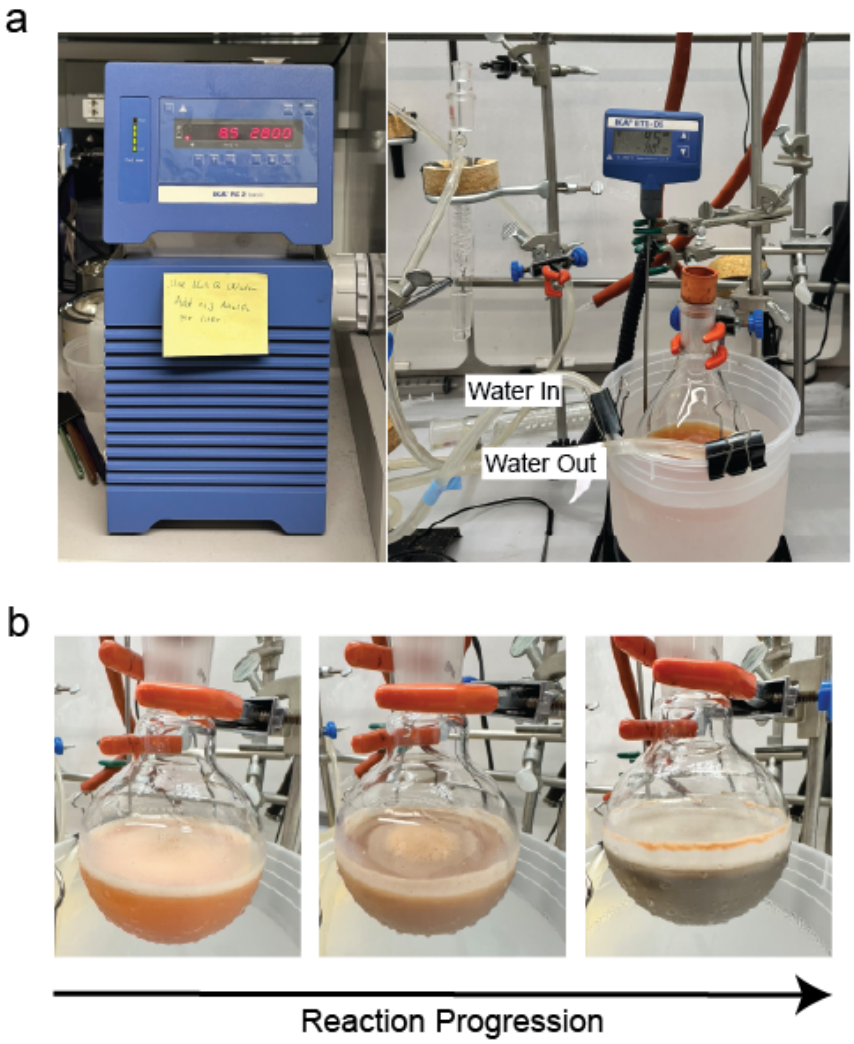

Figure C.1: Reaction setup for catalyst synthesis and color change of the reaction mixture. (a) Circulating cooler setup for keeping the reaction mixture below 10 °C. (b) The reaction mixture turns darker as the reaction proceeds. Note that the last picture shows the reaction mixture after being stirred for ~4 h. Typically, the reaction is allowed to stir at 10 °C overnight (~14-18 h).

Catalyst Ink and Catalyst-loaded Electrode Preparation

5 mg of the catalyst powder and 2 mg of Vulcan XC-72R carbon black powder were dispersed in 1 mL of a water-IPA solution (water : IPA = 1:4 volumetric ratio) as the catalyst ink. To ensure homogeneity, the catalyst ink was sonicated for 20 minutes before use. A total of 300 μL of catalyst ink was drop-casted in 50 μL increments on one side of a 14 mm-diameter Sigracet carbon paper (Sigracet 39 BB, 5 wt.% PTFE, Fuel Cell Store). The carbon paper was allowed to dry after each 50 μL addition

until no visible liquid could be observed so that no ink was able to completely penetrate through the carbon paper. To facilitate the drying process, the carbon paper was placed on a hot plate lined with aluminum foil, and the temperature was set at 80 °C. Finally, the carbon paper was coated with 50 μL of 2 wt.% Nafion solution and dried at 80 °C overnight. The 2 wt.% Nafion solution was prepared by diluting a commercially available 5 wt.% Nafion solution with IPA.

For the thermally treated electrode (HT-PdCu), catalyst-coated carbon paper was transferred to a muffle furnace and was heated at 400 °C for 3 h under static air; the ramping rate of the furnace was set at 10 °C/min from room temperature to 400 °C. The annealed carbon paper was then coated with the 2 wt.% Nafion solution and dried at 80 °C overnight.

C.3 Electrolyte Preparation

Aqueous electrolyte solutions were used in the electrochemical studies. All electrolyte formulations used 0.9 M $NaClO_4$, and the bulk pH was controlled via the 0.25 M sodium phosphate buffer. The electrolytes were prepared from 5 M $NaClO_4$ and 1 M/0.5 M sodium phosphate stock solutions. The buffer solutions were prepared by dissolving the theoretically determined amount of H_3PO_4, Na_2HPO_4, NaH_2PO_4, and NA_3PO_4 in Milli-Q water and adjusting to the desired pH value with 1 M NaOH and 1 M H_3PO_4 solutions (Table C.2).

Table C.2: Phosphate buffer compositions at different pH values.

Intended pH	**Molarity**	**[H_3PO_4] (M)**	**[NaH_2PO_4] (M)**
4	1	0.0139	0.9861
Intended pH	**Molarity**	**[NaH_2PO_4] (M)**	**[Na_2HPO_4] (M)**
5	1	0.9937	0.0630
6	1	0.9405	0.0595
7	1	0.6126	0.3874
8	1	0.1365	0.8635
9	0.5	0.0078	0.9922
Intended pH	**Molarity**	**[Na_3PO_4] (M)**	
12	0.5	0.5	

C.4 Catalyst Characterization

Powder X-ray diffraction (XRD) analysis

The X-ray diffraction patterns of the synthesized catalysts were obtained using an X-ray powder diffractometer (Rigaku SmartLab) with Cu Ka radiation (λ =1.54056Å). The diffraction patterns were collected from 10-90° 2θ at a step size of 0.01° and 5° per minute. Data were processed using HighScore software.

X-ray photoelectron spectroscopy (XPS)

The XPS samples for the standard materials (Cu, CuO, $Cu(OH)_2$) and the catalysts were prepared by pressing the sample powders into a 3-mm diameter pellet using a hydraulic press. After electrolysis, the electrodes were rinsed with Milli-Q water and dried under vacuum in a vacuum desiccator for at least 12 h before measurements. The XPS samples were directly attached to the sample platen with the platen's clips. The sample platen was then loaded in the Sample Entry Chamber and purged under vacuum overnight, followed by the transfer to the Sample Analysis Chamber. The XPS spectra were acquired using an AXIS Nova spectrometer by Kratos Analytical and analyzed with Casa XPS software.

X-ray absorption spectroscopy (XAS)

The XAS measurements were collected with an easyXAFS300 spectrometer. The standard samples (Cu, CuO, $Cu(OH)_2$) and synthesized catalyst powders were diluted with sucrose to ca. 10% for the standard samples and 15-18% for catalysts and homogenized with a mortar and pestle; the resulting mixture was pressed into a 3-mm diameter pellet using a hydraulic press and sealed with Kapton. The post-electrolysis spectra were obtained by pressing the spent catalyst-loaded carbon paper electrodes (which were dried in a vacuum desiccator for at least 12 h) into a 3-mm diameter pellet to increase the volumetric concentration. The XAS samples were attached to the spectrometer's sample wheel, and Cu foil was used as the standard to calibrate the energy shift. The data collection was performed with X-ray operating at 40 kV and 25 mA; two scans were collected for the Cu foil, and 10 scans for the standard materials and catalysts in transmission mode at Cu K-edge at room temperature. The energy calibration was obtained from the difference between the first peak of the first derivative of the Cu foil standard and the tabulated values for Cu K-edge; the same energy shift was applied to all the samples. The raw spectra were analyzed and processed utilizing the ATHENA suite to obtain the normalized spectra. The linear combination fitting function in ATHENA was used to fit the

spectra of the standard samples to those of the catalysts.

Scanning electron microscopy (SEM) and X-ray energy-dispersive spectroscopy (EDS)

The morphologies of the pristine and post-electrolysis catalysts were collected with a ZEISS 15500VP field emission SEM equipped with an Oxford X-MAS SDD EDS system. Catalyst-loaded carbon paper electrodes and vacuum-dried post-electrolysis carbon paper were attached to the SEM holders with carbon tape; extra copper tape was used to ground the sample. A turbo carbon evaporator was used to coat the sample with a thin layer of carbon (<10 nm). SEM images were obtained with an acceleration voltage of 2 kV, and the EDS were acquired at an acceleration voltage of 15 kV.

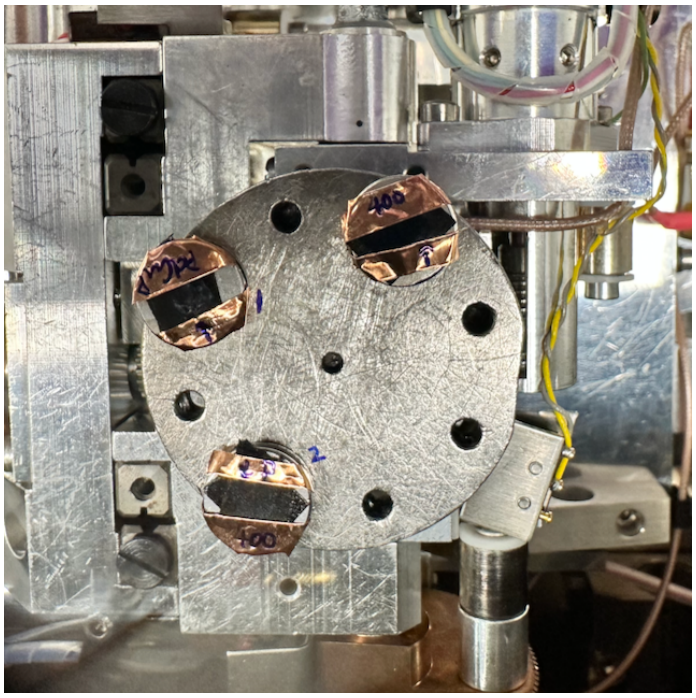

Figure C.2: SEM sample loading with copper tape.

High-resolution transmission electron microscopy (HRTEM)

All TEM characterizations were performed using an FEI Titan 80–300 scanning transmission electron microscope operated at 300 kV equipped with a field-emission gun, Oxford X-MaxN 100TLE 100 mm^2 SDD x-ray spectrometer, and Gatan Ultrascan digital camera. A small amount of diluted PdCu catalyst ink was drop-casted on to the TEM grid. The post-electrolysis PdCu-loaded carbon paper was sonicated with a probe sonicator in IPA to extract the catalyst powder. The resulting homoge-

neous solution was drop-casted on to the TEM grid. The sample-loaded TEM grids were allowed to air-dry for 2 h.

Electrochemistry study

Electrochemical experiments were carried out in a sandwich-style electrochemical cell with a piece of platinum foil (Pt, 0.025 mm, 99.99%) as the counter electrode. The carbon paper was punched in a 14 mm-diameter disk, and 1 cm2 of the electrode was exposed to the electrolyte in the assembled electrochemical cell. A leakless Ag/AgCl reference electrode (2.0 mm diameter, eDAQ) was used as a reference electrode. References were calibrated against a reversible hydrogen electrode weekly, which was done by bubbling hydrogen gas at ambient pressure into the electrolyte solution with a platinum wire as the working electrode. Aluminum foils (Reynold's Wrap) acted as the current collectors for both the anode and cathode. Hydrophobic carbon paper (Toray Carbon Paper 120, 5% wet-proofed, Fuel Cell Store) was placed behind the catalyst-loaded carbon paper to prevent electrolyte flooding, as it was observed that Sigracet carbon paper was susceptible to electrolyte flooding, resulting in poor gas phase transport. The total volume of electrolyte is 3.6 mL consisting of 0.25 M of sodium phosphate buffer of varying pHs (see Table C.2 for buffer stock solution) and 0.9 M NaClO4 in Milli-Q water; 1-butene flow was adjusted with a mass flow controller (Alicat) to ensure an ambient flow of 5 standard cubic centimeters per minute (sccm) in a pass-through gas diffusion configuration during the bulk electrolysis.

The electrochemical measurements were conducted with a BioLogic VMP3 Multichannel potentiostat. The solution resistance was measured at open circuit potential (OCP) by electrochemical impedance spectroscopy techniques from 200 kHz to 100 mHz at 10 mV amplitude, and the resulting resistance determined from the x-intercept in the Nyquist plot was input for 100% iR compensation. The electrolysis experiments were conducted at fixed applied potentials for 30 minutes.

Catalyst-loaded carbon papers were discarded after every experiment, and all other cell parts, including the counter electrode, were first rinsed with deionized water and sonicated in 10% nitric acid solution, followed by Milli-Q water for 5 minutes and 10 minutes, respectively, to remove any contaminants. The cell parts were air-dried.

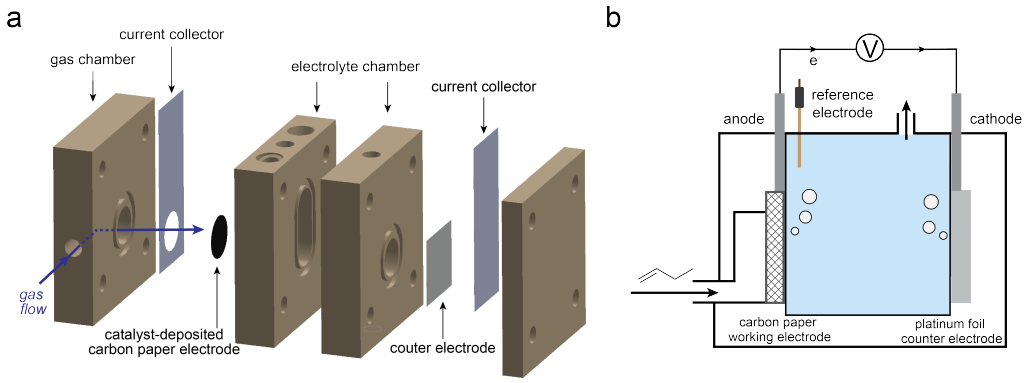

Figure C.3: Gas diffusion electrochemical cell used for electrochemical studies. (a) Cell part assembly. (b) A schematic of the gas diffusion cell operated in a flow-through configuration for 1-butene electro-oxidation.

C.5 Product Analysis

The post-electrolysis electrolytes were collected with a glass pipette and dispensed into a 5 mL volumetric flask. The electrolyte chamber was rinsed with additional Milli-Q water to remove any electrolyte residue, and the Milli-Q water was then transferred to the volumetric flask until the total volume reached the mark. The rinsing was usually done twice. 540 μL of the electrolyte was added to a clean NMR tube in addition to 60 μL of the internal standard solution, ~1mM 3-(Trimethylsilyl)-1-propanesulfonic acid sodium salt (DSS) in D_2O. The products were quantified using ^1H-NMR (nuclear magnetic resonance) spectroscopy. The NMR spectra were acquired on a Bruker 400 MHz spectrometer with water suppression performed. The ^1H probe was automatically tuned, and the solvent lock was done with 90% H_2O and 10% D_2O, and gradient shimming and auto-gain were used. 32 scans were collected per sample, and relaxation delay was set at 3 seconds. Products were quantified by taking the ratio of the areas of the peaks of interest to the peak at 0.0 ppm belonging to DSS. Auto phase correction, baseline correction with the Whittaker Smoother method, and further peak suppression at 4.7 ppm were performed using MestReNova software before the integration of peaks of interest.

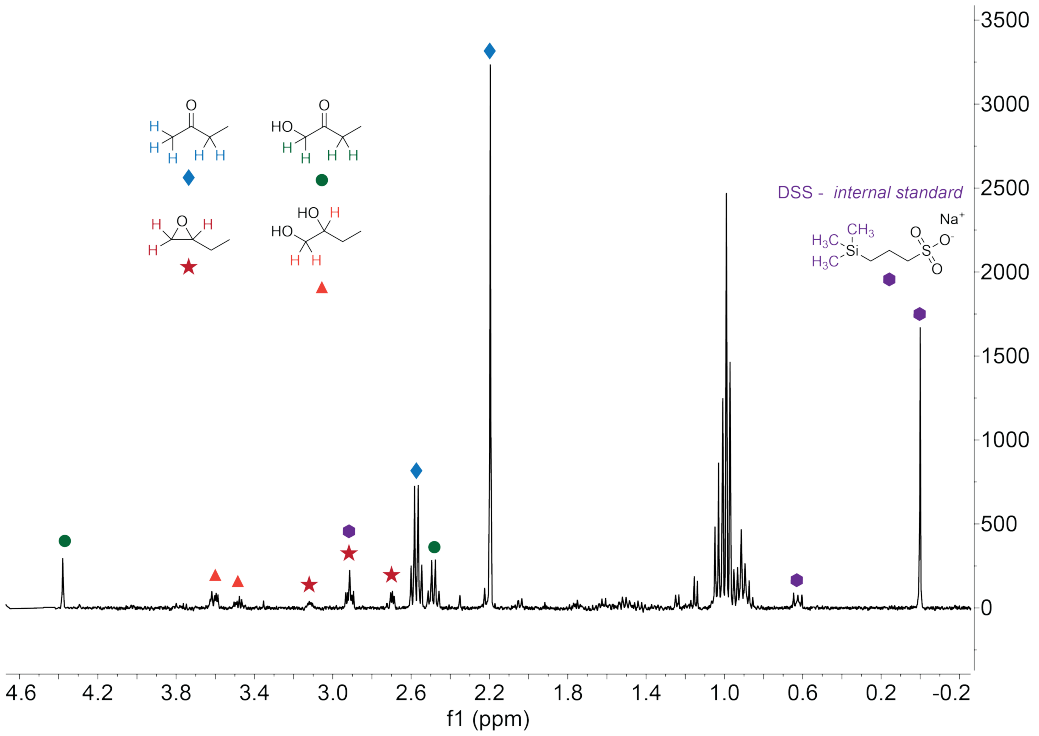

Figure C.4: ^{1}H NMR assignments for organic products observed. A typical NMR spectrum after electrolysis is shown here.

C.6 Supplementary Data and Discussion

Electrochemical Data

Additional Figures

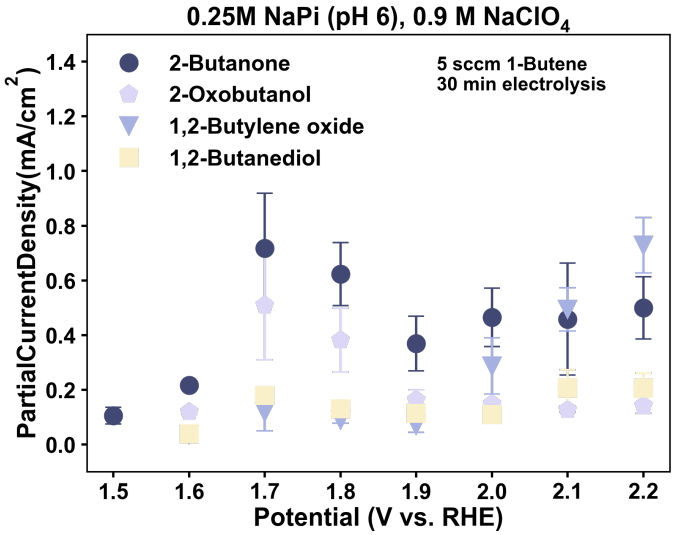

Figure C.5: Partial current densities of the organic products at different anodic potentials (100% iR corrected). Error bars represent standard deviations calculated from the mean of multiple replicates (n ≥ 3) with fresh electrodes for each measurement.

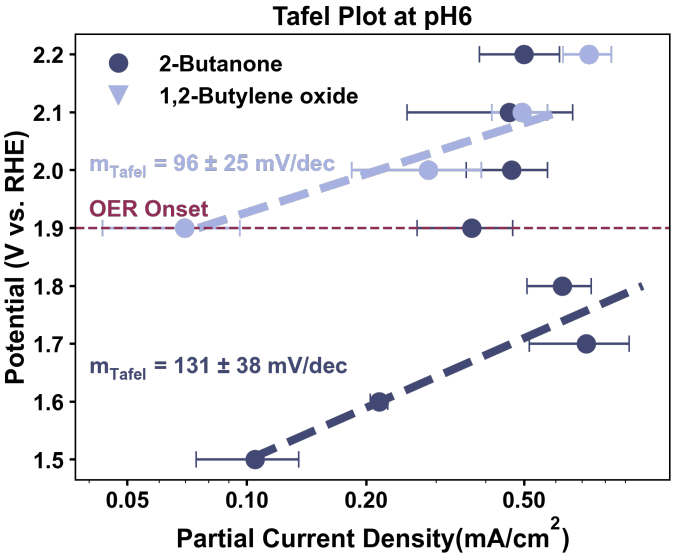

Figure C.6: Tafel plot for 2-butanone and 1,2-butylene oxide at pH 6. Error bars represent standard deviations calculated from the mean of multiple replicates (n ≥ 3) with fresh electrodes for each measurement.

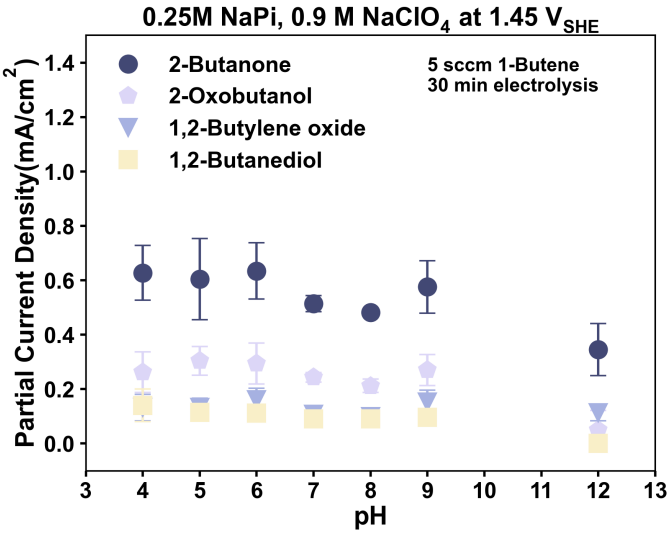

Figure C.7: Partial current densities of the organic products at different pHs. Error bars represent standard deviations calculated from the mean of multiple replicates ($n \geq 3$) with fresh electrodes for each measurement.

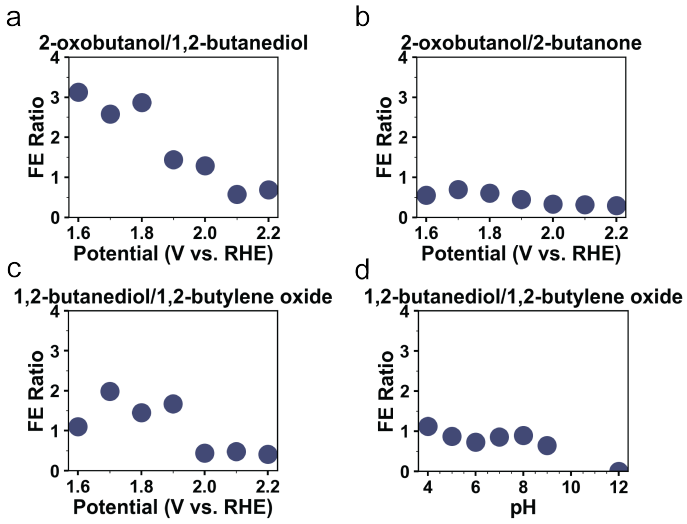

Figure C.8: Product selectivity ratio as a function of applied anodic potential: (a) 2-oxobutanol vs. 1,2-butanediol; (b) 2-oxobutanol vs. 2-butanone; (c) 1,2-butanediol vs. 1,2-butylene oxide. (d) 1,2-butanediol and 1,2-butylene oxide ratio as a function of electrolyte pH.

Analysis of transport limitation

The transport-limited current density to a planar surface is calculated by:

$$i_{lim} = nF\frac{D_A C_A}{\delta} \tag{C.1}$$

where n is the number of electrons transferred in the reaction, F is Faraday's constant, D_A and C_A are the diffusion coefficient and bulk concentration of species A, the most limiting reactant in the system, and δ is the hydrodynamic boundary layer thickness.

In our system, the limiting reactant is 1-butene with a solubility of 0.221 g/100 mL water, meaning the maximum bulk concentration of 1-butene is 0.04 M. The diffusion coefficient for 1-butene is assumed to be about 1E-5, which is a conservative estimate for gas in liquid as utilized in our previous work.[2] We conservatively assume a boundary layer thickness of about 100 μm in similar electrochemical cells with the gaseous reactants bubbling into the bulk electrolyte. As 1-Butene is introduced to the electrolyte in a flow-through gas-diffusion configuration, the actual boundary layer thickness is much less than 100 μm when the gas is directly bubbled into the bulk. Thus, we get the minimal estimation for $i_l im$:

$$i_{lim} = 2 \times 96485 \frac{1E-5 \frac{cm^2}{s} (0.04 \frac{mol}{L}) (\frac{1L}{1000 cm^3})}{1E-2 cm} = 7 mA/cm^2. \qquad \text{(C.2)}$$

The partial current density towards 2-butanone in the electrochemical study is less than $1 mA/cm^2$ (Figure C.4 and C.6), which is less than 15% of the transport-limited current density.

Peak modeling for X-ray photoelectron spectroscopy

The C 1s spectrum was acquired for every sample so that the adventitious carbon at 285 eV could be used to calibrate the charging effect. Shirley backgrounds were used when the peak fittings were conducted. ST(22)LA(1.75) was used as the line shape of Pd 3d, and LA(1.53, 243) for Cu 2p. The peak fitting for Cu 2p peaks used the peak models synthesized from the standard copper materials. The peak models were tested with Monte Carlo stimulation to ensure their validity.

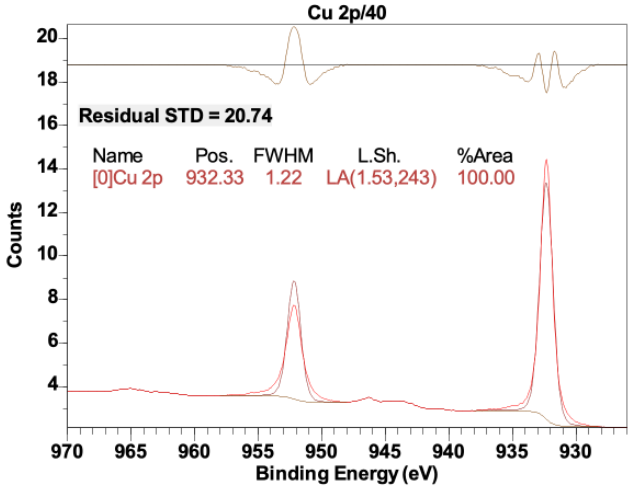

Figure C.9: Peak model for Cu. The synthetic peak model was used as the line shape (%&<>LS-CU) for peak fitting of samples.

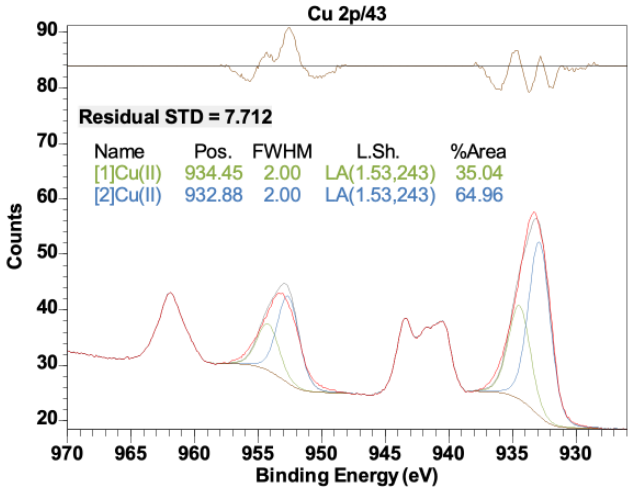

Figure C.10: Peak model for CuO. The synthetic peak model was used as the line shape (%&<>LS-CUO) for peak fitting of samples.

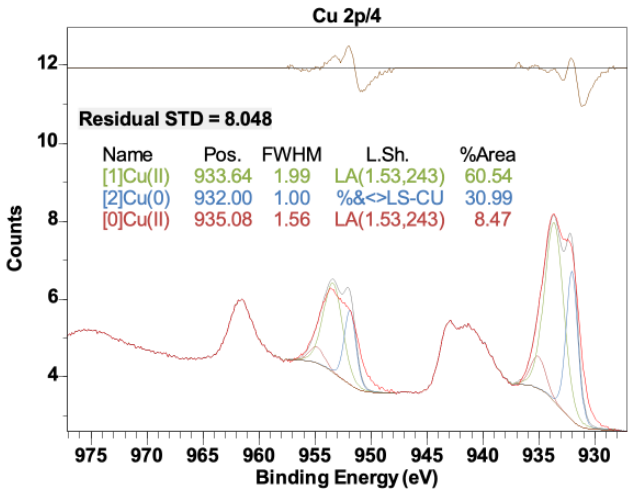

Figure C.11: Peak model for $Cu(OH)_2$. The synthetic peak model was used as the line shape (%&<>LS-CUOH) for peak fitting of samples. The commercial sample used appears to contain Cu0 impurities.

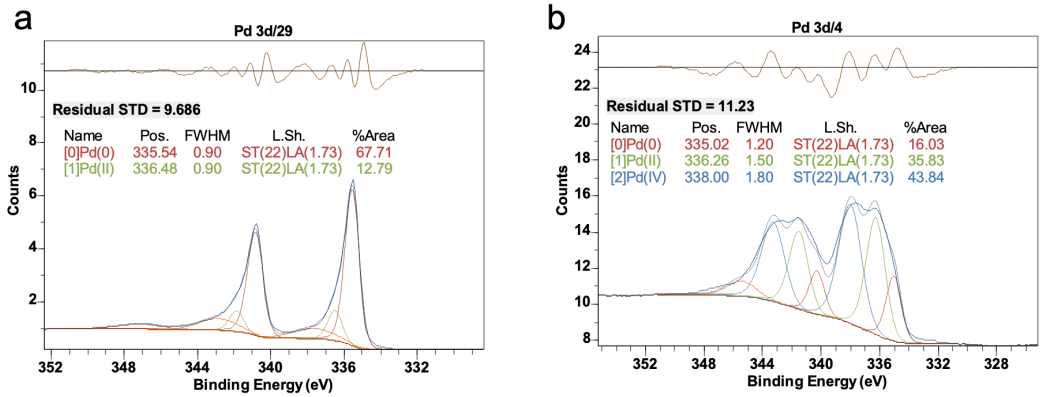

Figure C.12: XPS spectra. Shown are the Pd 3d spectra of **pristine (a) and post-electrolysis (b) Pd**.

Table C.3: XPS peak data for Pd 3d spectra of the pristine Pd.

Component	Binding Energy (eV)	FWHM	Area
$Pd^{0}_{5/2}$	335.5	0.9	61320.2
$Pd^{0}_{3/2}$	340.8	0.9	44150.6
$Pd^{2+}_{5/2}$	336.5	0.9	11926.7
$Pd^{2+}_{3/2}$	342.9	0.9	12473.9

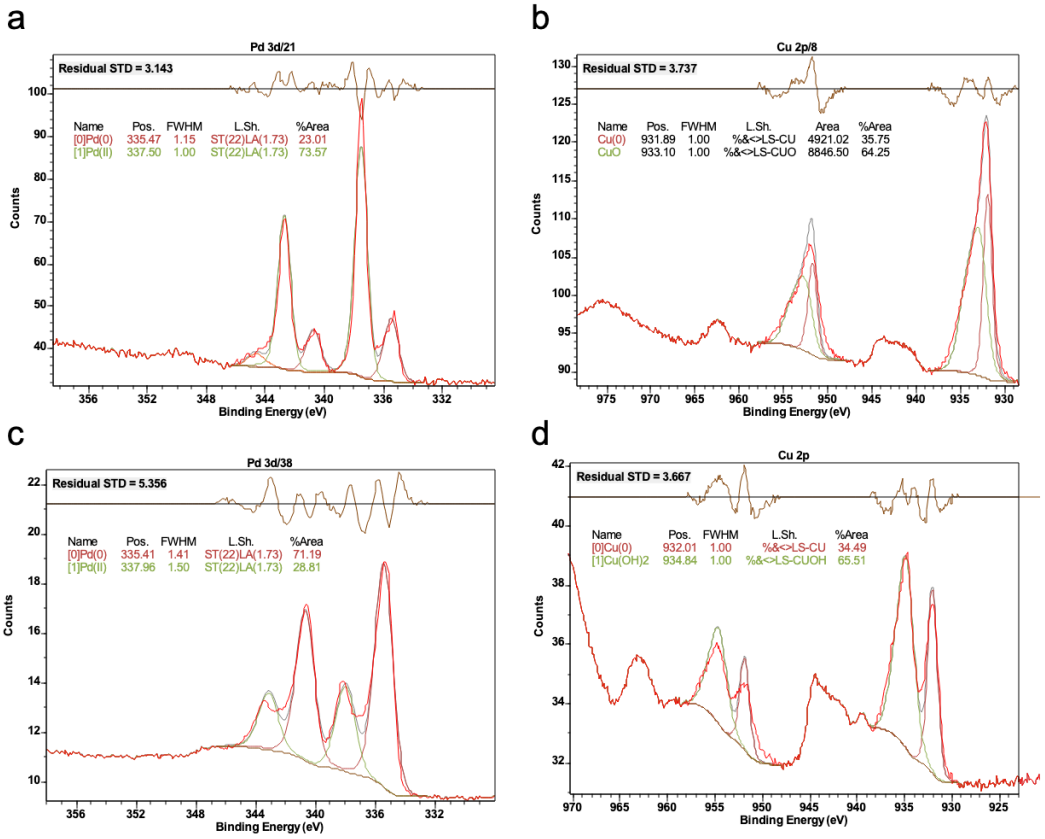

Figure C.13: XPS spectra. Shown are the Pd 3d spectra of **pristine (a) and post-electrolysis (c) PdCu** as well as Cu 2p spectra (b for pristine, d for post-electrolysis).

Table C.4: XPS peak data for Pd 3d spectra of the post-electrolysis Pd.

Component	Binding Energy (eV)	FWHM	Area
$Pd^{0}_{5/2}$	335.0	1.2	4994.7
$Pd^{0}_{3/2}$	340.3	1.2	2246.5
$Pd^{2+}_{5/2}$	336.3	1.5	11153.7
$Pd^{2+}_{3/2}$	341.5	1.5	7472.9
$Pd^{4+}_{5/2}$	338.0	1.8	13515.8
$Pd^{4+}_{3/2}$	343.3	1.8	9010.5

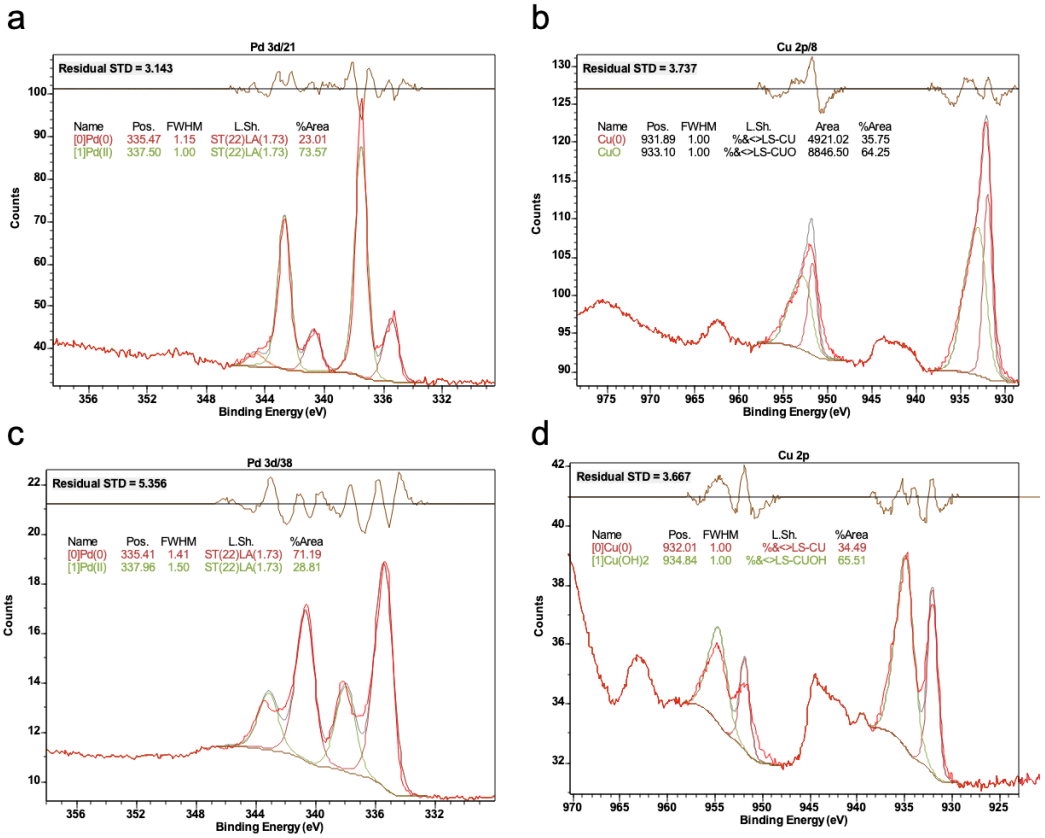

Figure C.14: XPS spectra. Shown are the Pd 3d spectra of **pristine (a) and post-electrolysis (c) PdCu** as well as Cu 2p spectra (b for pristine, d for post-electrolysis).

Table C.5: XPS peak data for Pd 3d spectra of the pristine PdCu.

Component	Binding Energy (eV)	FWHM	Area
$Pd^{0}_{5/2}$	335.5	1.1	195.9
$Pd^{0}_{3/2}$	340.7	1.1	130.6
$Pd^{2+}_{5/2}$	337.5	1.0	626.1
$Pd^{2+}_{3/2}$	342.7	1.0	417.4

Table C.6: XPS peak data for Cu 2p spectra of the pristine PdCu.

Component	Binding Energy (eV)	Area
$Cu^{0/+}_{3/2}$	931.9	4921.0
$Cu^{0/+}_{1/2}$	951.9	
$Cu^{2+}_{3/2}$ – CuO	933.1	8846.7
$Cu^{2+}_{1/2}$ – CuO	952.9	

Table C.7: XPS peak data for Pd 3d spectra of the post-electrolysis PdCu.

Component	Binding Energy (eV)	FWHM	Area
$Pd^{0}_{5/2}$	335.4	1.4	1464.6
$Pd^{0}_{3/2}$	340.7	1.4	976.4
$Pd^{4+}_{5/2}$	380.0	1.5	592.5
$Pd^{4+}_{3/2}$	343.1	1.5	395.0

Table C.8: XPS peak data for Cu 2p spectra of the post-electrolysis PdCu.

Component	Binding Energy (eV)	Area
$Cu^{0/+}_{3/2}$	932.0	1257.6
$Cu^{0/+}_{1/2}$	952.6	
$Cu^{2+}_{3/2}$ – $Cu(OH)_2$	934.8	2390.0
$Cu^{2+}_{1/2}$ – $Cu(OH)_2$	954.6	

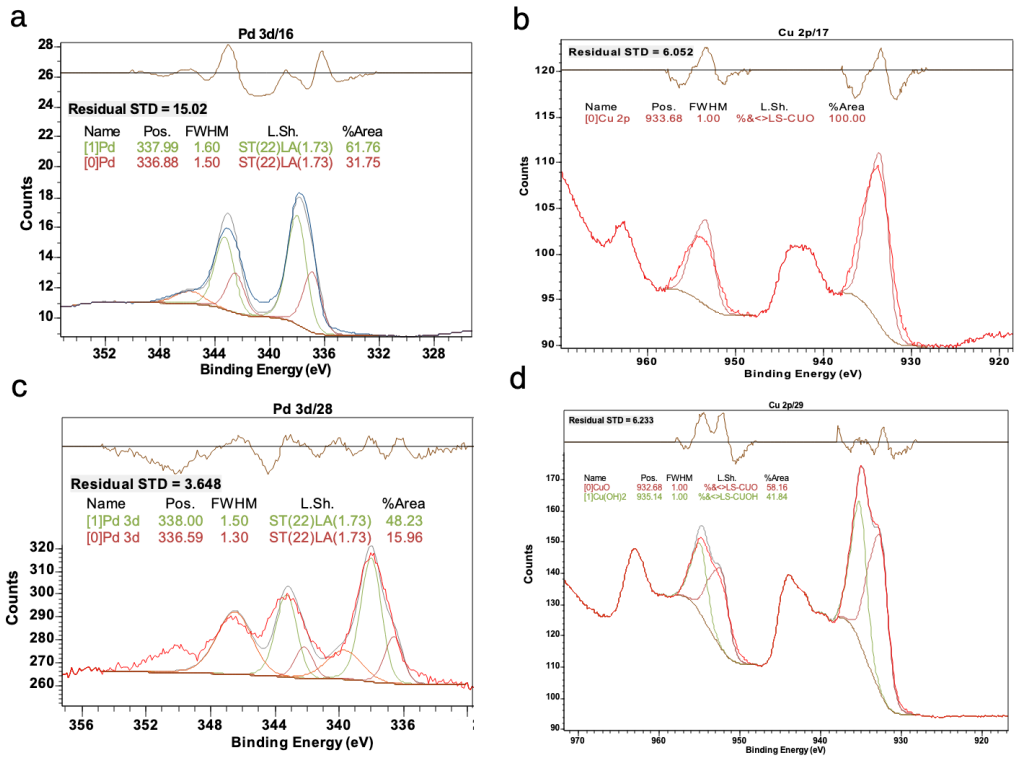

Figure C.15: XPS spectra. Shown are the Pd 3d spectra of pristine (a) and post-electrolysis (c) HT-PdCu as well as Cu 2p spectra (b for pristine, d for post-electrolysis).

Table C.9: XPS peak data for Pd 3d spectra of the pristine HT-PdCu.

Component	**Binding Energy (eV)**	**FWHM**	**Area**
$Pd^{2+}_{5/2}$	336.9	1.5	6832.7
$Pd^{2+}_{3/2}$	342.5	1.5	4555.2
$Pd^{4+}_{5/2}$	338.0	1.6	13255.5
$Pd^{4+}_{3/2}$	343.2	1.6	8881.2

Table C.10: XPS peak data for Cu 2p spectra of the pristine HT-PdCu.

Component	**Binding Energy (eV)**	**Area**
$Cu^{2+}_{3/2}$ – CuO	933.7	8558.0
$Cu^{2+}_{1/2}$ – CuO	953.6	

Table C.11: XPS peak data for Pd 3d spectra of the post-electrolysis HT-PdCu.

Component	Binding Energy (eV)	FWHM	Area
$Pd^{2+}_{5/2}$	336.9	1.3	418.3
$Pd^{2+}_{3/2}$	342.5	1.3	278.8
$Pd^{4+}_{5/2}$	338.2	1.5	902.2
$Pd^{4+}_{3/2}$	343.5	1.5	604.5

Table C.12: XPS peak data for Cu 2p spectra of the post-electrolysis HT-PdCu.

Component	Binding Energy (eV)	Area
$Cu^{2+}_{3/2}$ – CuO	932.7	22956.4
$Cu^{2+}_{1/2}$ – CuO	952.7	
$Cu^{2+}_{3/2}$ – $Cu(OH)_2$	935.1	16514.1
$Cu^{2+}_{1/2}$ – $Cu(OH)_2$	955.1	

Alternative peak fitting for LCF

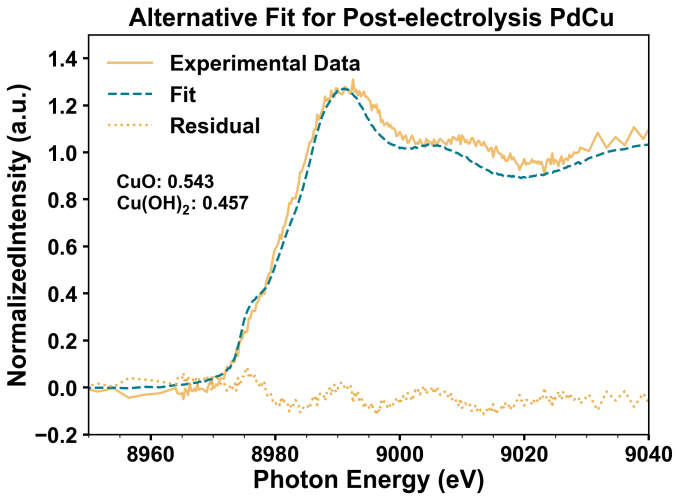

Figure C.16: Alternative linear combination fitting for pristine PdCu.

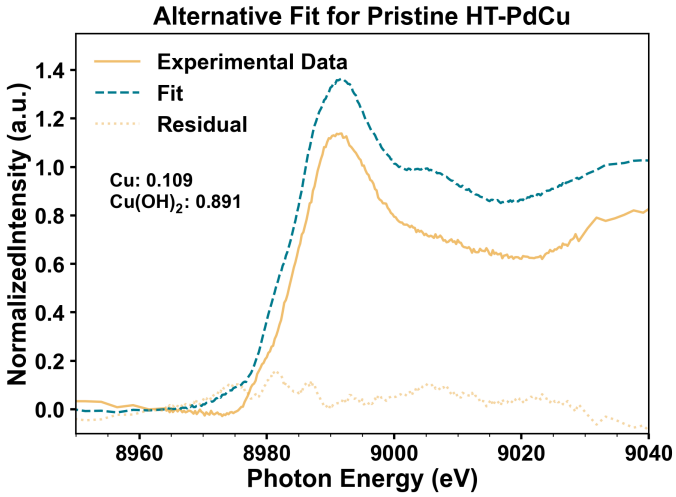

Figure C.17: Alternative linear combination fitting for post-electrolysis PdCu.

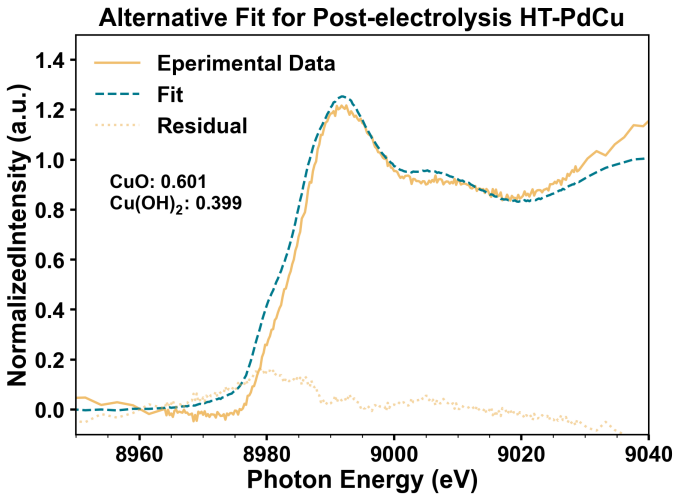

Figure C.18: Alternative linear combination fitting for pristine HT-PdCu.

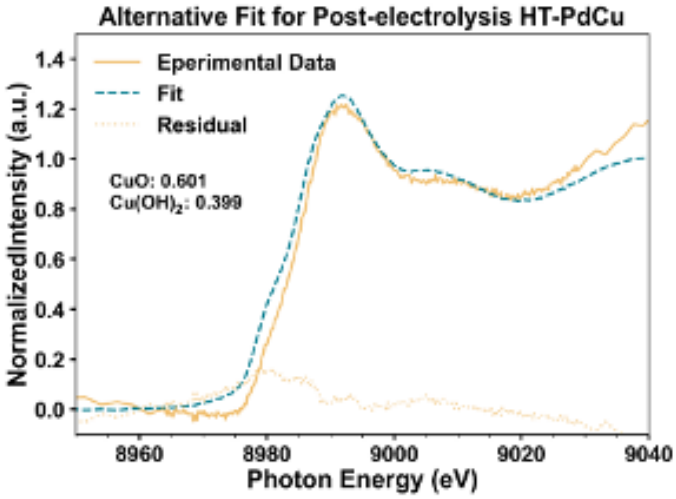

Figure C.19: Alternative linear combination fitting for post-electrolysis HT-PdCu.

Surface morphologies of catalyst-loaded electrode by SEM

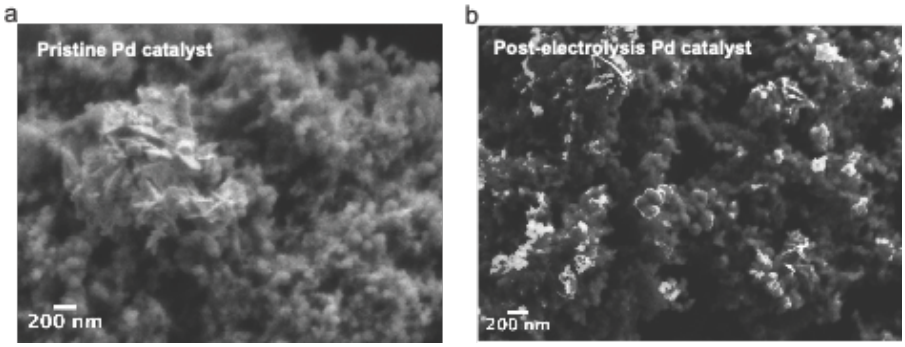

Figure C.20: Pre- and post-electrolysis electrode with Pd catalyst.

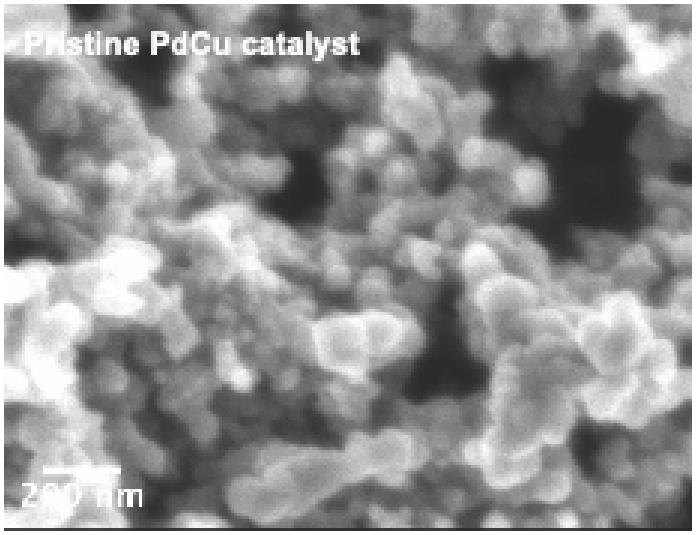

Figure C.21: Pristine PdCu catalyst on carbon paper electrode.

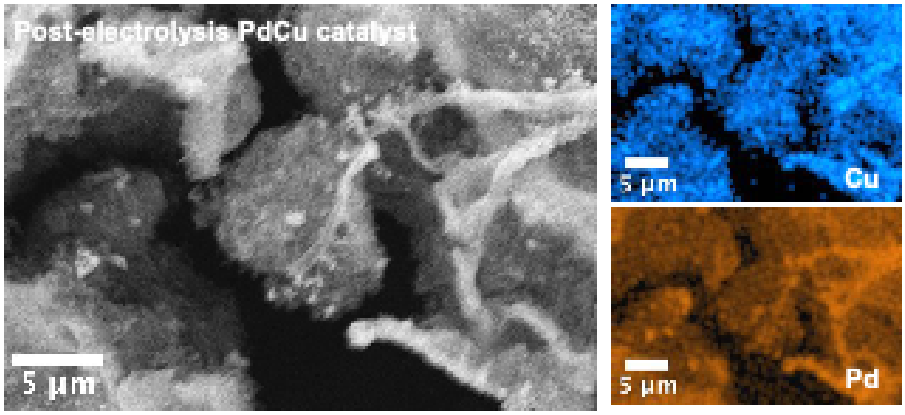

Figure C.22: Nanoparticle morphology in post-electrolysis PdCu and the EDS spectra of Cu and Pd.

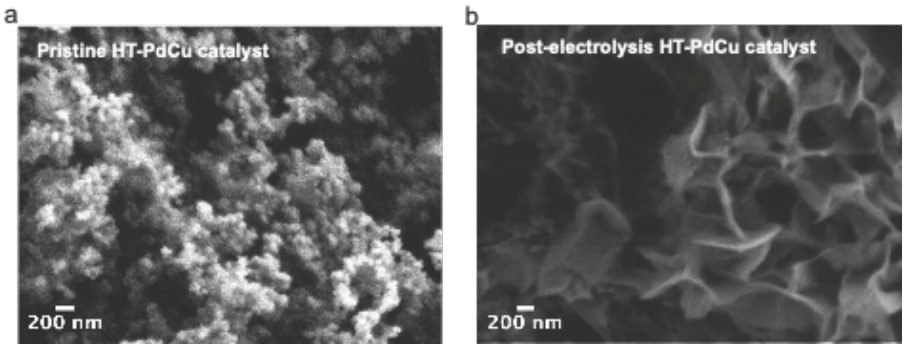

Figure C.23: Pre- and post-electrolysis electrode with HT-PdCu catalyst.

TEM characterization of the pristine and post-electrolysis PdCu

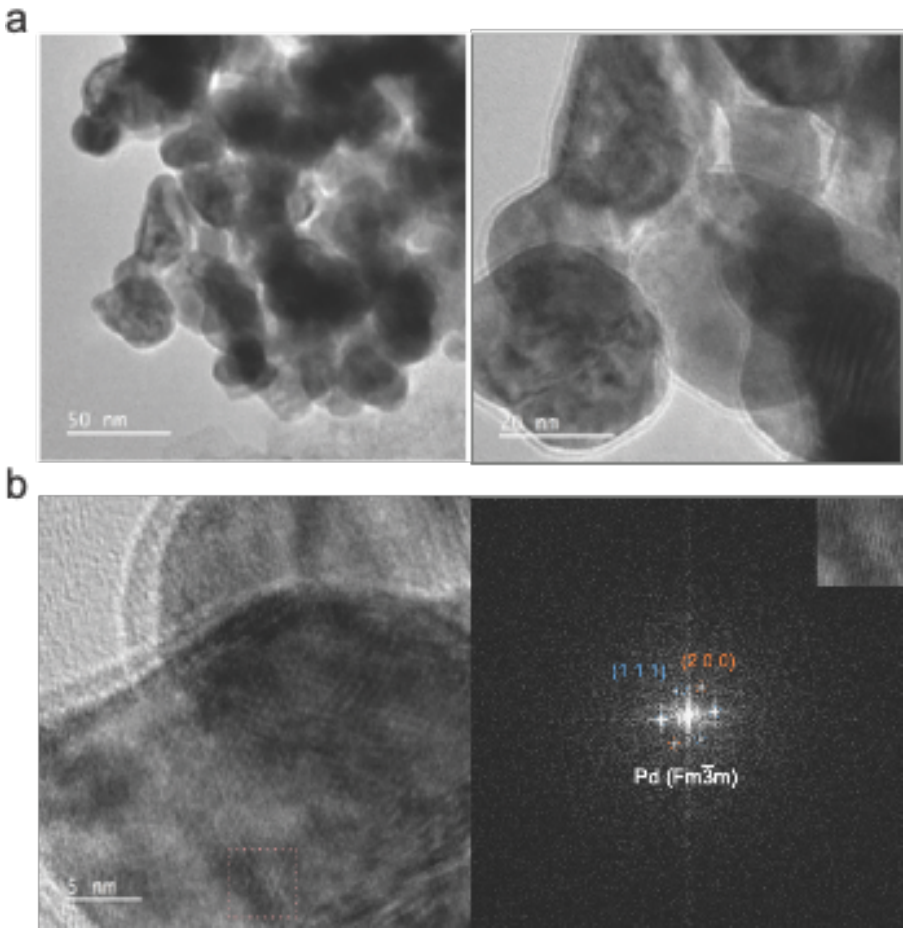

Figure C.24: Representative TEM images (a) of the pristine PdCu and electron diffraction patterns (b) obtained by Fourier transformation.

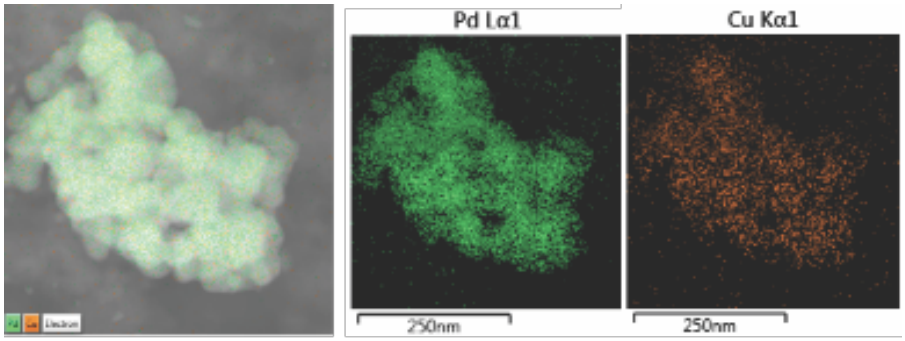

Figure C.25: High-resolution EDS mapping of the pristine PdCu.

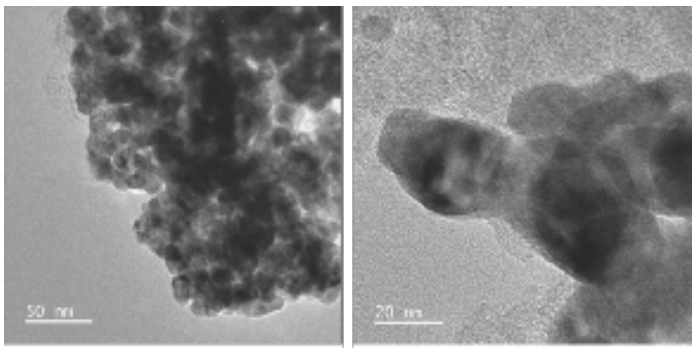

Figure C.26: Representative TEM images of the post-electrolysis PdCu.

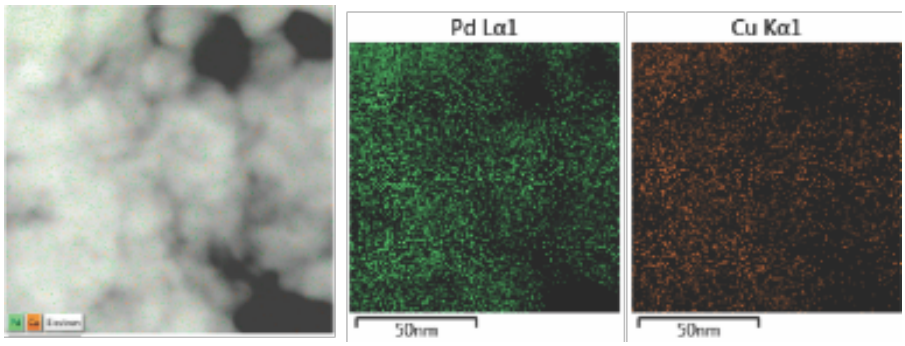

Figure C.27: High-resolution EDS mapping of the post-electrolysis PdCu.

XRD diffraction patterns

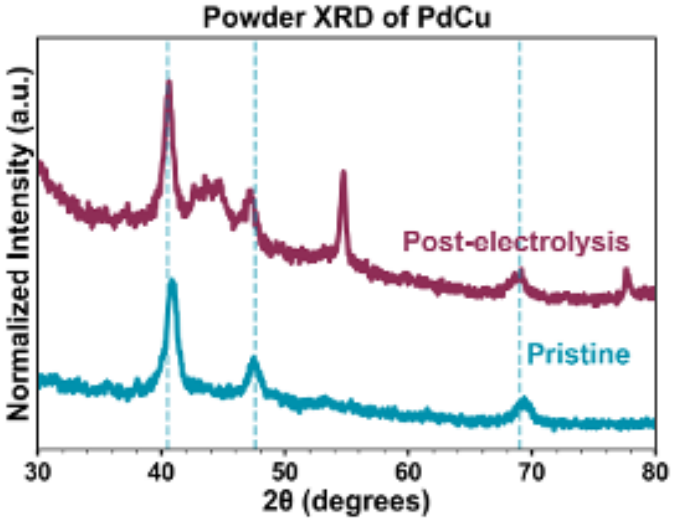

Figure C.28: XRD diffraction patterns of the post-electrolysis PdCu compared to the pristine PdCu.

Compilation of previous reports on alkene electro-oxidation

Table C.13: Comparison of electrochemical ketonization catalysts.

	Catalyst	Substrate	Electrolyte	Conditions	Proposed Pathway*	Highest FE†	Reference
1	PdCu	1-Butene	0.25 M NaPi (pH 6), 0.9 M $NaClO_4$	1.7 V vs. RHE	Heterogeneous	24%	Chapter 4 Figure 4.2b
2	Electrodeposited Pd nanodendrites	Propylene	0.1 M $HClO_4$ (pH 4)	1.1 V vs. RHE	Homogeneous (by dissolved Pd^{2+})	50%	[111]
3	Electrodeposited Pd	Propylene	0.1 M $HClO_4$	1 V vs. RHE	Homogeneous (by dissolved Pd^{2+})	24%	[114]
4	Pd/C	Propylene	0.1 M $HClO_4$	1 V vs. RHE	Heterogeneous	44%	[110]
5	PdO/C	Propylene		1.4 V vs. RHE		10%	
6	PtOx(O_2)	Propylene	Nafion MEA (0.5 M H_2SO_4), CH_2Cl_2 solvent	1.2 V vs. SHE	Heterogeneous	26%	[164]
7	PtOx(N_2H_2)	Propylene		1.6 V vs. SHE		10%	
8	Ag_3PO_4 tetrahedra	Propylene	0.1 M phosphate-buffered saline (pH 7)	2.2 V vs. RHE	Heterogeneous	4%	[89]

*The proposed pathway for the formation of ketone products, namely acetone when propylene used as the substrates, in the recent reports is thought to be either homogeneous or heterogeneous. For the studies proposed the homogeneous pathway catalyzed by dissolved Pd^{2+}, the authors offered the correlation between the amount of Pd^{2+} in the electrolyte and ketone formation as the evidence. It should be noted that the evidence for a heterogeneous route in the cited studies was less substantiated as no control experiments were conducted.

†The values of FEs were found in each paper's methods and supplementary material. An online plot digitizer was utilized to extrapolate the values from the figures.